Al-Farabi Kazakh National University

UDC: 620.3

On manuscript rights

MOHAMMAD SHAMS

SYNTHESIS OF HYDROXYAPATITE NANOFIBERS FOR TARGETED DRUG DELIVERY

8D07113 - Nanomaterials and Nanotechnologies

Dissertation submitted in partial fulfillment of the requirements for the degree of Doctor of Philosophy (PhD)

Scientific supervisors
Doctor of Chemical Sciences,
Professor,
Institute of Combustion Problems,
Mansurov Z.A.

Scientific advisor:
PhD in Inorganic Chemistry,
Institute of Nano Science and
Nano Technology,
The University of Kashan,
Masood Salavati Niasari

Republic of Kazakhstan
Almaty, 2022

CONTENTSE

NORMATIVE REFERENCES

In the present thesis, the following references for standards are used:

State Standard 7.1-2003. Bibliographic record. Bibliographic description. General requirements and rules.

State Standard 7.32-2001. Report on scientific - research work. Structure and rules for formulation.

State Standard 12.1.008-76. Occupational safety standards system. Biological security. General requirements. Specifications.

State Standard 3885-73. Reagents and very pure substances, sampling, packing, packing, and marking.

State Standard 6709-72. Distilled water.

State Standard 8.417-81. State system for ensuring uniformity of measurements. Units of physical quantities.

State Standard 1770-74. Laboratory glassware measuring. Cylinders, beakers, flasks, and test tubes. General technical conditions.

NOTATIONS AND ABBRIVIATIONS

ASTM	-	american society for testing and materials
AM	-	additive manufacturing
AMX	-	amoxicillin
BET	-	brunauer–emmett–teller analysis
BPMs	-	bone morphogenetic proteins
CAD	-	computer-aided design
CaPs	-	calcium phosphates
CFD	-	computational fluid dynamics
CPP	-	calcium pyrophosphate
CT	-	computed tomography
DOE	-	design of experiments
2D	-	two-dimensional
3D	-	three-dimensional
DGT	-	derivative thermogravimetric analysis
DICOM	-	digital imaging and communications in medicine
FEA	-	finite element analysis
FESEM	-	field emission scanning electron microscope
FGLS	-	functionally graded lattice structures
FGM	-	functionally graded materials
FTIR	-	fourier transform infrared spectroscopy
GBD	-	global burden of diseases
HA	-	hydroxyapatite
IHME	-	the institute for health metrics and evaluation
LVDT	-	linear variable differential transformers
MRI	-	magnetic resonance imaging
PCL	-	polycaprolactone
PVA	-	polyvinyl alcohol
SA:V	-	surface area to volume ratio
SBF	-	simulated body fluid
SEM	-	scanning electron microscope
SLA	-	stereolithography
SM	-	subtractive manufacturing
TCP	-	tricalcium phosphate
TE	-	tissue engineering
TEOS	-	tetraethyl orthosilicate
TETA	-	triethylenetetramine
TGA	-	thermogravimetric analysis
TPMS	-	triply periodic minimal surfaces
VSM	-	vibrating sample magnetometer
XRD	-	x-ray diffractometer
YLDs	-	years lived with disability

INTRODUCTION

General characteristics of the work. The work involves obtaining hydroxyapatite-based biodegradable scaffolds and their application for bone regeneration. HA and CPP nanopowders were obtained from eggshell waste, and metallic nano-silicates as resin reinforcement precursors were synthesized using the sonochemical method. In addition, a biodegradable resin was prepared in which Polylactic acid-polyurethane was used as the main matrix. Printed scaffolds' physicochemical, mechanical, in vitro, and in vivo properties were studied.

The actuality of the theme. Although bone fractures are a major public health concern worldwide, their incidence and costs have not been thoroughly investigated. Fractures are the main issue with bone illness, especially osteoporosis, and may be the patient's first obvious symptom. For example, an estimated 2 million people in the US annually experience a fracture. (including fractures in patients with osteoporosis).

According to the data provided by the Institute for Health Metrics and Evaluation (IHME), In the 21 GBD regions and 204 countries and territories from 1990 to 2019, there was a 33% increase in new fractures, 70% increase in prevalent cases of acute or long-term symptoms of a fracture, and 65% increase in YLDs [1]. Males also experienced more fractures than females across all age groups over the course of the study.

In cases where conventional methods cannot repair bone fractures, bone scaffolds promise effective therapies. In conventional techniques, there is a change in structure and function by biological substitutes when used for repairing the damaged bone. In addition to other problems such as a long period of convalescence, the need to remove some of the implanted material after the treatment period, the impossibility of blood flow and nutrients at the fracture site, infections due to the indestructible implanted material, etc.

With scaffolds' porous structure and interconnected pore networks with adequate pore size for efficient mass-transport activities (including nourishment of cells, exchanging nutrients, oxygen, and cell migration), 3D printing of biodegradable scaffolds can address such issues. They can be designed according to each patient's specific and individual defects in a short time with the lowest cost and side effects.

In this regard, the relevance of the research topic of the doctoral dissertation on achieving an optimal infill model of TPMS and FGLS structures, the resin composition of 3D printed scaffolds, and the study of their physicochemical and mechanical properties is undoubtedly relevant.

The research purpose: This work aims to obtain optimal TPMS and FGLS structures as the primary scaffold model and a biodegradable resin composition for bone regeneration in orthopedic surgery. To accomplish this goal, the following tasks were carried out:

1. Obtaining HA and CPP from eggshells, developing optimal conditions for synthesis, selecting the optimum composition with bioactivity properties, and studying their physicochemical properties.

2. Obtaining Nanofibrous biologically soluble scaffolds as an effective drug delivery system by electrospinning.

3. Synthesizing biodegradable resin from PLA/PUA as the oligomer, TEGDMA as the diluent, and Irgacure 819 as an initiator.

4. Synthesizing of nano-metallic silicates as precursor and reinforcement agent by sonochemical method.

5. Achieving and developing an optimal model of TPMS and FGLS structures as the primary scaffold model.

6. Study of the scaffolds' mechanical properties for various medical uses.

7. Implanting scaffolds in dog femur bone and study of the in-vivo properties and their effect on the healing process.

The main provisions for the defense of the thesis:

1. Mechanical tests showed that the TPMS and FGLS structures have good resistance against crushing and tension forces besides improving efficient mass-transport activities and can be used as potential medical scaffolds.

2. Results of different analyses confirmed that nanomagnetic resin precursors enhanced Osteogenesis.

3. Printed scaffolds coated with HA could decrease the period of convalescence compared to filing the fracture with HA powder.

The research object: Hydroxyapatite, Nanofibers, Bone scaffolds, Drug delivery, 3D printing.

The subject of research: Obtaining an optimal model of TPMS and FGLS structures as the primary scaffold model and a biodegradable resin composition for bone regeneration in orthopedic surgery.

The scientific novelty of research:

For the first time, the following results were obtained:

- Developing several algorithms for the parametric design of TPMS and FGLS structures from a unit cell.
- Using a simple and Eco-friendly sonochemical method to synthesize nano reinforce additives.
- Synthesizing a UV-cured/Reinforced biodegradable resin that can be used in standard SLA 3D printers.
- Physico-chemical, mechanical, in-Vitro, and in-Vivo studies of printed scaffolds showed the possibility of using them as functional scaffolds for bone surgery.

The theoretical significance. The main regularities of synthesis/design/3D printing of HA-based scaffolds by sonochemical/precipitation method were established.

The practical significance.

- For the First time, coated TPMS-based bone scaffolds were designed and implanted in the republic of Kazakhstan.
- The optimal condition for manufacturing hydroxyapatite and calcium pyrophosphate from eggshells was determined, and the obtained powders were used to obtain nanofibers.

- Several algorithms were developed to create TPMS structures by parametric design.
- Different resin precursors were synthesized as resin additives to improve the scaffold's osteogenesis and mechanical properties.
- In-Vivo and In-Vitro tests were done to measure the bioactivity properties of scaffolds.

Reliability of the results

The conclusions' validity and the results' reliability are due to the use of a wide range of modern physicochemical methods: X-ray Diffraction, SEM, TEM, IF-spectroscopy, TGA, EDX, and VSM.

Conclusions based on the obtained experimental data:

1. It was discovered that the crystalline HA powder obtained from an aqueous solution through chemical precipitation using a biological eggshell waste has a purity of~95%. According to EDX analysis, the Ca/P ratio is 1.5, which is suitable for medical uses and improves the osteogenesis properties of scaffolds.
2. The experimental data confirm that obtained polymer-based fibers by electrospinning with the addition of HA particles are well-qualified candidates for use as biological matrixes and drug delivery agents in TE and can reduce the convalescence period.
3. According to the results, among the TPMS structures, the Gyroid structure is the best in Top-load/Crush test, and the Lidinoid structure is the best in Tensile tests. However, it was found that adding the resin reinforce precursors to the matrix positively affects the mechanical properties, enhancing osteogenesis and reducing the convalescence period. In addition, obtained data from actual mechanical tests agree with the simulation data and confirm the method.
4. Producing resin reinforce precursors by ultrasonic method led to the formation of nanomaterials with suitable size, morphology, and surface properties for medical applications. These nanomaterials are soft magnetic materials, and numerous studies demonstrate the beneficial effects of magnetic nanoparticles and magnetic fields on osteogenic enhancements.

Relation to the plan of state research programs

This dissertational work was carried out without any framework.

Approbation of thesis

The thesis contents were reported and discussed at various international conferences and symposiums:

- International Kazakh-Russian symposium “Chemical physics and nanomaterials” dedicated to the 125th anniversary of N.N.Semenov (Almaty, Kazakhstan, April 09, 2021).
- VI Conference of students and young scientists “Chemical physics and nanomaterials” (Almaty, Kazakhstan, 18 March 2021).
- VII Conference of students and young scientists “Chemical physics and nanomaterials” (Almaty, Kazakhstan, 18 March 2022).

The author's personal contribution is conducting experiments, summarizing and interpreting the obtained results, and writing articles and reports.

Publications. The results of the thesis are reflected in 7 scientific papers, including:

- Three scientific articles published in journals having an impact factor according to the Scopus database;
- Four oral abstract presentations at international conferences and symposia;

Volume and structure of the thesis. The thesis is presented in 77 pages and includes 42 Figures, 15 Tables, and 12 formulas. The work includes an introduction, literature review, description of objects and research methods, results and discussion, conclusion, and list of references, including 115 names.

1 LITERATURE REVIEW

1.1 Natural bone and it alternatives

Bones are rigid organs that consist of osseous tissue, bone marrow, endosteum, periosteum, cartilage, nerves, and vascular channels constituting the skeleton of vertebrate animals. Between 60 and 70 percent of bone is made up of mineral phase, while between 5 and 10 percent is made up of water. The remaining is an organic matrix made up of proteins like collagen. The main component of bone's mineral phase is hydroxyapatite, a calcium phosphate present as nanocrystals between 25 to 50 nm in size [2].

Table 1 – Bone mechanical characteristics [3, 4].

Property	Cortical bone	Cancellous bone
Tensile strength (MPa)	50 - 150	10 - 100
Compressive strength (MPa)	130 - 230	2 - 12
Young's modulus (GPa)	7 - 30	0.02 - 0.5
Strain to failure (%)	1 - 3	5 - 7
Shear strength (MPa)	53 - 70	
Shear modulus (GPa)	3	

Bone fractures are a global public health issue. Fractures are the main issue with bone illness, especially osteoporosis, and may be the patient's first obvious symptom. In cases where conventional methods cannot repair bone fractures, bone scaffolds promise effective therapies.

Table 2 – Properties of bone graft substitutes[5, 6].

Property	Allograft	Polymers	Ceramics	Composites	Cell-based therapies	Growth factors
Biocompatibility	Yes	Yes	Yes	Yes	Yes	Yes
Osteoconductivity	Yes	Yes	Yes	Yes	No	No
Osteoinductivity	Yes	No	No	Yes	No	Yes
Osteogenicity	Yes	No	No	No	Yes	No
Osteointegrity	Yes	No	Yes	Yes	Yes	No
Mechanical match	No	Yes	Yes	Yes	No	No

The construction of scaffolds that aid bone regeneration is a hot topic in tissue engineering (TE). Table 2 presents the main bone graft substitutes used as scaffolds constituent material and their bio-properties.

1.2 Calcium phosphate materials

In terms of composition, bioactivity, and osteoconductive properties, calcium phosphates fall under synthetic bioactive and biocompatible materials similar to bone. The capacity of a material to function with an appropriate host response in a particular application is known as biocompatibility [7]. Because of these properties have been widely used in the medical field in the form of various composites, granules, powders, granules, and dense porous blocks [8].

Calcium is one of the ions that form the bone matrix, which causes bone formation and maturation through calcification. Furthermore, Calcium ions promote bone regeneration via influencing cellular signaling. In addition, Calcium stimulates bone growth precursor cells for bone tissue regeneration and motivates mature bone cells by producing nitrogen monoxide [9].

Along with the interface, CaPs also have chemical bonds with the bone, which are considered to be triggered by the adsorption of proteins that promote bone growth on the surface of the biomaterials [10]. In addition, a series of CaP compounds are available that differ in their chemical stoichiometry and crystallographic structure. The Ca/P ratio, which ranges from 1 to 2, is the defining factor, as shown in Table 3.

Table 3 – Ca/P ratio classification of CaP materials [11].

Phase	Formula	Crystal Structure	Ca/P
Tetra calcium phosphate	$Ca_4O(PO_4)_2$	Monoclinic	2.00
Hydroxyapatite	$Ca_{10}(PO_4)_6(OH)_2$	Hexagonal	1.67
Tricalcium Phosphate	$Ca_3(PO_4)_2$	Rhombohedral	1.50
Octa calcium phosphate	$Ca_8H_2(PO4)_6.5H2O$	Monoclinic	1.33
Dicalcium Phosphate Dihydrate	$CaHPO_4.2H_2O$	Triclinic	1.00
Calcium Pyrophosphate	$Ca_2P_2O_7$	Hexagonal, Triclinic, Monoclinic	1.00

Some facts and issues regarding the use of calcium phosphate materials in medicine are:

1. All of the various forms of these materials appear to be very biocompatible.
2. Most forms of these materials are osteoconductive and chemical bonds are formed between these materials and bone.
3. The mechanisms of interaction with the bone are not well understood. It is unknown if the ceramic partially dissolves and re-precipitates on the surface as natural apatite, if the implant material acts as a seed for the natural material, or if both mechanisms occur.
4. There are many forms of calcium phosphate materials: crystalline with various crystal sizes, amorphous, and variable Ca to P ratios.

5. The methods used in the application of coatings generally change the crystal structure of the ceramic.

6. The long-term interface strength of coatings is not known.

7. The long-term attachment of coating to substrate and coating to the bone may not be needed in many applications. The primary function of HA may be to encourage an initial bed of bone whose long-term behavior is governed by the overall implant design.

8. Rigid fixation of implant interfaces is not a panacea. Implant design is also important. Solid fixation in some designs may lead to poorer performance of the total system, e.g., a rigidly fixed implant could stiffen the bone-implant system and result in long-term loss of bone density.

9. The ability to stimulate bone generation is not very sensitive to the form of the calcium phosphate material; however, the resorption rate and strength are.

1.3 Hydroxyapatite

A naturally occurring mineral type of calcium apatite is called hydroxyapatite (HA). Human knowledge of the chemical composition and structure of bone is progressively evolving. Bone comprises 60% inorganic components, including calcium phosphates predominantly as hydroxyapatite, 10% water, and 30% organic component. The era of HA in regenerative science dates back to the 1950s [12] when bioceramics were used as an inert scaffold for filling bone defects. Calcium orthophosphates have a long history that extends back to 1770; [13] there are also published works that cover the early history up to 1950 [2, 14].

HA possesses the highest solubility and thermodynamic stability (after Fluorapatite) in physiological circumstances than other CaPs. Moreover, HA includes the greatest similarity with the function and structure of the biominerals, such as teeth and bone, making it a significant particle for dental and bone researchers.

1.3.1 Crystal structure of HA

HA is the primary mineral component of bone that belongs to the apatite group with a general chemical formula of $M_{10}(XO_4)_6Z_2$, in which M= Ba^{2+}, Ca^{2+}, Sr^{2+}, Pb^{2+}, Na^{+}, La^{3+}; XO= VO_4^{3-}, AsO_4^{3-}, PO_4^{3-}, CO_3^{2-}; Z = Cl^{-}; OH^{-}, F^{-}; CO_3^{2-} [15]. The HA's crystallographic structure can be classified as hexagonal or monoclinic for each space group. The HA's monoclinic structure is unstable; moreover, it can be destabilized even by the existence of fewer ions [16]. Hence, it is less practically crucial in comparison to the hexagonal structure. In contrast, HA in hexagonal form is stable and observed in most biological apatites and nonstoichiometric compositions [17].

The structure is created by PO_4 tetrahedral arrays reserved by intermingled Ca ions. Ca fills two various sites within a hexagonal structure, Ca (I) and (II). Four of ten Ca atoms in the HA structure are placed at Ca (I) with six other atoms placed at the Ca (II) site. Figure 1 presents the structure of hydroxyapatite crystals.

Unit cell lattice dimensions for hydroxyapatite are a=0.94 nm and c=0.68 nm, and it has hexagonal symmetry. The unit cell of the lattice is thought to be oriented along the c-axis when the lattice's characteristics and symmetry are taken into

consideration. This would justify a preferred orientation that gives rise to an oriented growth along the *c*-axis and a needle-like morphology.

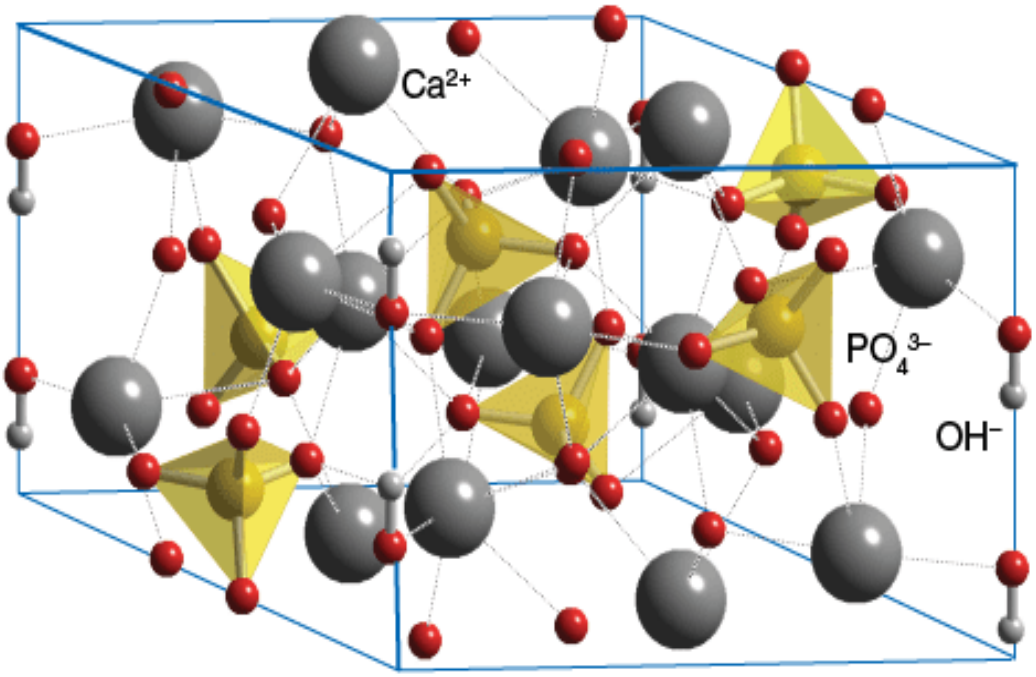

Figure 1 – The hydroxyapatite structure, $Ca_5(OH)(PO_4)_3$, is shown as Ca^{2+} ions coordinated by phosphate and OH^- ions into a strong three-dimensional structure. The isolated O atoms are OH^- ions with the H lying outside the unit cell [18].

The similarity in crystallographic characteristics is shown in Table 4: Lattice parameters (±0.003 Å) between hydroxyapatite, dentine, enamel, and bone [19].

Table 4 – Crystallographic characteristics: lattice parameters (±0.003 Å).

Composition, wt%	Enamel	Dentine	Bone	HA
a-axis (Å)	9.441	9.421	9.41	9.430
c-axis (Å)	6.880	6.887	6.89	6.891
Crystallinity index, (HA=100)	70–75	33–37	33–37	100

1.3.2 Biological properties of HA

The extraordinary properties of HA, like nontoxicity, biocompatibility, bioactivity, osteointegration, osteoconduction, osteoinduction, biological and biochemical affinity have made it the top contender in biomedical engineering and modern orthopedic surgery as an artificial bone substitute.

HA can physically or chemically integrate drug compounds. Therefore, the medication is intact until it reaches the intended spot. Additionally, the drug could be delivered in a controlled manner over time as HA gradually degrades. Thus, hydroxyapatite is a leading candidate for targeted drug delivery [20, 21].

HA is more stable than other calcium phosphates. Regarding thermodynamic stability, HA is the most stable calcium phosphate compound under physiological conditions such as body fluid composition, pH, and temperature [22].

Due to their biocompatibility and capacity to adhere directly to bone, bioactive calcium phosphate ceramics used as coatings on bioinert metallic substrates for orthopedic and dental implants have drawn attention worldwide [23]. However, several variables, including coating thickness, chemical composition, crystallinity, phase purity, cohesive and adhesive strengths, and resorption resistance, may affect the performance of any hydroxyapatite coating.

To prevent the hydroxyapatite coating from cracking, peeling off, or chipping during implant emplacement, the coating's adhesion strength to the implant surface must be enhanced. Low porosity, high cohesive strength, good adherence to the substrate, a high degree of crystallinity, high chemical purity, and phase stability would all be characteristics of the ideal hydroxyapatite coating [24].

Since 1985, when Furlong and Osborn started the first clinical trials using implants with hydroxyapatite coating [25], according to reports, hydroxyapatite coatings can effectively increase clinical success, and a mean follow-up study of 10 years revealed a failure rate of less than two percent [26].

1.3.3 Mechanical properties of HA

Although this compound has good biological properties, its mechanical properties are unsuitable for medical applications and HA-based implants are exposed to excessive failure, wear, and untimely fracture. In vivo results showed that HA's properties must be approached to the properties of natural bone without affecting its biodegradability. This prompted the researchers to investigate various methods like adding dopants, coating, controlling morphologies, and composite fabrication with biomaterials to face this phenomenon.

Nano-sized synthesis of HA particles can help to overcome the brittleness problems. Numerous studies show that nano-size HA particles have better mechanical properties than their micro-size counterparts [27 - 29].

1.3.4 Synthesis methods of HA

Various techniques are developed to obtain HA from natural resources. These techniques result in different sizes, morphologies and yield different crystalline phases of the calcium phosphate besides pure crystalline HA and are classified into three main groups and several subgroups [30].

1. *Wet techniques:* (hydrolysis, chemical precipitation, hydrothermal, sol-gel, sonochemical emulsion).
2. *Dry techniques:* (solid-state, mechanochemical).
3. *High-temperature techniques:* (pyrolysis, combustion, combination procedures, and synthesis from biogenic sources).

The most important structural data of this component are summarized in table 5.

Table 5 – The biological, mechanical, and physiochemical properties of HA.

Flexural Strength	pH stability range in aqueous	Solubility at 25°C	Density	Space group
100 - 120 MPa	9.5 - 12	~0.0003 g/L	3.16 g/cm^3	hexagonal $P6_3/m$
Formula mass	Unit cell	Birefringence	Mohs scale hardness	Specific Gravity
502.31 g/mol	a = 9.41 Å, c = 6.88 Å; Z = 2	δ = 0.007	5	3.14 - 3.21
Young's modulus	Compressive strength	Modulus of Elasticity	Decomposition Temp.	Melting point
80-110 GPa	400-900 MPa	7.00 - 13.0 GPa	>1000 ºC	1614 ºC
Osteoconductivity	Biocompatibility	Bioactivity	Biodegradation	Cellular-compatibility
High	High	High	Low	High

1.4 Calcium pyrophosphate

An insoluble calcium salt with the pyrophosphate anion is called calcium pyrophosphate ($Ca_2P_2O_7$). CPP can control when calcification starts in bone and functions as a catalyst to boost mineralization. Due to its high biocompatibility and absorption properties, it has gained increasing attention in bone TE.

1.4.1 Crystal structure of CPP

Structures of both α- and β-CPP contain pyro groups, P_2O_7, which consist of two corner-shared PO_4 tetrahedra with P-O-P angles of 130° for the α phase and angles of 131° and 135° for the phase β.

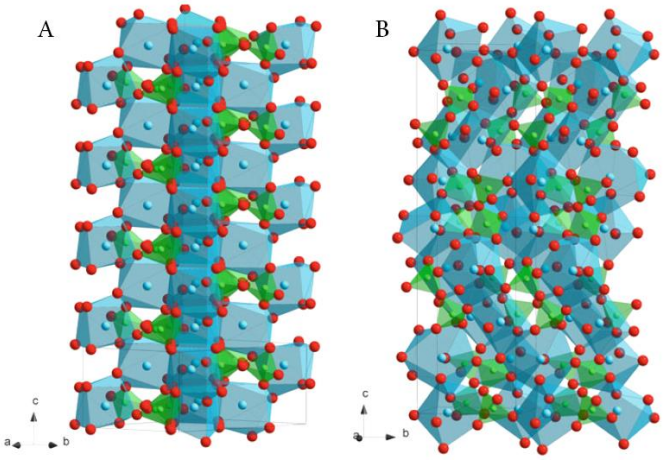

Figure 2 – Crystal structures of A) α-calcium pyrophosphate and B) β-calcium pyrophosphate [31].

In α-CPP, the Ca ions coordinate with eight oxygen atoms and the chains of edge-shared Ca polyhedral form sheets parallel and perpendicular to the *ac* plane.

Ca has three different coordination numbers in β-CPP: 7, 8, and 9. Each pyrophosphate group is connected to another by Ca atoms that both share, resulting in an endless chain of pyrophosphate-Ca chelate-like chains [11]. Figure 2 presents the crystal structures of both the α and β phases.

1.4.2 Biological properties of CPP

CPP shows a positive interaction with living tissue and has been frequently used in the medical industry due to its bio-active, bio-compatible, biodegradable, and osteoconductive properties [32, 33]. Some CPP applications in the medical field are artificial bone, scaffolds, dentin regeneration, implants, coatings, etc.

1.4.3 Mechanical properties of CPP

Calcium phosphate materials' mechanical strength and shape are affected by pores larger than 100 μm, resulting in brittleness, low impact resistance, and low tensile stress. Although CPP has the properties mentioned above, it is utilized in non-load bearing implants, defect-filling, and coating techniques because its compressive strength is better than that of natural human bone [34].

1.4.4 Synthesis methods of CPP

Heating phosphates leads to the formation of Pyrophosphates. Since pure CPP can exist in three polymorphic forms (β-CPP, α-CPP, and γ-CPP), its synthesis is thought to be complicated. However, the biggest interest for utilization as a bone graft material is in the β-CPP phase [35].

Table 6 – The biological, mechanical, and physiochemical properties of CPP.

Density	Solubility	Refractive index	Bioactivity
3.09 g/cc	Insoluble in H_2O; Soluble in Diluted Acid	1.585	High
Molecular Weight	Topological Polar Surface Area	Osteoconductivity	Cellular-compatibility
254.099 g/mol	136 Å²	High	High
Melting Point	pH	Biocompatibility	Decomposition Temp.
1353 °C	Between 5,5 and 7,0 (10 % suspension in water)	High	>1000 ºC

For the synthesis of crystalline CPP, several methods have been published in the literature; the most popular ones are:

1. *Precipitation method*
2. *Wet chemical process*
3. *Gel growth technique*

Other techniques such as wet precipitation, solid-state reaction, glass crystallization, and thermal decomposition of dicalcium phosphate dehydrate or dicalcium phosphate are reported to synthesize nano-sized CPP.

1.5 Disadvantages of calcium phosphate materials as bone scaffolds

CaP's porosity, which makes it brittle, fragile, and only useful for non-weight-bearing bone repairs, is its most significant flaw [36]. For example, Joaquim M Oliveira et al. reported that the compressive strength of a HA scaffold is 30.2 ± 6.0 MPa, significantly lower than cortical bone (130 - 180 MPa).

For cells and growth factors to access a large portion of the scaffold surface, the scaffold's porosity is essential for effective wound repair. Interconnected pores are essential to facilitate cells' invasion, growth, nutrition and the diffusion of waste from the inner core. However, higher porosity and pore size reduce compressive strength and hardness. In vitro, osteoblast cell proliferation and osteogenic differentiation are facilitated by small pore size and low porosity, whereas higher porosity promotes cell recruitment and vascularization in-vivo [37]. Consequently, achieving the proper pore size and porosity for a specific circumstance is necessary.

The flexural and tensile strength of CaP scaffolds can also be influenced by other factors, such as crystallinity and particle size.

Scaffolds made of calcium phosphate also have no osteoinductive function [38]. However, bone morphogenetic proteins (BPMs) have significant osteogenic properties [39], and their combination with CaP can result in a scaffold with greater osteoinductive capacity.

1.6 3D printing in tissue engineering

3D printing is positioned to be a key component of personalized regenerative medicine in the twenty-first century. The variety of biomaterials that can be used in this field has slowed down the development of bio-screws, implants, and scaffolds for TE. There have been numerous recent initiatives to develop and fabricate novel biomaterials and compositions for AM [40].

Google Ngram is an online search engine that charts the frequencies of any set of search strings using a yearly count of n-grams found in sources printed between 1500 and 2019 in Google's text corpora in English and other languages [41]. In the following, we can see that the use of "hydroxyapatite" in books has been going on since the 1920s and has increased over the years, which shows the importance of this component in science. Also, the term "3D printing" started to appear in the 2000s decade and has had a staggering growth in the last decade.

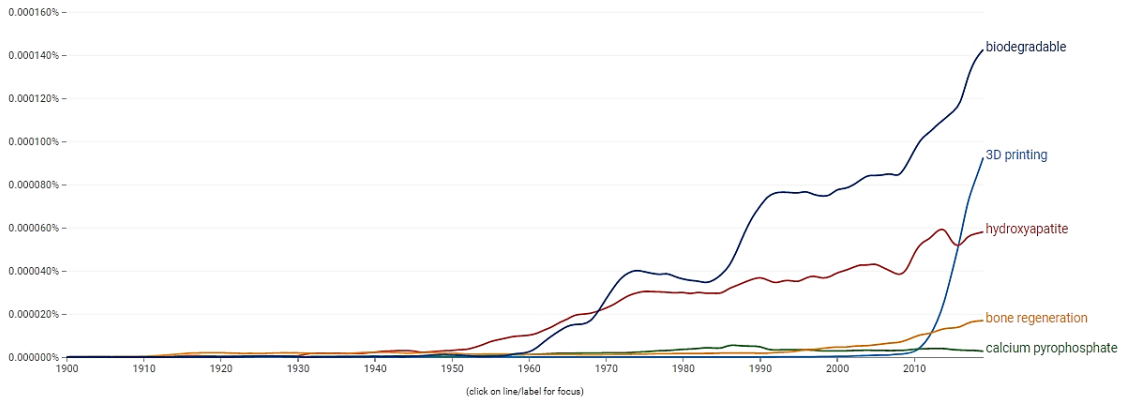

Figure 3 – The frequency of 5 different keywords between 1900 to 2019 in Google's text corpora in English language sources.

The following are a few of the most significant benefits of using three-dimensional printing for manufacturing scaffolds: Low production costs, effective management of porosities, co-culture of different cells, adaptable and precise personalization tailored to the target region, and capacity to produce complicated geometries [42].

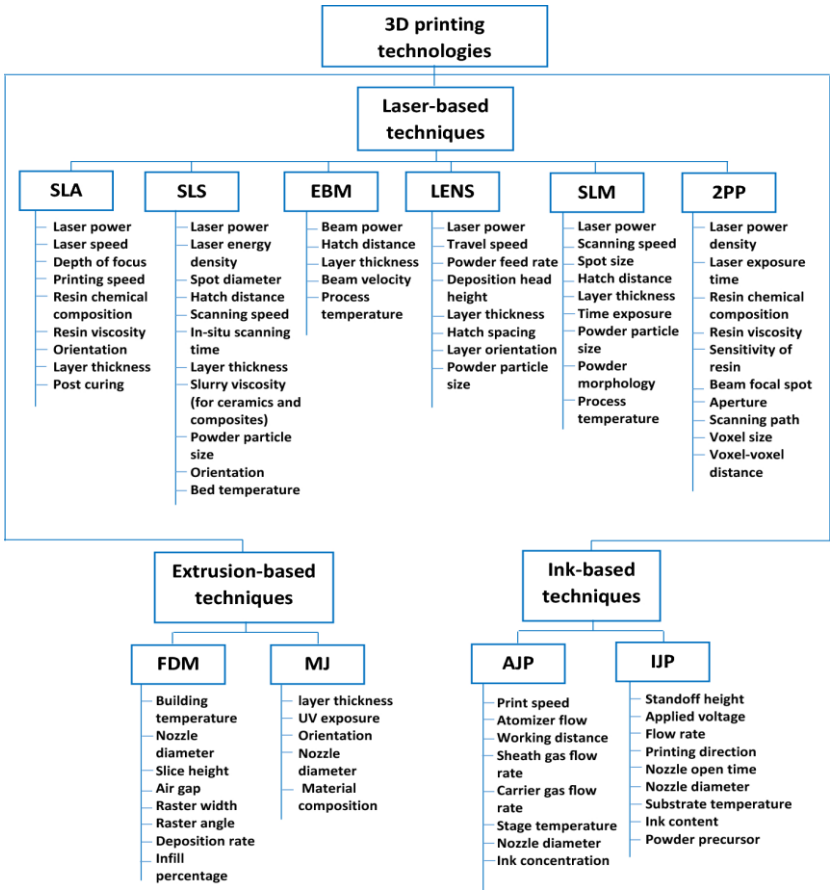

Figure 4 – Process parameters and material variables for 3D printing technologies.

Bone tissue scaffolds are made using various methods, including increasingly popular 3D printing technology (Figure 5a). Bioprinting is an additive fabrication technique that can construct or create functional 3D organ-like or tissue structures. Recently, it has drawn scientists' attention to various cell-laden structures for the regeneration of many tissues (Figure 5b). These methods often involve using bio-inks to build scaffolds layer by layer. In addition, one or more biomaterials are combined with living cells to create bio-inks [43].

Many 3D bioprinting systems have been developed in the same categories as 3D printing techniques. Extrusion-based bioprinting has gained popularity among these methods (Figure 5c) because hydrogel precursors having low-shear viscosities can be used for printing and can deposit high cell densities, similar to the target tissue structure.

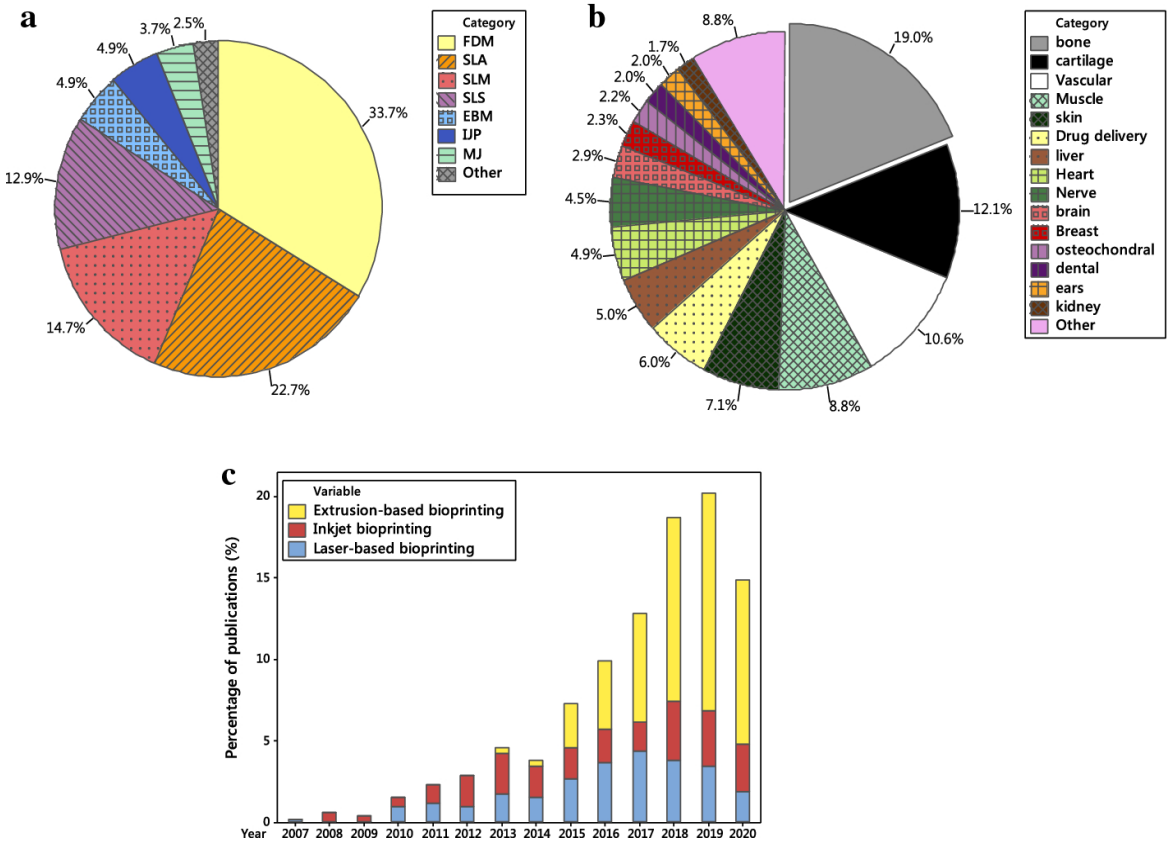

Figure 5 – a) Percentages of different 3D printing approaches investigated for bone scaffolds; b) percentages of 3D bioprinting uses in different tissue engineering applications; and c) comparison of uses of different 3D bioprinting approaches over time (based on Scopus search, type of document was article).

Figure 6 presents the latest information that shows Fused deposition modeling (FDM)/fused filament fabrication (FFF) was the most widely used 3D printing technology in 2021, with 71 percent of respondents using it in houses. The second most popular technology was selective laser sintering (SLS), which was adopted by 42 percent of respondents through external services.

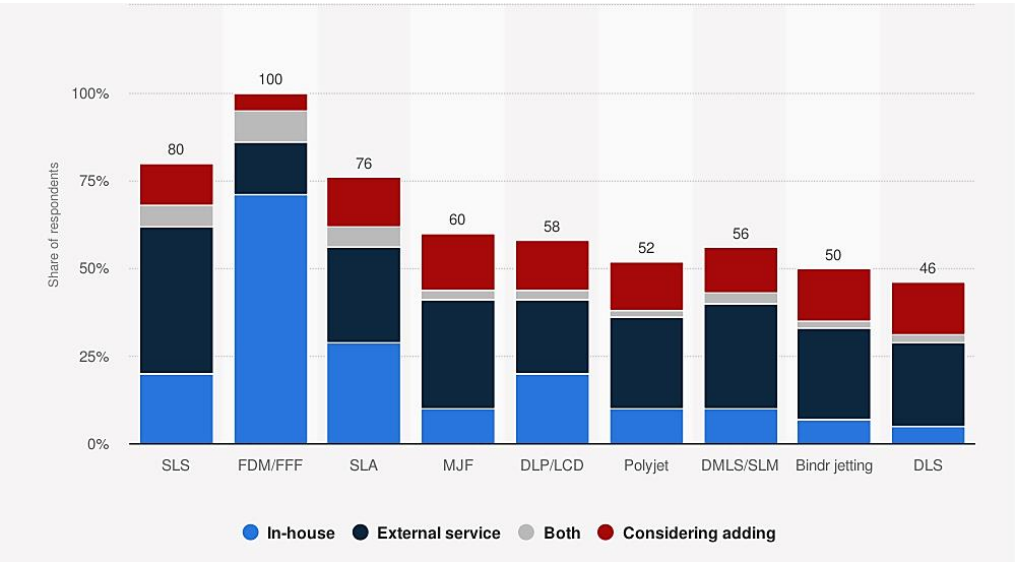

Figure 6 – Most widely used 3D printing technologies worldwide in 2021 (Statista, 2021).

1.6.1 Bone Scaffolds

In severe injuries, the type of tissue and the need for growth hormones limit the body's capability to heal damaged areas. External support is required to repair defects larger than the critical size, and these supports are called scaffolds. To restore the functionality of damaged tissues, organs and joints, invasive surgery is often required by transplantation, repair and replacement of implants and scaffolds [44]. In addition, the utilization of scaffolds is influenced by two major factors: the biomaterial's type and the manufacturing process [45, 46].

From a structural perspective, a scaffold should have a porous structure with sufficient interconnected pore networks and pore size for effective mass-transport activities such as cell nourishment, exchange of nutrients and wastes, and cell migration [47].

These requirements make the scaffold design process (material and geometry optimization) very complex and may make it difficult to customize a scaffold for a specific patient defect, especially when utilizing traditional manufacturing methods. However, 3D printing can fabricate customized scaffolds with precise control on structure and with advanced materials.

1.6.1.1 3D - printed bone scaffolds

A complex, personalized 3D scaffold that matches the defect shape in the anatomical structure can be created using medical image-based modeling (CT scan, MRI), which is an excellent technique when combined with 3D printing. Additionally, the computer-aided design (CAD) model created from medical imaging may effectively and methodically optimize the scaffold material and geometry, minimizing costly trial-and-error testing.

Customized or patient-specific scaffold geometry can be obtained using CAD software along with known individual patient anatomical data associated to the defect

site. In the following, the limitations and challenges of 3D printing technologies will be discussed, and the optimization of the process parameters will be examined to achieve efficient scaffolds.

1.6.1.2 Computer modeling of customized bone scaffolds

There are essentially two separate steps in computer modeling before 3D printing a bone scaffold:

1. Data acquisition
2. Image processing and model generation

1.6.1.2.1 Anatomical data acquisition

Before 3D printing, considerable efforts are required to convert the acquired data into a format compatible with a CAD program. CT scans or MRI technologies are frequently used to gather anatomical information about the fractured bone [48]. Hard tissue imaging is a perfect choice for CT since it produces high-resolution images [49]. However, when soft tissues are involved, MRI is preferred because it can distinguish soft tissue types and the boundaries of tissues with similar densities [50].

As a result, CT scans are a good choice for modeling damaged bones because they are conducted to provide a series of 2D images identifying a density map of the bone that can be converted to 3D images by processing in different software.

1.6.1.2.2 Image processing and model generation

CT scans and MRI are the imaging modalities that contain the data needed to create 3D models. Both generate DICOM data sets. This data collection has three dimensions and contains voxels-similar to pixels in that they store color and opacity-gives it the name "Volume" and has volumetric qualities relating to width, depth, and height. Voxels merge to create a 3D volume, similar to how pixels combine to create a 2D image.

Using this information, the software can be used to choose voxels from a dataset of interest anatomy to produce a 3D volume and then a model. The user can create a "Segmentation" using software like 3DSlicer and InVesalius. Segmenting is the process of creating an identified subset of voxels using a governing characteristic that is shared between them. Threshold segmentation- a technique for carrying out this task-segments all voxels within a specified voxel intensity. Different body tissues and materials will have different voxel intensity thresholds that capture them. This allows it to independently set a voxel intensity to capture bone, air, and soft tissue.

The subsequent step is to export the 3D rendering in a format suitable for creating a functional model, such as STL, which is popular and acceptable. Modifications can be needed to isolate the anatomy of interest from the created model due to the method used to segment the model. Model manipulation techniques include cutting, simplifying, and smoothing the model to achieve the desired final shape. These processes can be carried out using the user-friendly software Autodesk Meshmixer. Figure 7 shows the three general steps to fabricating a 3D medical model.

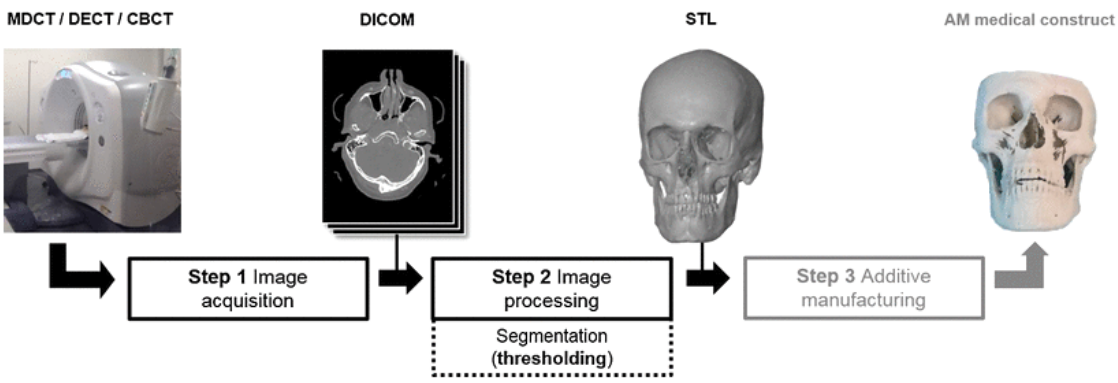

Figure 7 – A flowchart illustrating the procedures required to make a 3D medical structure [51].

1.6.2 Requirements for bone scaffolds

The primary need for scaffold material is interacting with living cells and tissues without inducing unfavorable physiological reactions. The term "biocompatibility" refers to a wide range of factors relating to a biomaterial's function in the human body. Therefore, any device intended for medical purposes should have ISO 10993 (To manage biological risk, the ISO 10993 set entails a variety of standards for assessing the biocompatibility of medical equipment).

Moreover, bone scaffold material is desired to be biodegradable, meaning it can gradually degrade into nontoxic compounds [52]. Other essential aspects that should be considered are [53]:

1. *Osteoconductivity* (Osteoconduction means that bone grows on a surface. This phenomenon is regularly seen in the case of bone implants).
2. *Osteoinductivity* (Osteoinduction is the process by which osteogenesis is induced. It is a phenomenon regularly seen in any type of bone healing process. Osteoinduction implies the recruitment of immature cells and stimulating of these cells to develop into preosteoblasts).
3. *Osseointegration ability* (Osseointegration is the stable anchorage of an implant achieved by direct bone-to-implant contact).

As bone scaffolds degrade gradually, they must have temporary mechanical stability and be able to endure early biomechanical forces such as wound contraction forces and body loads. However, the production process and the used material affect the mechanical strength. Daily activities subject scaffolds to cyclic loads, which can cause fatigue failure [54]. At body temperatures, metals and ceramics have a reasonably high creep resistance because it starts to matter at a temperature that is significantly higher than the body's temperature, or roughly half of their melting point [55].

Fulfilling all these requirements is out of access and under development right now. A bone scaffold with comprehensive functionality requires an optimal porous structure and optimal material ingredients, which can be given by precise advanced manufacturing technology such as 3D printing. This has encouraged scientists to utilize

computers to simulate, optimize, analyze and study complex scaffolds using mathematics, physics, and computer science to predict their behavior in a real system and combine them with 3D printing technologies [56, 57].

1.6.3 Optimization for biomimetic function

1.6.3.1 Internal structure of scaffolds

Unit cells with multi-dimensional/polyhedral shapes can be used as building blocks to construct the internal architecture, which can then be assembled to form a 3D structure. Typically, the porosity of natural bone is gradient, giving the tissue a gradient mechanical strength and stiffness. Long, short, and irregular bones all exhibit radial and linear changes. Therefore, in order to regenerate bone, a porous bone scaffold with a gradient structure is needed [58].

Previous research used FEA-based computer modeling to evaluate the impact of various geometrical designs on scaffolds' mechanical parameters, such as compressive strength, tensile strength, stiffness, and effective bulk or elastic modulus.

Fluid flow analysis is an important part of the internal design of bone scaffolds because of its effect on the transport of nutrients and oxygen into the scaffold structure and cell seeding in the bone healing process. To obtain mechanical and micro-circulation qualities, such as the blood's stress-strain interaction with the scaffold's channels and blood flow velocity, a combination of CAD, FEA, and CFD techniques can be applied [59, 60]. Figure 8 illustrates an example of combining FEA and CAD for printing a scaffold from a mathematical or inspired unit cell.

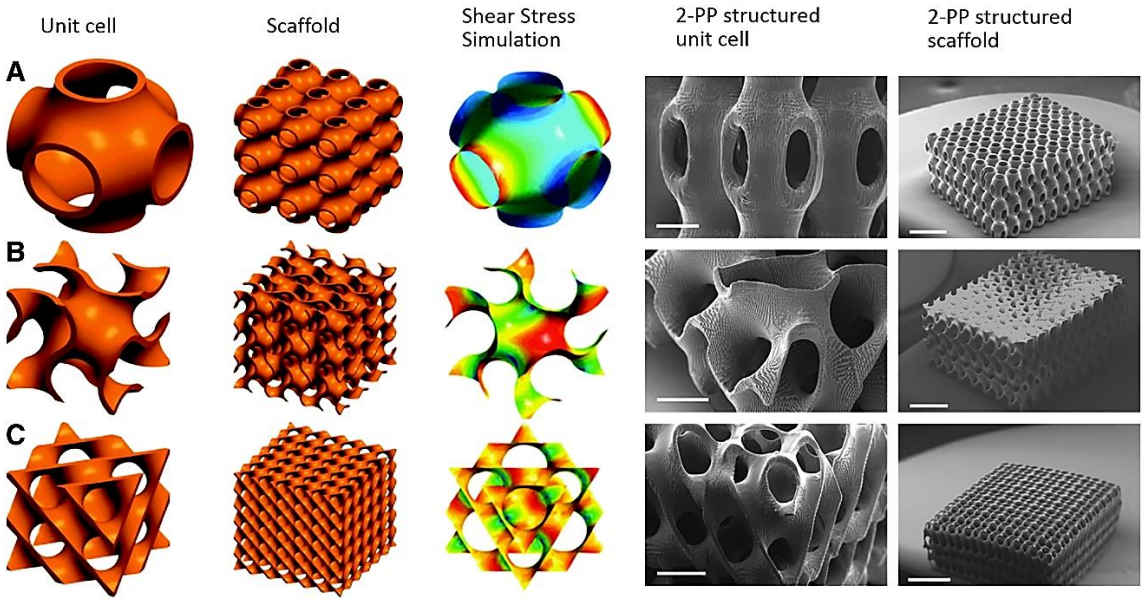

Figure 8 – CAD model of the unit cell, designed scaffold and shear stress simulation, and SEM images of 2-PP polymerized unit cell and scaffold of (A) Schwarz P, (B) Gyroid, and (C) Diamond TPMS [61].

When considering all the variables (pore shape, pore size, porosity percentages, and pore interconnectivity) and various responses (mechanical properties,

permeability, and cell responses), parametric FEA appears to be the most effective method for optimizing bone scaffold geometry.

The difficult challenge of multi-objective optimization with numerous independent variables is the need for an understanding of sophisticated computer modeling and mathematical techniques. The design of experiments (DOE), which has been utilized in the scaffold optimization process mostly for finding optimal hybrid materials or process parameters, is one useful method [62, 63].

The suggested steps for the optimization process of internal scaffold architecture are:

1. Design feature primitive with initial dimensions
2. Design of unit cell
3. Replication of unit cell and generation of a scaffold model
4. Applying material properties and loading and boundary conditions
5. FEA to predict objective functions such as strain energy, elastic modulus, stress distribution, compressive strength, and permeability
6. If the criteria are not met, repeating the first three steps

Mechanobiology is an emerging field of science at the interface of biology, engineering, chemistry, and physics. The shape and motility of cells are influenced by how they are organized, and how cells are organized can be affected by physical forces. This, in turn, then influences the function of the tissue or organ. Mechano-biological knowledge is used by scientists to manufacture scaffolds that would promote the formation of bone tissue in vivo.

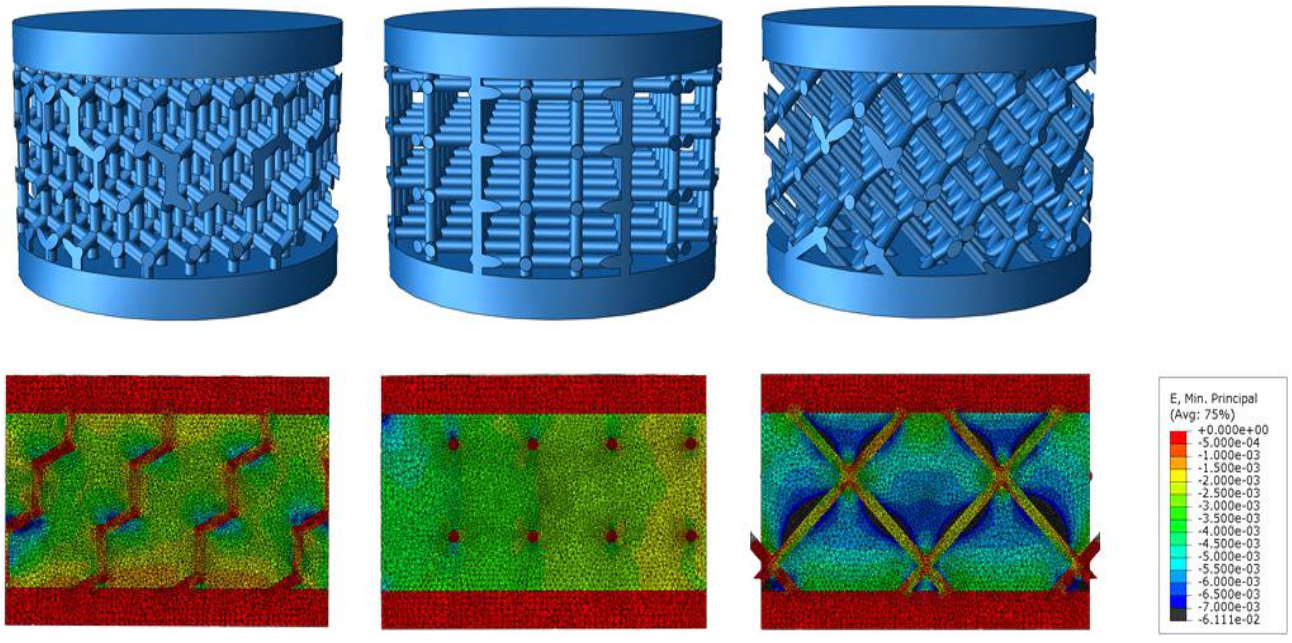

Figure 9 – An example of mechano-biological optimization of scaffolds - mechanical strains within bone tissue scaffolds of different configurations leading to different mechanical environments within the construct [64].

1.6.3.2 Scaffold biomaterials

Biomaterials are natural or manufactured materials that comprise all or part of a living structure or biomedical device [65]. Three individual groups of biomaterials are used to fabricate scaffolds for tissue engineering [66]:

1. Ceramics
2. Synthetic polymers
3. Natural polymers

The existing single-constituent biomaterials fail to satisfy all the requirements and cannot completely replicate the bone properties when used alone. Consequently, developing new hybrid biomaterials, including composites, has become inescapable. Different composites, including polymer-ceramic, polymer-metal, ceramic-metal, and polymer-polymer, have been developed to achieve improved function.

Functionally graded materials (FGMs) are a new generation of composites studied for bone tissue repair [67]. For the first time, the FGM concept in engineering was introduced in 1980 in Japan with the development of graded thermal barrier coatings [68]. FGMs are innovative heterogeneous composite materials composed of two or more materials characterized by a smooth transition from one material to another. According to the desired application, the gradation in composition, structure, and morphology (including arrangement, distribution, dimension, orientation, and interface) may occur in one or more directions.

The fundamental characteristics that a biomaterial should possess in order to run successfully as an implant in the living system are mentioned below [69]:

1. Nontoxicity

A designed biomaterial should serve its purpose in the environment of the living body without affecting other bodily organs. For that, a biomaterial should be nontoxic. Toxicity for biomaterials deals with the substances that migrate out of the biomaterials. In general, nontoxicity refers to noncarcinogenic, nonpyrogenic, nonallergenic, blood compatible, and noninflammatory of biomaterial.

2. Biocompatible

Biocompatibility is generally defined as the ability of a biomaterial, prosthesis, or medical device to perform with an appropriate host response during a specific application.

3. Absence of foreign body reaction

The reaction sequence that generates due to the presence of a foreign body in a living biological system is referred as "foreign body reaction."

4. Mechanical properties and performance

The biomaterial's most important requirement is matching its physical properties with the desired organ/tissue in the living system where it is to be implanted. Therefore, the materials are designed according to the tissue features where they will be used.

1.6.4 Porous scaffolds design

A paradigm shift is happening in the TE scaffold design from manual to CAD-based methods with the fast progress in 3D technologies like stereolithography. Earlier research results show that several architectural characteristics, including pore size and

shape, porosity, and pore interconnectivity, play an important role in biological delivery and tissue regeneration. Therefore, to address biological needs, approaches in scaffold design must be able to create hierarchical porous structures to attain desired mechanical function and mass transport properties and produce these structures within arbitrary and complex 3D anatomical shapes [56].

The well-known existing approaches to modeling the geometry of microstructures like porous scaffold internal architectures include those based on surfaces (boundary representations, BRep) and voxels (discrete volume representation). In the future, it is likely that most digitally designed scaffolds will not be created as homogeneous objects of uniform porosity, same pore size, and same pore shape but will instead be made up of microstructures with spatial variations in porosity, pore size, and pore shape.

Researchers recently started to use TPMS to design TE porous scaffolds to overcome the limitation in the geometry of pore-making elements. The first examples of TPMS were the surfaces described by Hermann Schwarz in 1865 [70], followed by his student E. R. Neovius in 1883 [71]. They described five TPMSs, namely, Schwarz primitive (P), Schwarz diamond (D), Schwarz hexagonal (H), Schwarz crossed layers of parallels, and Neovius (N). In 1970, Alan Schoen, a NASA crystallographer interested in strong but light materials, described 12 more TPMSs [72]. Figure 10 shows CAD designs of six different TPMS structures.

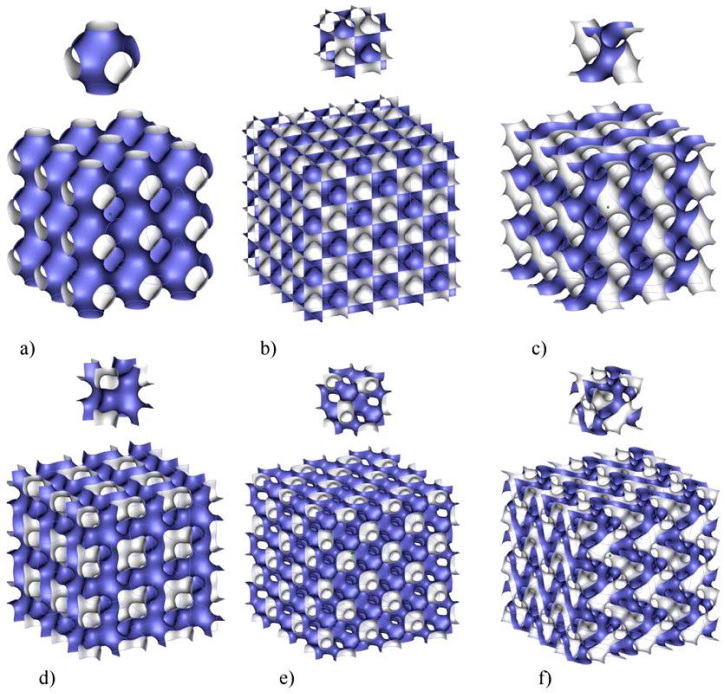

Figure 10 – Examples of CAD designs of TPMS showing one unit cell and 3x3x3 tessellation: a) Schwarz Primitive, b) Schwarz Diamond, c) Schoen Gyroid, d) Schoen I-WP, e) Schoen F-RD, and f) Fischer-Koch S [73].

In the real world, examples of TPMS include some biological structures in nature, block copolymers, and electrostatic equipotential surfaces in crystals. Most

TPMS forms exist as an interface between two phases [74]. Understanding the formation of these delicate structures through biological processes in natural systems inspires the innovative material design and technological applications.

1.6.4.1 Parametric Design

A series of methods based on algorithms is proposed to build a complex porous structure. There are two main methods to design the porous structure according to algorithms, Voronoi-Tessellation, and TPMS.

The unit cell is the basis of the porous structure at a microscopic point using AM technology. Designs are divided into non-parametric design and parametric design. Non-parametric design is structural and geometric design. Parametric design is that cellular structures that are generated according to specific algorithms. Non-parametric design can also be called based geometry design. The non-parametric design was divided into 3D and plane structural-based designs according to the different shapes. The Diamond/FCC, the BCC, and the other polyhedron structure were parts of the design based on the 3D structure. Honeycomb was the most common plane structural-based design [75].

Parametric modeling is an approach to 3D CAD in which a model is built up step-by-step using features and constraints to capture design intent. The parametric modeling process allows for intent and relationships to be created between geometric features, which means the shape of the model changes as soon as a dimension value is modified.

Adding parametric modeling to the engineering process reduces time spent incorporating design changes, as a single parameter can cascade geometric updates throughout the model. The key advantage of parametric modeling is that when setting up a 3D geometric model, the shape of the model geometry can be changed as soon as the parameters such as the dimensions or curvatures are modified; therefore, there is no need to redraw the model whenever it needs a change [76].

This method can help design customized scaffolds suitable for each patient without the need to design from scratch, especially in the bio-printing of 3D bone scaffolds. Hence, parametric modeling can improve, change, and update designs easily, even for non-specialists.

The complexity of the design process limits TPMS-based materials adoption across different research and engineering fields. MSLattice is a complete design platform for users in various engineering disciplines, particularly in 3D printing and computational modeling applications, thanks to these features [77]. MSLattice allows the generation of uniform and functionally graded lattices with cell size grading and relative density grading. Lattices can be based on sheet networks or solid networks. Users can use the program to adjust the TPMS topology type, cell size, relative density grading, and hybridization between lattices.

Using MSLattice is a complementary method for parametric modeling. After acquiring anatomical data from CT scan or MRI and converting them to a 3D model, this program can transform the 3D model into a porous structure, as shown in Figure 11.

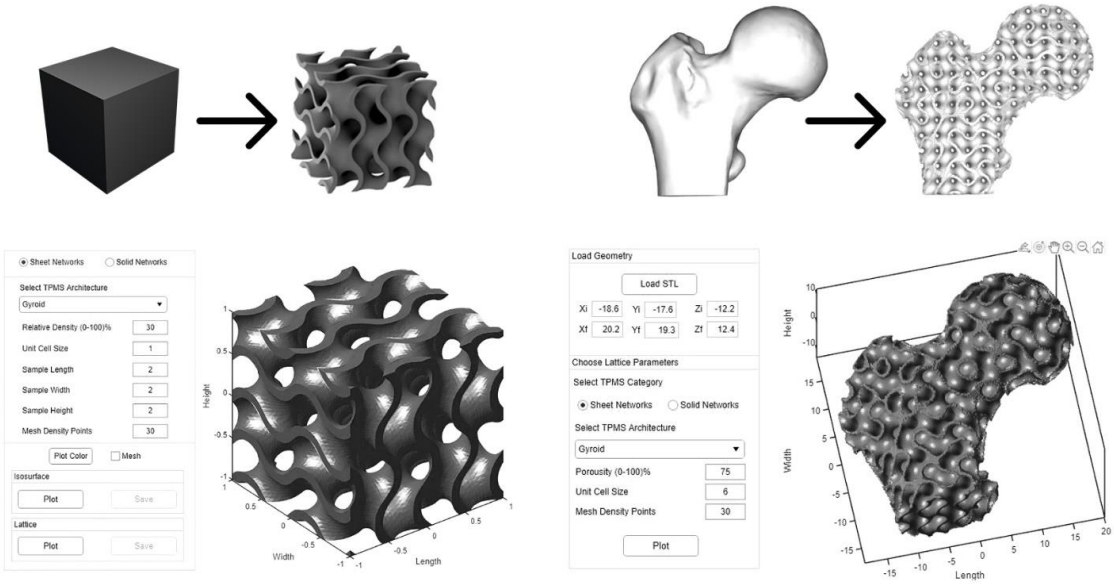

Figure 11 – Steps of converting a three-dimensional Proximal femur model to a porous model with Gyroid structure.

1.6.5 Challenges and future scope

3D printing will become a versatile technique for bone TE in the future, allowing for tailored therapy that provides an opportunity to print with different materials. A qualitative change in the scaffold can be examined for different tissues by modifying the input material. In the distant future, bioprinting will become more common.

The application of porous structures in designing and manufacturing orthopedic scaffolds has a broad future. In order to increase the use of these structures in the orthopedic scaffold substantially, several challenges need to be addressed:

3D printing is still in its early stages and can evolve over time. Print speed is one major limiting factor, and still, traditional techniques are faster, especially in the scale of mass production. 3D printing costs for the mass production of a new drug or a generic prosthetic will be higher due to a lack of economies of scale.

Issues with raw materials are also a limitation. Few materials can be printed with 3D printers; many are not biodegradable and can not be used for medical purposes. Pre-preparation of raw materials and post-preparation of printed structures are costly and time-consuming. Bioprinters do not have enough resolution and precision to create microscopic structures to print living tissues.

Before additive manufacturing spreads and becomes clinically available, several scientific research and medical practice regulations should be adopted. Human rights and dignity must be considered while developing requirements for technological procedures' safety, quality, and efficiency and the final products obtained by 3D bioprinting. The challenge with ethical evaluation and legal regulation of 3D bioprinting is that this technology cannot be thoroughly evaluated using standard clinical trials or the current regulatory requirements.

There is no regulatory regime governing the entire bioprinting process, but some countries have partial TE and regenerative medicine legislation. The issues become even more exacerbated as numerous participants are involved in the production chain of bioprinting. Advanced therapy medicinal products (ATMPs) are human medicine based on genes, tissues, or cells. The principles developed in the ATMPs regulations of the European Commission might be applied to different stages of 3D bioprinting production [78].

Currently, the relations between 3D bioprinting providers, medical organizations, and patients can be settled in the contract for work or medical services. Such contracts can be used in the case of personalized bio-fabrication of organs or tissues for an individual order. However, if bio-printed organs are depersonalized, the sale-purchase agreement can be applied [79].

Copyright infringement refers to the unauthorized reproduction, duplication, distribution, or creation of a derivative work of an original work. With advanced 3D printing technology, any person may scan a copyrighted work and reproduce that original work. Any object scanned without the original owner's permission and printed on a 3D printer may constitute copyright infringement. As with copyright law, if a person takes a product or process and reproduces it with a 3D printer, that may constitute patent infringement. Patent infringement occurs when a party makes, uses, sells, or offers the invention without the patent holder's permission. As a consequence, Trademark infringement occurs under the same conditions.

The impact of 3D printing on the environment is one of the topics that has caused discussion among experts. According to the literature-based study done by Mohd Shuaib et al. [80], as the component's complexity increases, the conventional manufacturing methods' environmental impact also increases with an increase in the manufacturing time to produce the part. They also claim that SM is a better alternative for manufacturing the superficial geometric structures as the material wastage is lessened, build time is quicker, and the environmental footprints and energy consumption is similar to AM.

The fatigue life of most porous structures is still uncertain in current research. Further tests on fatigue life should be carried out under design guidance.

More attempts are needed to be made in the cellular structure. The existing cellular structure could be defective, unable to completely simulate the bone structure. More random mesh structures need to be discovered and manufactured.

Based on the literature review, the following tasks should be done:

- Achieving a synthesis method to obtain HA and CPP powders with optimum crystal structure, morphology, particle size, and biological properties.
- Synthesis of suitable resin for printing the structures using SLA printer with biodegradable functionality and proper viscosity.
- Finding the deficiencies in previous research on the internal structure of scaffolds to achieve a scaffold with the highest mechanical strength and biodegradability and the lowest production cost and time.
- Achieving an effective drug delivery system to deliver the HA/Drug mixtures to the targeted site and release them through time using biocompatible fibrous scaffolds

with antimicrobial properties based on PCL/HA/amoxicillin produced by electrospinning.

- Developing the periodic trigonometric function to model the TPMS structures without the need to know about the 3D modeling knowledge by users. Adding parametric modeling to the process reduces time spent incorporating design changes, as a single parameter can cascade geometric updates throughout the model. Thus, when setting up a 3D geometric model, the shape of model geometry can be changed as soon as the parameters, such as the dimensions or curvatures are modified; therefore, there is no need to redraw the model whenever it needs a change. Using algorithms can help design customized scaffolds suitable for each patient without needing to design from scratch and improve, change, and update designs easily, even for non-specialists.
- Developing a simple method to transform the obtained 2D images from the defected bone using CT scan or MRI to 3D models.
- Examine the mechanical properties of different structures to choose the optimum structure in terms of resistance to pressure and tension to use as a bone refining scaffold.
- Improving mechanical and bio-properties of scaffolds using different orthosilicates as resin precursors.
- Optimizing the Osteoinduction, Osteoconduction, and Osseointegration properties of scaffolds by coating the scaffolds using the SBF solution and HA powder.
- Preparing selected scaffold for in-Vivo tests and using it in the dog's bone, checking the recovery/healing process, and comparing the results with conventional scaffolds.

Conclusion and significance of the study

No previous study has been found on the effect of HA/CPP/orthosilicates as resin reinforcement precursors on the mechanical properties of printed scaffolds, and this study can be used as a basis for further research. Considering HA/CPP directly affects the Osteoinduction, Osteoconduction, Osseointegration and regeneration rate of bone, this composition can be used to find a balance between mechanical properties and the bioactivity of scaffolds.

Traditional medical scaffolds are based on isotropic materials, which in most cases, are less challenging to manufacture, simulate, and procure. The difference between scaffolds made by 3D printers and traditional methods like using molds is that in additive manufacturing, the shapes include user-defined infill geometries, which replace the solid internal volume with a structural lattice known as infill. The most significant effect of infill shape is on mechanical properties such as strength, toughness, hardness, stiffness, hardenability, brittleness, malleability, ductility, resilience, creep, slip, etc.

From the structural point of view, a scaffold should have a porous structure of appropriate interconnected pore networks and proper pore size for efficient mass-transport activities, including nourishment of cells, oxygen, exchange of nutrients, and cell migration. Various tests confirm more cellular activity in the porous scaffolds than in the massive ones.

The previous research on the modeling of the structures is also focused on their mechanical resistance, and there was no case of investigating the effect of the internal structure/infill pattern on the speed of bone formation, which this research on TPMS structures compensates this research gap.

The Cells can immigrate to the site of action using the platform made by scaffolds and form new tissue. Loading the scaffolds with growth factors accelerates cells' differentiation to preferred lineage types to assist in new tissue formation. According to the defined computer-aided design, standard infill percentages are 10 to 25%, which means a scaffold with an infill structure can be printed much faster than a solid scaffold. Furthermore, from an industrial point of view, production costs will reduce as less material is required to produce the object.

Personalized scaffolds can be designed according to each patient's specific and individual defects by converting the two-dimensional images obtained from computerized tomography (CT scan) and magnetic resonance imaging (MRI) to 3D models, which can be modified in CAD software.

In addition to affecting the mechanical properties, the infill geometry also affects drug release from 3D printed scaffolds, and the findings of this research can lead to the design of bone scaffolds with the ability to adjust drug release over time.

3. EXPERIMENTAL METHODS

The quality of raw chemical materials is an essential factor in the production of medical tools because of their direct impact on the mechanical and biological properties of scaffolds, implants, screws, etc. Therefore, some materials such as hydroxyapatite, calcium pyrophosphate, PLA-based resin, triethylene glycol dimethacrylate, Irgacure 819, different metal nitrates, and silicates have been used to make scaffolds. In addition, the following reagents were used:

Orthophosphoric acid 85%, Nitric acid 65%, Disodium phosphate 98%, Polycaprolactone (average M_w ~ 14,000), Dimethylformamide 99.9% and Isopropyl alcohol ≥ 99.7% were purchased from Sigma Aldrich (Sigma-Aldrich Pty Ltd. USA) and used without further purification.

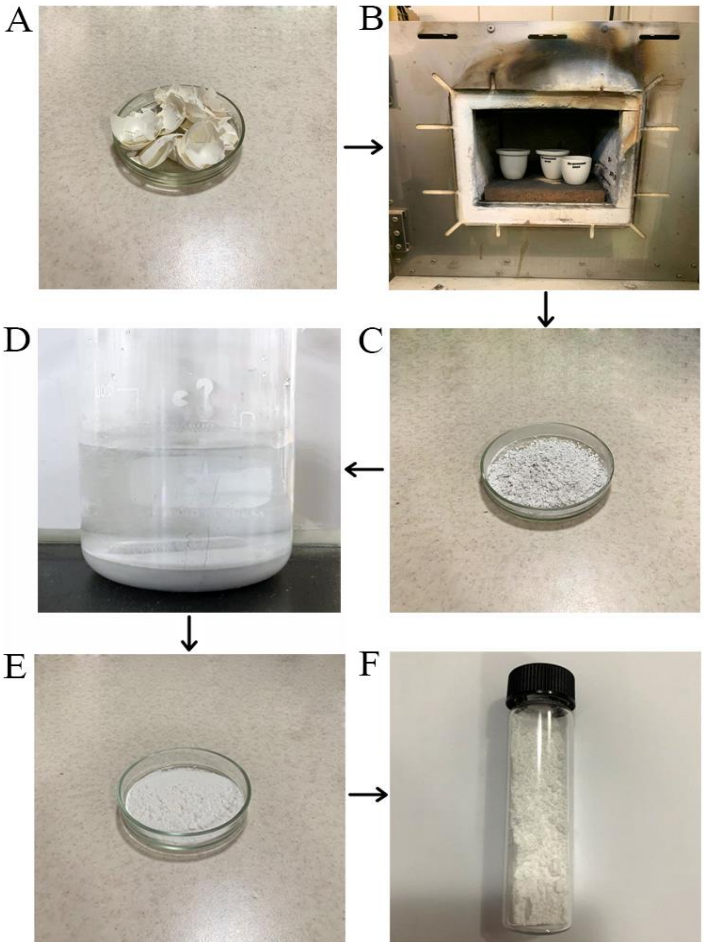

Figure 12 – Synthesis stages of hydroxyapatite A) Eggshell after washing and drying B) Calcination in a laboratory furnace C) Obtained CaO powder D) HA sediment obtained by adding H_3PO_4 to $Ca(OH)_2$ solution E) Deposited powder after aging F) Pure hydroxyapatite after drying in a vacuum and purification in the furnace.

Plant-based and standard translucent UV resins were purchased from Anycubic (Hongkong Anycubic technology Co. China). The wavelength range for the standard

resin is 405 nm and for Plant-based resin is 355-410 nm. As denoted by the manufacturer, the Plant-based resin parameters are:

Hardness	84D	Bending Strength	59 - 70 MPa
Viscosity	150 - 300 MPa.s	Extension Strength	36 - 52 MPa
Shrinkage	3.72 - 4.24%	Vitrification Temperature	100 ºC
Shelf Time	1 Year	Thermal Deformation	80 ºC
Solid Density	1.05 - 1.25 g/cm^3	Elongation at Break	11 - 20%
Wave Lenght	355 - 410 nm	Viscosity	592.0 mPa·s

2.1 Obtaining hydroxyapatite from eggshells waste

Biodegradable hydroxyapatite and calcium pyrophosphate were obtained from eggshell waste.

The initial materials for crystalline HA preparation are orthophosphoric acid (H_3PO_4) and eggshell waste which was used as a calcium-containing component. First, a weighted amount of eggshells (4g) was annealed to 950 °C for two hours with the evaporation of volatile compounds and calcium oxide (CaO) formation.

The resulting CaO powder (2g) was mixed with an aqueous solution of phosphoric acid (6%, 40 mL) under constant stirring for 1 hour, followed by its ultrasonic treatment in an ice bath at 32 kHz for 1 hour until complete homogenization. Finally, the mixture was dried in a vacuum at 110 °C for 24 hours (Figure 12).

2.2 Electrospinning of PCL/HA fibers

Dimethylformamide (C_3H_7NO) and Polycaprolactone ($(C_6H_{10}O_2)_n$) were used to prepare the polymer solution. At first, PCL (1 g) was dissolved in DMF (9.5 mL) under magnetic stirring for 30 min (120 rpm) at 50 °C. Then, HA powder (0.5 g) was added to the solution. The polymer mixture was stirred until its complete homogenization; then, a 10 mL medical syringe was filled with the solution, and the process of electrospinning of polymer fibers was performed at 25 °C; the voltage value was 15 kV, and the precursor feed rate was 0.7 mL/h. Figure 13 illustrates the Electrospinning setup; Figure 14 presents the obtained HA/PCL fibers after electrospinning.

2.3 Electrospinning of PCL/HA/AMX fibers

PCL was chosen as a polymer to produce biologically soluble scaffolds with HA and AMX by the electrospinning method since this polymer is biodegradable, biocompatible, non-immunogenic, non-carcinogenic, and non-toxic, which allows obtaining composite scaffolds that are widely used in tissue engineering. Moreover, the chemical and biological properties of PCL, such as biological compatibility and mechanical strength, make it possible to use it as a replacement for hard tissues in the body, in which healing also takes an extended period.

Polycaprolactone and dimethylformamide were used to prepare the polymer solution for electrospinning. First, PCL (2 g) was dissolved in dimethylformamide (10 mL) under magnetic stirring for 20 min (120 rpm) at 50 °C. Then, HA powder

(0.5 g) and AMX (0.6 mL) were added to the polymer solution. The polymer mixture with the added components was stirred until its complete homogenization; then, a 10 mL medical syringe was filled with the solution. The electrospinning of polymer fibers was performed at room temperature, the voltage value was 15 kV, and the precursor feed rate was 0.5 mL/h.

Solutions for electrospinning were prepared with different ratios of components to study their concentration's effect on the scaffolds' final properties. The experiments showed that an increase in polymer concentration of the solution leads to the formation of fibers with a large diameter, which can be explained by forming fibers' diameter dependence on the electrospinning viscosity [81].

The formation of PCL/HA/AMX scaffolds was conducted via the vertical arrangement of the syringe pump. It should be noted that under the influence of gravity in the horizontal position of the syringe pump, a precipitate is formed in the syringe. In turn, forming a precipitate reduces the solution's viscosity at the needle's exit, affecting the diameter of the polymer fiber. The influence of the solution feed rate, which varied from 1.5 to 3 mL/h, on the diameter of nanoscale fibers is related to the mechanisms of formation of a Taylor cone. At high solution feed rates, the Taylor cone does not have time to be formed, leading to unstable nanoscale fibers.

2.4 Evaluation of the microbiological effectiveness of scaffolds (Fibers)

The antimicrobial properties of bioscaffolds based on PCL/HA/AMX were studied on Staphylococcus aureus and Enterococcus faecalis, which are the prominent representatives of aerobic and facultative anaerobic microflora of the root canals.

Three types of bioscaffolds with different PCL, HA, and AMX contents (PCL with seven wt% of HA and five wt% of AMX; PCL with seven wt% of HA; and pure PCL) were prepared.

Antibiotic-free samples served as the negative control. The obtained samples (15×15 mm^2) were placed in well plates and disinfected by adding 2 mL of 70% ethanol with an exposure time of 30 min; then, they were washed twice with 2 mL of 0.9% isotonic solution. The bacterial suspension of the investigated germs was prepared from several daily colonies grown on nutrient agar in correspondence to the 0.5 McFarland turbidity standard.

To inoculate the nutrient medium, a sterile cotton swab was immersed into the suspension by removing the inoculum excess and seeded onto the surface of Mueller–Hinton agar with dashed movements by rotating the Petri dish. Then, six Petri dishes were used for the study: the reference strain of S. aureus 209P was inoculated on the first three of them, while the bacterial culture of E. faecalis (an archival strain of S.D. Asfendiyarov Kazakh National Medical University) was inoculated on the remaining three dishes. Within 15 min, three samples (one from each type of bioscaffolds) were placed on the surface of the dishes inoculated with S. aureus 209P; the remaining three samples were placed on the dishes inoculated with E. faecalis and incubated in a thermostat at 37 °C for 24 h.

The antibacterial properties were recorded after 24 and 72 hours by measuring the bacterial growth inhibition zone (mm) around the scaffold sample.

2.5 Scaffolds drug release measurements

The scaffolds obtained with the addition of HA and AMX were loaded into flasks with 10 mL of phosphate buffer solution and placed in a horizontal incubator, which was rotated with a rate of 40 rpm at 33 °C. The amount of the released drug was determined using a Varian Cary 300 spectrophotometer under UV irradiation with a wavelength of 272 nm.

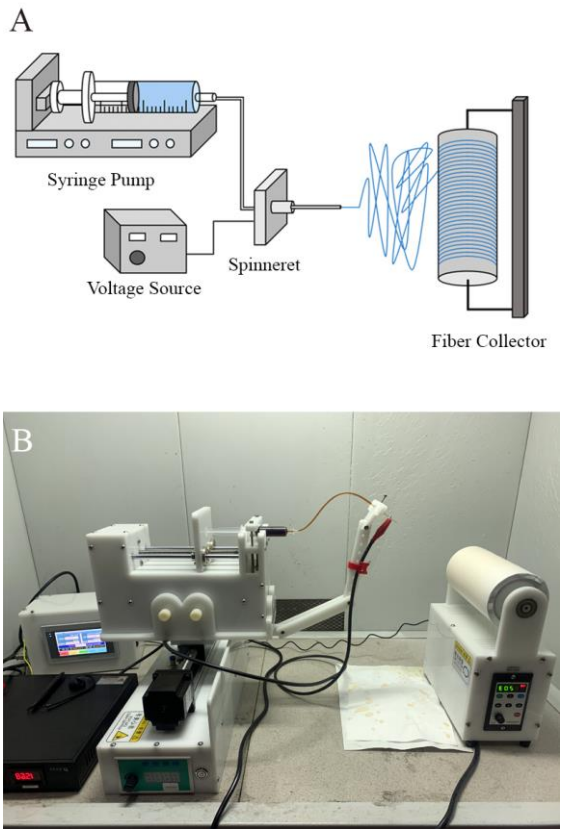

Figure 13 – Electrospinning setup for collecting HA nanofibers A) a simple schematic of setup B) actual setup.

Figure 14 – Obtained HA/PCL fibers.

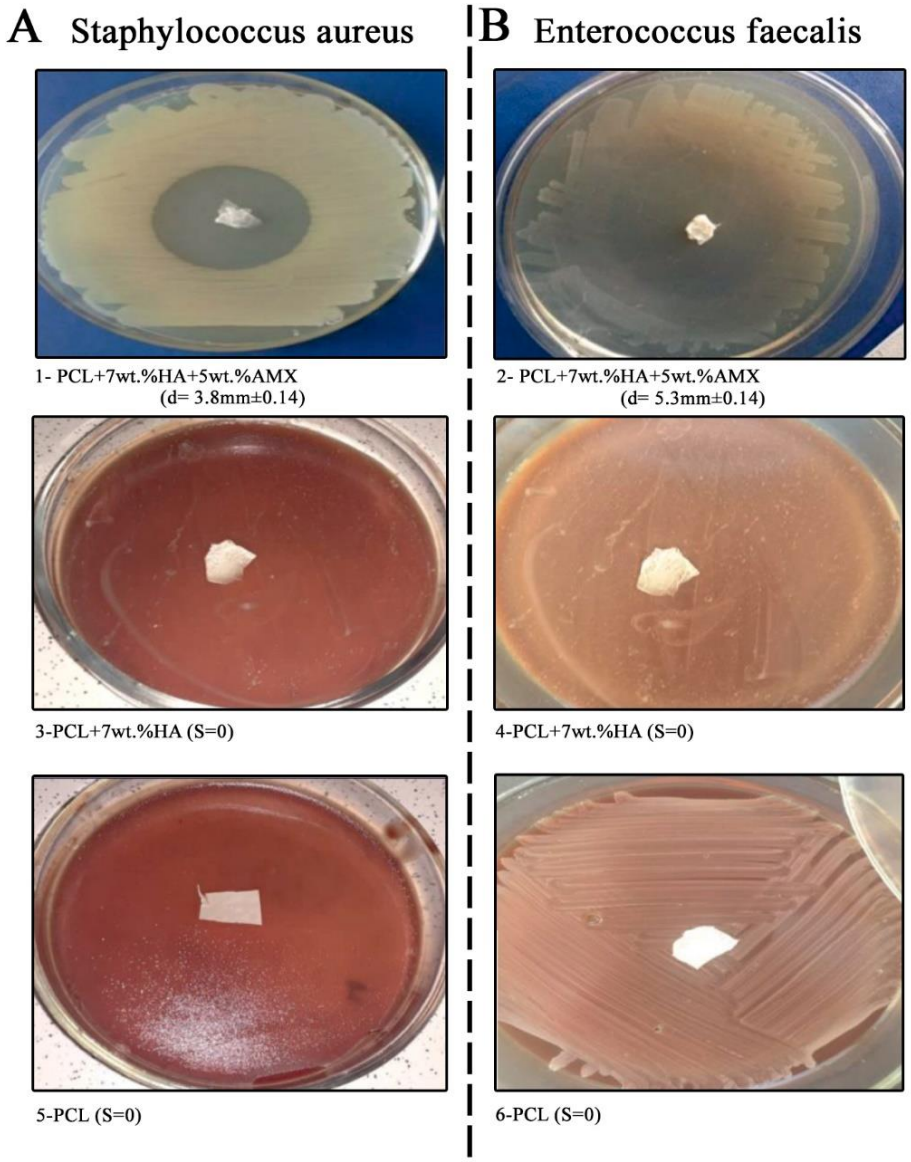

Figure 15 – Inhibition of (A) Staphylococcus aureus and (B) Enterococcus faecalis growth after 72 hours by PCL/HA/AMX-based scaffolds (PCL + 7 wt% HA + 5 wt% AMX). PCL + 7 wt% HA (3,4) and pure PCL (5,6) used as a negative controls [82].

2.6 Obtaining calcium pyrophosphate from eggshells waste

The wet precipitation method was used to prepare calcium pyrophosphate [83]: The inner membrane layer of the eggshell waste was removed using distilled water. Then, it was dried at 100 ºC for 24 h, crushed into powder, and sieved through a 150 mesh sieve. HNO_3 and Na_2HPO_4 were used. The clean eggshell waste was completely dissolved in HNO_3 (1 M) with constant stirring for 2 hours, resulting in a $Ca(NO_3)_2$ (1 M) solution. The Na_2HPO_4 was slowly added to the $Ca(NO_3)_2$ solution, and the solution mixture was vigorously stirred for 2 hours at 50 ºC. The resulting precipitate was vacuum filtered, washed with distilled water, and dried at 80 ºC for 2 hours. Finally, the precipitated powder was calcined in air at 950 ºC for 3 hours using a heating rate of 10 ºC/min.

2.7 Biodegradable resin synthesis

Polylactic acid/Polyurethane was used as oligomer because PLA is made of renewable resources such as corn or sugar cane and is 100% bio-sourced/biodegradable [84], and PLU is susceptible to biodegradation by naturally occurring microorganisms [85]. Phenylbis (2,4,6-trimethylbenzoyl) phosphine oxide, also known as Irgacure 819 was used as an initiator. According to several experiments conducted to investigate the compatible reactive diluent, as shown in table 11, Triethylene glycol dimethacrylate, also known as TEGDMA used as diluent. The final biodegradable resin formulation was 37 wt.% diluent, 62 wt.% oligomer, and 1 wt.% initiator.

Initiator powder was added to the diluent and stirred at 40 °C for 30 minutes. For further dispersion, the solution was poured into PLA-PUA. The formed bubbles during the dispersion were eliminated by further degassing at -1 bar pressure and room temperature for 30 minutes. Eventually, a homogeneous liquid biodegradable UV - curable resin was obtained. Figure 16 shows a schematic of the resin preparation process.

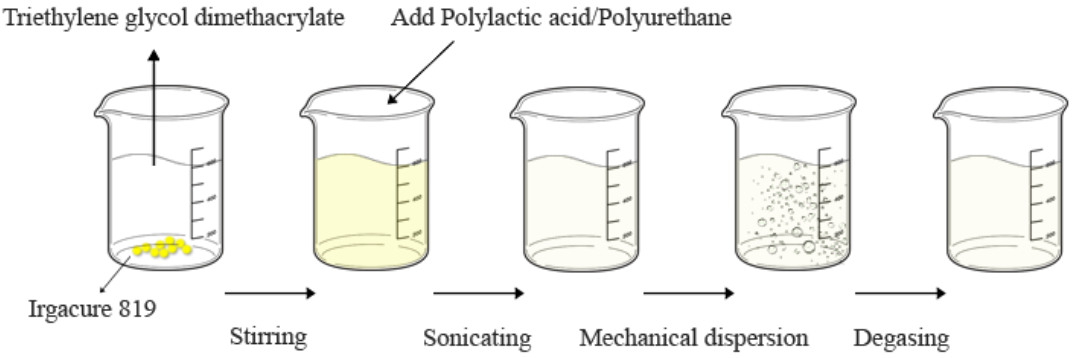

Figure 16 – Schematic of the resin preparation process.

2.8 Designing of Scaffolds

Scaffolds were modeled using Rhino 7. Transforming to a polygon mesh and preparation for 3D printing was done by Autodesk Meshmixer 3.5. 3D Slicer 4.11 was used to convert 2D computed tomography images to a 3D model, and optimization for use in Abaqus was done by Altair HyperMesh 2020. The CT Scan of the femur bone of a 37-year-old patient was received in collaboration with SEMA hospital (Almaty, Kazakhstan) and used as a bone defect model.

TPMS and FGLS structures were designed based on various cell geometries. As the primary goal was to investigate the effect of design variation on the mechanical properties and the geometrical scaffold requirements, such as pore interconnectivity does not depend on the scaffold scale, all scaffolds were designed as cubes with dimensions of 15 mm.

A minimal surface is the surface of minimal area between any given boundaries. In nature, such shapes result from an equilibrium of homogeneous tension. A porous scaffold with controllable pore distribution can be established using a TPMS modeling method.

There are a variety of methods for generating TPMS coordinates, which have an exact parameterized form defined by the Weierstrass formula, as shown in equation [86]:

$$\begin{cases} x = Re\int_{\omega 0}^{\omega 1} e^{i\theta}(1-\omega^2)R(\omega)d\omega \\ y = Re\int_{\omega 0}^{\omega 1} e^{i\theta}(1+\omega^2)R(\omega)d\omega \\ z = Re\int_{\omega 0}^{\omega 1} e^{i\theta}(2\omega)R(\omega)d\omega \end{cases} \quad (1)$$

where ω represents a complex variable, θ is an angle called Bonnet, and R (ω) represents a function that varies with different surfaces. For Schwarz P, Schwarz D and Schwarz G surface of TPMS, R (ω) can be expressed by equation:

$$R(\omega) = \frac{1}{\sqrt{1-14\omega^4+\omega^8}} \quad (2)$$

Compared with parametric TPMS, the periodic surface in approximate TPMS is generally defined and can be expressed as shown in equation:

$$\varphi(r) = \sum_{k=1}^{K} A_k \cos\left[\frac{2\pi(h_k * r)}{\lambda_k} + pk\right] = C \quad (3)$$

where γ represents position vectors of Euclidean space, A_k Represents the amplitude factor, h_k is the k[th] grid vector in the reciprocal space, λ_k Represents the periodic wavelength, pk represents the phase offset, and C is a constant. Some approximate TPMS are listed in Table 7, where the standard values are $\varphi(r)_0$=0, X=2πx, Y=2πy, and Z=2πz.

Table 7 – TPMS models constructed by trigonometric function (circular functions or goniometric functions).

TPMS	Periodic Trigonometric Function
Gyroid	cos(x)sin(y)+cos(y)sin(z)+cos(z)sin(x)=0
Schwarz P	cos(x)+cos(y)+cos(z)=0
Schwarz D	cos(x)cos(y)cos(z)-sin(x)sin(y)sin(z)=0
Schwarz G	sin(x)cos(y)+sin(z)cos(x)+sin(y)cos(z)=0
Lidinoid	0.5(sin(2x)cos(y)sin(z)+sin(2y)cos(z)sin(x)+sin(2z)cos(x)sin(y)) 0.5(cos(2x)cos(2y)+cos(2y)cos(2z)+cos(2z)cos(2x))+0.15=0

As shown in equation 3, the parameters involved in the surface modeling are A_k, h_k, λ_k, pk and the standard value $\varphi(r)_0$=C. The trigonometric parameters adjust the control of the TPMS surface modeling in the function.

Mechanical properties depend mainly on the material and relative density or the so-called "volume ratio".The volume ratio (Vr) of solid-phase expresses how many percent of the cell space is filled by material according to equation:

$$Vr = \frac{Volume\ of\ the\ solid\ phase}{Total\ volume} \times 100\% \quad (4)$$

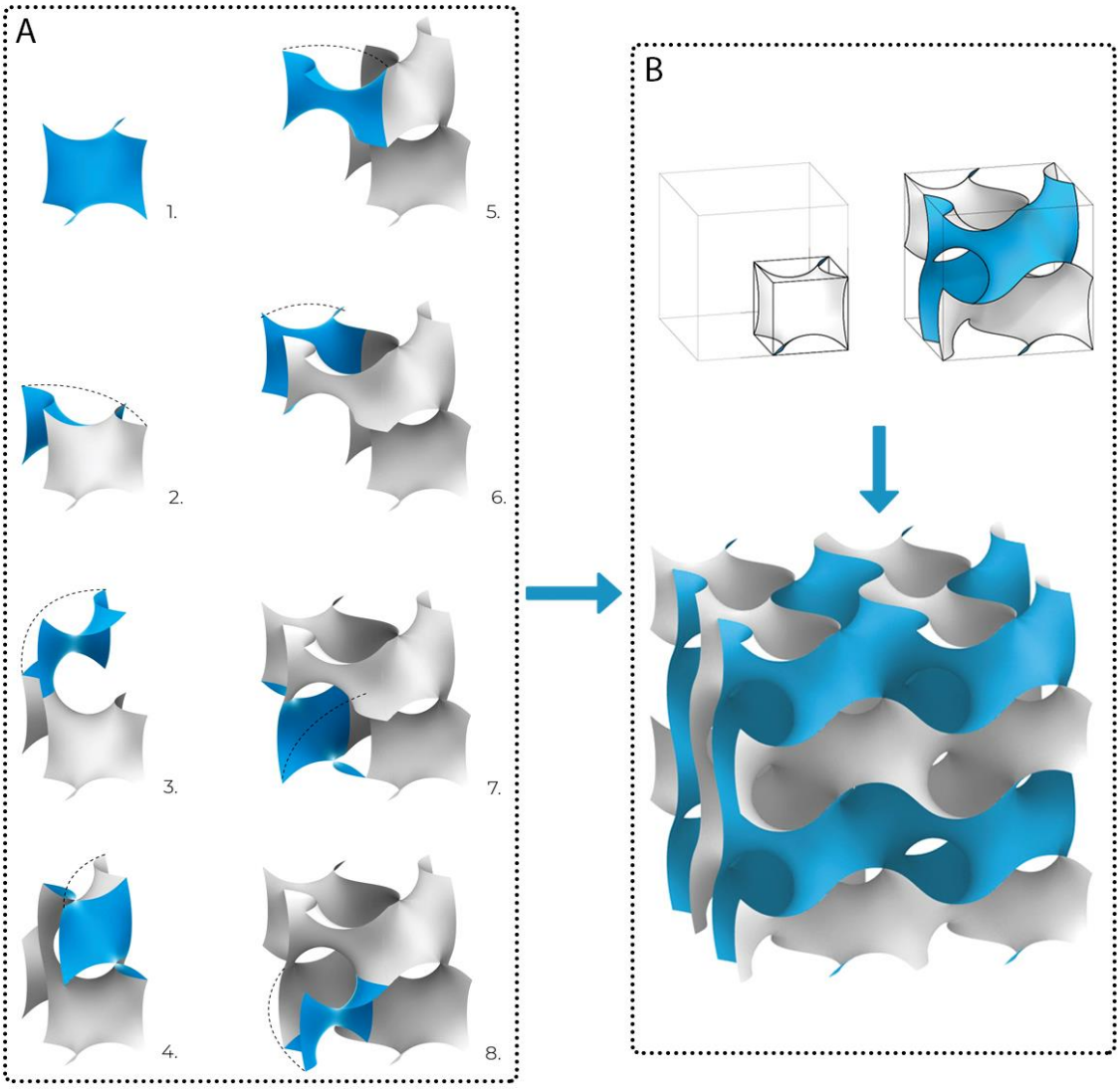

Figure 17 – Evolution of a Gyroid surface from A) Fundamental region to B) Cubic unit cell and final TPMS scaffold.

The following measures were performed to compare the experimental results with the modeling parameters in the software. The porosity and density of the scaffolds were measured using Archimedes' principle and water as the liquid medium. The porosity (P) was calculated according to equation:

$$P = \frac{(Wsat - Wdry)}{(Wsat - Wsus)} \times 100\% \quad (5)$$

The density was calculated according to equation:

$$\rho = \frac{Wdry \times (Pwater - Pair)}{(Wdry - Wsat) + Pair} \quad (6)$$

where:
W_{dry} is the dry weight of the scaffolds
W_{sus} is the weight of the scaffolds suspended in water
W_{sat} is the weight of the scaffolds saturated with water
ρ water is the density of water at 4.0 °C (1.0 g/cm^3)
ρ air is the density of air at 15 °C (0.0012 g/cm^3)

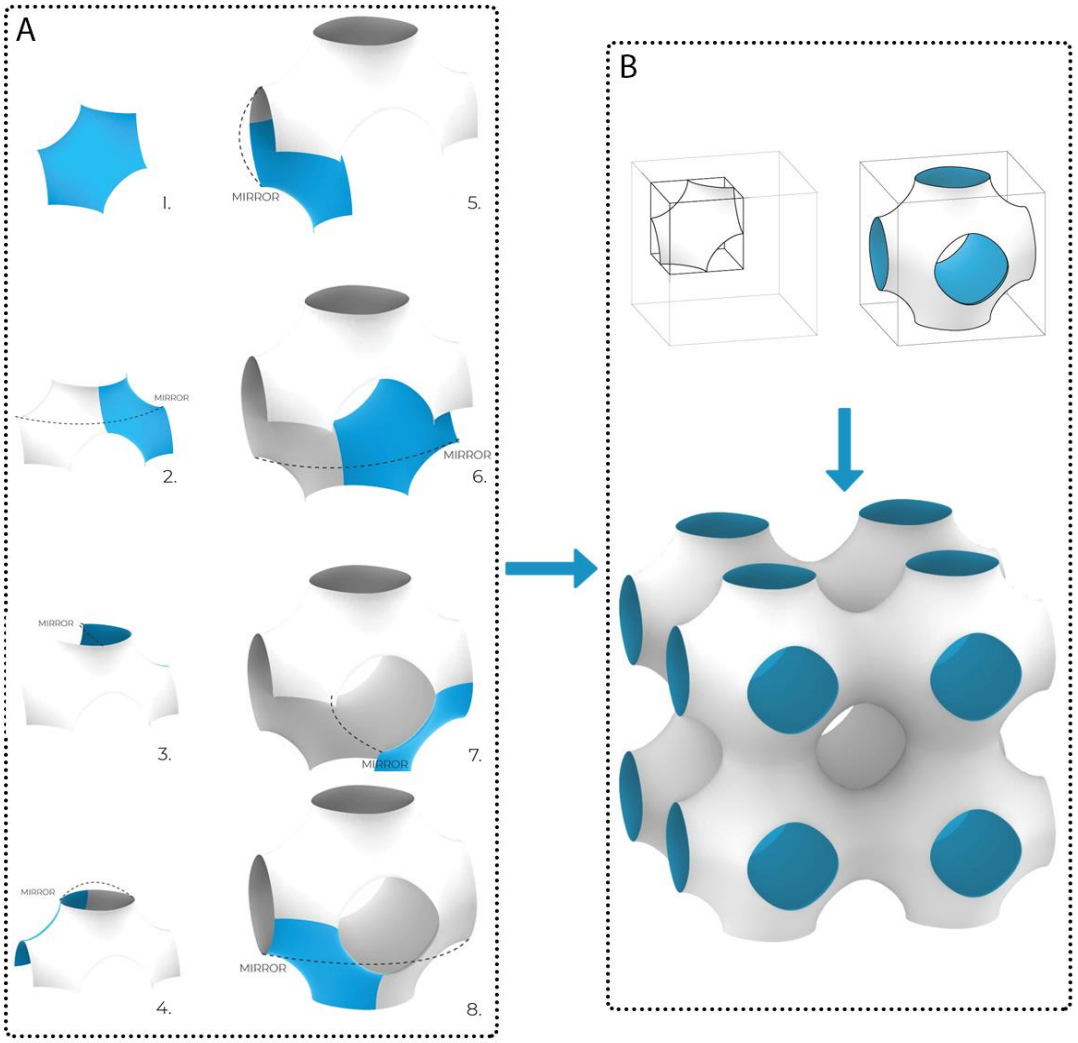

Figure 18 – Evolution of a Schwarz P from A) Fundamental region to B) Cubic unit cell and final TPMS scaffold.

Using Grasshopper (a visual programming language and environment created by David Rutten that runs within the Rhinoceros 3D CAD application) and the 'Iso Surface' component of Millipede, many TPMS can be generated by finding the result of its implicit equation. Standard F (x,y,z) functions of minimal surfaces are defined to determine the shapes within a bounding box. According to the studies, a porous scaffold with controllable pore distribution can be established using a TPMS modeling method. Figures 17 and 18 show the gyroid and Schwarz P surface evolution stages.

Figure 19 shows the parametric design steps of TPMS scaffolds from the elementary cell geometry using the grasshopper plugin in Rhino 7.

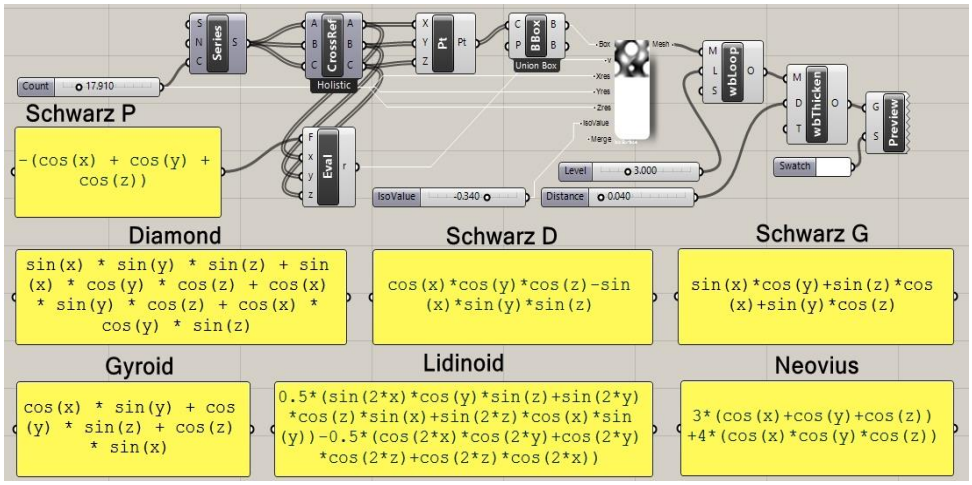

Figure 19 – Parametric design steps of TPMS scaffolds using the grasshopper plugin in Rhino 7 and their periodic trigonometric function.

Figure 20 shows the designed structures using the grasshopper plugin in Rhino 7.

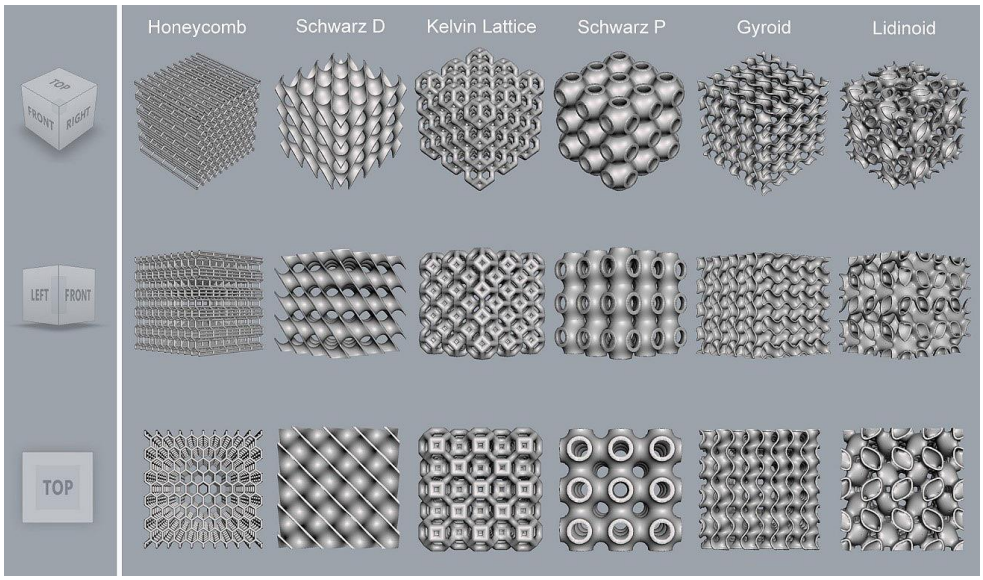

Figure 20 – Designed triply periodic minimal surfaces and functionally graded lattice structures, modeled based on various cell geometries using the grasshopper plugin in Rhino 7.

2.9 Printing of scaffolds

Designed structures were printed at room temperature using the resin made in the previous step. Table 8 presents the printing parameters.

Table 8 – Print parameters.

Layer Height	0.05 mm	Bottom Retract Distance	6.00 mm
Bottom Layer Count	6	Retract Distance	6.00 mm
Exposure Time	8.00 s	Bottom Lift Speed	180.00 mm/min
Bottom Exposure Time	60.00 s	Lifting Speed	180.00 mm/min
Light-off Delay	1.00 s	Bottom Retract Speed	180.00 mm/min
Bottom Lift Distance	6.00 mm	Retract Speed	180.00 mm/min
Lifting Distance	6.00 mm	Resolution	1440×2560 px

In the post-processing stage, printed structures were washed with Isopropyl Alcohol (C_3H_8OH) to remove and dissolve uncured resin from prints without traces or residues. Then printed structures were cured using Anycubic Wash & Cure Machine under the 405 nm UV light for 1 min. Figure 21 shows the final structures after printing.

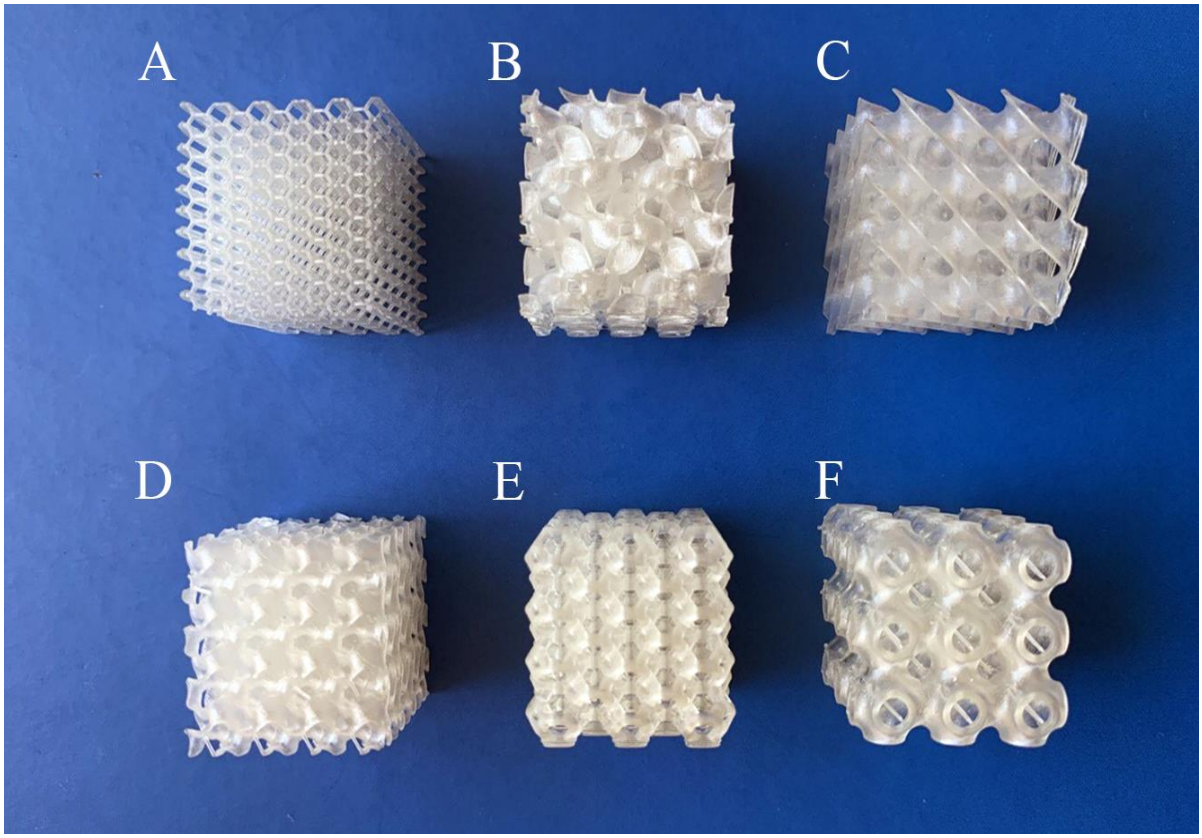

Figure 21 – Top view of printed triply periodic minimal surfaces and functionally graded lattice structures using UV-cured resin without additives and 15mm×15mm×15mm dimension. A) Honeycomb B) Lidinoid C) Schwarz D D) Gyroid E) Kelvin lattice and F) Schwarz P.

2.10 Mechanical properties of scaffolds

2.10.1 Compression Test

Compression test results show the infill shape and volume percentages effect on the mechanical properties of the 3D printed parts. Two groups of scaffolds were printed. In the first group, six scaffolds were printed using biodegradable commercially available resin made from soybean oil as the matrix (made by Anycubic Co.). In the second group, six scaffolds were printed using a mixture of biodegradable UV-cured resin with 5% W/W of hydroxyapatite and 5% W/W calcium pyrophosphate.

2.10.2 Tensile Tests

The importance of tensile loading in the fracture mechanisms of bone has long been recognized. Evans and his colleagues [87, 90] demonstrated with brittle coatings that most bone fractures occur in tension since bone (like most brittle materials) is weak in tension. Brooks et al. [91] also suggested that bone failure is closely associated with planes of maximum tensile stress.

Before tensile testing, the 3D-printed specimens must be conditioned according to ASTM D638 standards. Conditioning them alters the plastic's molecular structure, improving their properties.

The models were designed according to ASTM D638 standard in the form of standard dumbbell-shaped test specimens. This test method is designed to produce tensile property data for the control and specification of plastic materials. These data are also useful for qualitative characterization and research and development. The test specimen shall conform to the dimensions shown in Figure 22 and Table 9 presents the dimensions for all five specimen types according to the ASTM D638 standard.

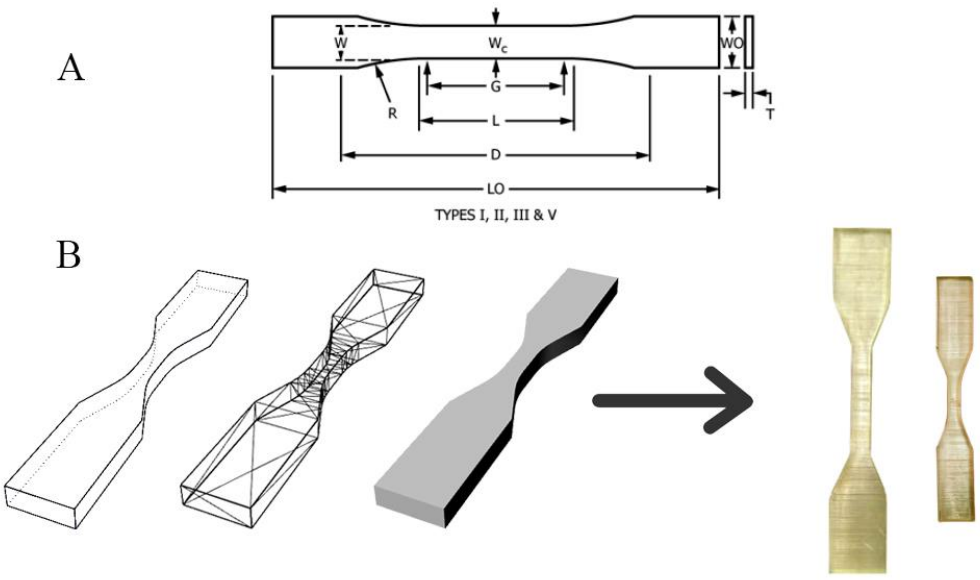

Figure 22 – Dumbbell-shaped test specimen A) design dimensions B) modeled specimens in Rhinoceros 3D and final 3D printed ones.

Table 9 – Specimen dimensions for thickness.

Dimensions (see drawings)	Specimen Dimensions for Thickness, *T*, mm (in.)[A]					Tolerances
	7 (0.28) or under		Over 7 to 14 (0.28 to 0.55), incl	4 (0.16) or under		
	Type I	Type II	Type III	Type IV[B]	Type V[C,D]	
W—Width of narrow section[E,F]	13 (0.50)	6 (0.25)	19 (0.75)	6 (0.25)	3.18 (0.125)	±0.5 (±0.02)[B,C]
L—Length of narrow section	57 (2.25)	57 (2.25)	57 (2.25)	33 (1.30)	9.53 (0.375)	±0.5 (±0.02)[C]
WO—Width overall, min[G]	19 (0.75)	19 (0.75)	29 (1.13)	19 (0.75)	...	+ 6.4 (+ 0.25)
WO—Width overall, min[G]	...	...	...	...	9.53 (0.375)	+ 3.18 (+ 0.125)
LO—Length overall, min[H]	165 (6.5)	183 (7.2)	246 (9.7)	115 (4.5)	63.5 (2.5)	no max (no max)
G—Gage length[I]	50 (2.00)	50 (2.00)	50 (2.00)	...	7.62 (0.300)	±0.25 (±0.010)[C]
G—Gage length[I]	...	...	...	25 (1.00)	...	±0.13 (±0.005)
D—Distance between grips	115 (4.5)	135 (5.3)	115 (4.5)	65 (2.5)[J]	25.4 (1.0)	±5 (±0.2)
R—Radius of fillet	76 (3.00)	76 (3.00)	76 (3.00)	14 (0.56)	12.7 (0.5)	±1 (±0.04)[C]
RO—Outer radius (Type IV)	...	...	...	25 (1.00)	...	±1 (±0.04)

[A]Thickness, *T*, shall be 3.2± 0.4 mm (0.13 ± 0.02 in.) for all types of molded specimens, and for other Types I and II specimens where possible. If specimens are machined from sheets or plates, thickness, *T*, shall be the thickness of the sheet or plate provided this does not exceed the range stated for the intended specimen type. For sheets of nominal thickness greater than 14 mm (0.55 in.) the specimens shall be machined to 14 ± 0.4 mm (0.55 ± 0.02 in.) in thickness, for use with the Type III specimen. For sheets of nominal thickness between 14 and 51 mm (0.55 and 2 in.) approximately equal amounts shall be machined from each surface. For thicker sheets both surfaces of the specimen shall be machined, and the location of the specimen with reference to the original thickness of the sheet shall be noted. Tolerances on thickness less than 14 mm (0.55 in.) shall be those standard for the grade of material tested.

[B]For the Type IV specimen, the internal width of the narrow section of the die shall be 6.00 ± 0.05 mm (0.250 ± 0.002 in.). The dimensions are essentially those of Die C in Test Methods D412.

[C]The Type V specimen shall be machined or die cut to the dimensions shown, or molded in a mold whose cavity has these dimensions. The dimensions shall be:
W = 3.18 ± 0.03 mm (0.125 ± 0.001 in.),
L = 9.53 ± 0.08 mm (0.375 ± 0.003 in.),
G = 7.62 ± 0.02 mm (0.300 ± 0.001 in.), and
R = 12.7 ± 0.08 mm (0.500 ± 0.003 in.).
The other tolerances are those in the table.

[D]Supporting data on the introduction of the L specimen of Test Method D1822 as the Type V specimen are available from ASTM Headquarters. Request RR:D20-1038.

[E]The tolerances of the width at the center W_c shall be +0.00 mm, –0.10 mm (+0.000 in., –0.004 in.) compared with width *W* at other parts of the reduced section. Any reduction in *W* at the center shall be gradual, equally on each side so that no abrupt changes in dimension result.

[F]For molded specimens, a draft of not over 0.13 mm (0.005 in.) is allowed for either Type I or II specimens 3.2 mm (0.13 in.) in thickness. See diagram below and this shall be taken into account when calculating width of the specimen. Thus a typical section of a molded Type I specimen, having the maximum allowable draft, could be as follows:

[G]Overall widths greater than the minimum indicated are used for some materials in order to avoid breaking in the grips.

[H]Overall lengths greater than the minimum indicated are used for some materials to avoid breaking in the grips or to satisfy special test requirements.

[I]Test marks or initial extensometer span.

[J]When self-tightening grips are used, for highly extensible polymers, the distance between grips will depend upon the types of grips used and may not be critical if maintained uniform once chosen.

According to the ASTM D638 standard, For isotropic materials, at least five specimens of each sample should be printed. Tensile characteristics are known to vary on specimen preparation, testing speed, and testing environment. Consequently, these factors must be managed appropriately when precise comparative results are desired.

Temperature and relative humidity generally impact plastics' physical and electrical characteristics in a manner that materially influences test results. Thus, all specimens were conditioned according to the standard practice for conditioning plastics for testing (ASTM Designation: D 618-00) before starting the experiments.

The standard specimen's inside was printed with 100% infill without specific orientations. Tensile testing of the specimens was conducted on Metrotest REM-50 with a 25 kN load cell. All tests were conducted at 20-25 ºC. Built-in linear variable differential transformers (LVDT) were used to measure displacement. Six specimens were tested with different structures. Figure 23 shows the steps of the standard specimen tensile test using the universal testing system.

Figure 23 – Tensile tests of a standard specimen using the universal testing system

The modulus of Elasticity (E =Young modulus in tension) was determined using the following formula [92]:

$$E = \frac{\sigma}{\varepsilon} = \delta = \frac{Stress}{Strain} \quad (7)$$

where:
E is Young's modulus
σ is Tensile stress
ε is Axial strain
δ is Elastic modulus

Tensile stress and strain can be obtained using the following equations:

$$\sigma = \frac{F}{A} \tag{8}$$

$$\varepsilon = \frac{\Delta L}{L} \tag{9}$$

where *F* is the tensile force applied, *A* is the cross-sectional area of the specimen, *ΔL* is the change in length in the loading direction, and *L* is the original length of the specimen.

2.11 Synthesis of resin reinforces precursors using the Sonication technique

Three nano-metallic silicates were synthesized through the ultrasonically accelerated method through the sonochemical method in the presence of TETA (Triethylenetetramine) to improve the scaffolds' mechanical properties and give them Osteogenesis properties. To control the morphology and size in the reaction, the amine of TETA performs two roles: alkaline agent and masking agent. Sonication time and power as significant parameters studied on the product properties.

In the first step, the calculated amount of precursors ($M(NO_3)_2 \cdot xH_2O$ (M = Fe, Mn, Ca)) and Tetraethyl orthosilicate (TEOS) were dissolved in the 20 ml distilled water and mixed with a magnetic stirrer for 30 min. An ultrasonic probe (60 W) set in the obtained solution for 10 minutes. The TETA was added to the reaction medium during the sonication to adjust the pH to 10. The effect of different time duration and sonication power was studied on the samples' structural properties. The precipitate was centrifuged at 3800 RPM for 6 min, then washed and dried at 80 °C for 24 hours, and finally calcinated in the furnace at 800 °C for 8 hours.

2.12 Using SBF to predict in vivo bone bioactivity of scaffolds

SBF solution was prepared with the method explained in reference [93];

Table 10 – Chemical composition of the SBF solution.

Reagents	Amount in 1000 ml	Formula weight	Ion
NaCl	8.035 g	58.4430	Na^+
$NaHCO_3$	0.355 g	84.0068	HCO_3^-
KCl	0.225 g	74.5515	K^+
$K_2HPO_4.3H_2O$	0.231 g	228.2220	HPO_4^{2-}
$MgCl_2.6H_2O$	0.311 g	203.3034	Mg^{2+}
1.0 M HCl	39.0 ml	-	Cl^-
$CaCl_2$	0.292 g	110.9848	Ca^{2+}
Na_2SO_4	0.072 g	142.0428	SO_4^{2-}
$NH_2C(CH_2OH)_3$	6.118 g	121.1356	-
1.0 M HCl	0-5 ml(pH~7.4±0.05)	-	-

Powder reagent chemicals presented in Table 10, Ion-exchanged and distilled water were used to prepare SBF. In the following, 3D-printed scaffolds were soaked in SBF for 24 hours of nucleation times. After nucleation time, scaffolds were taken out, air-dried, and sterilized for 15 minutes under UV light before being used in further research.

2.13 Calcium deposition Test

One important factor is Calcium deposition to investigate the effect of the internal geometry of scaffolds prepared by 3D printing technology on enhancing Osteogenesis. Most previous studies have focused on 2D structures (films and coatings). Previous studies confirm the increase in Osteoblast adhesion and proliferation by soaking the scaffolds in SBF solution [94].

Ca deposition is an important indicator of new bone formation. Quantitative determination of Calcium was done by Nathan J. Castro et al. [94] method using a calcium reagent kit. Briefly, after osteoblasts were lysed, the scaffolds were immersed in a 0.6 N Hydrochloric acid at 37 °C for one day.

After the specified time, the amount of dissolved Ca was measured by colorimetric estimation (reacting with Phthalein Purple ($C_{32}H_{32}N_2O_{12}$) until obtaining the purple solution). The light absorbance of these samples was measured at 570 nm spectrophotometrically. Total calcium deposition was calculated from standard curves of known calcium concentrations versus absorbance in parallel with the experimental samples.

Normalizing Ca deposition was done to remove the contribution of nucleation and indicated as the total mass.

3 RESULTS AND DISCUSSION

3.1 Hydroxyapatite XRD Analysis

X-ray diffraction analysis was performed on the fabricated samples to verify crystal phase recognition and showed that HA and CPP powders are pure (~ 95%). The average crystallite size of the HA and CPP powders was evaluated from the peak broadening of the XRD patterns based on Scherrer's equation (Equation 10), which was 2.21 μm for HA as below:

$$\tau = \frac{K\lambda}{\beta cos\theta} \tag{10}$$

where:
τ is the mean size of the ordered (crystalline) domains
K is a dimensionless shape factor
λ is the X-ray wavelength
β is the line broadening at half the maximum intensity
θ is the Bragg angle

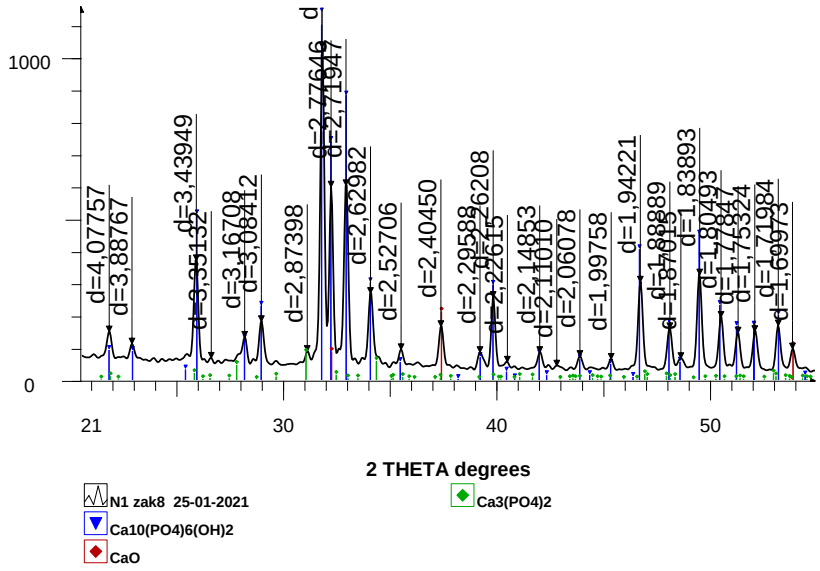

Figure 24 – XRD pattern of HA powders.

XRD analysis on obtained powders shows that HA purity is 94.6 %. The XRD pattern shows peaks of two undesired compounds, CaO and $Ca_3(PO_4)_2$. These impurities can be due to the higher decomposition temperature than hydroxyapatite which can be ignored due to their small amount. For tricalcium phosphate (TCP) preparation, the Ca/P molar ratio of the reagents is 1.5.

During thermal treatment, $CaCO_3$ decomposes to CaO and CO_2:

$$CaCO_3 \rightarrow CaO + CO_2 \text{ (T=850-1000 °C)}$$

Formation of calcium hydroxide as a result of mixing Calcium oxide with an aqueous solution of Phosphoric acid under vigorous stirring:

$$CaO+H_2O \rightarrow Ca(OH)_2+Q$$

Complete reaction after stirring the suspension for one hour after adding the acid:

$$10Ca(OH)_2+6H_3PO_4 \rightarrow Ca_{10}(PO_4)_6(OH)_2+18H_2O$$

HA is the least soluble and least resorbable, whereas TCP is osteoconductive (used as a support for bone repair, then gradually disappears by resorption). Therefore, the presence of TCP does not reduce the efficiency of the obtained powder and has a positive effect on Osteoconduction.

The following reaction can explain the formation of the undesired compound ($Ca_3(PO_4)_2$)) in HA powder:

$$3Ca(OH)_2+2H_3PO_4 \rightarrow Ca_3(PO_4)_2+6H_2O$$

To obtain HA with the required Ca/P ratio close to 1.67 (which corresponds to the formation of stoichiometric HA with good crystallinity and purity) the synthesis process was controlled by maintaining the pH in the range of 6 to 8. All diffraction peaks correspond to the hexagonal structure of synthesized HA and agree with the JCPDS (Joint Committee for Powder Diffraction Standards) data # 96-900-2219.

3.2 Calcium Pyrophosphate XRD Analysis

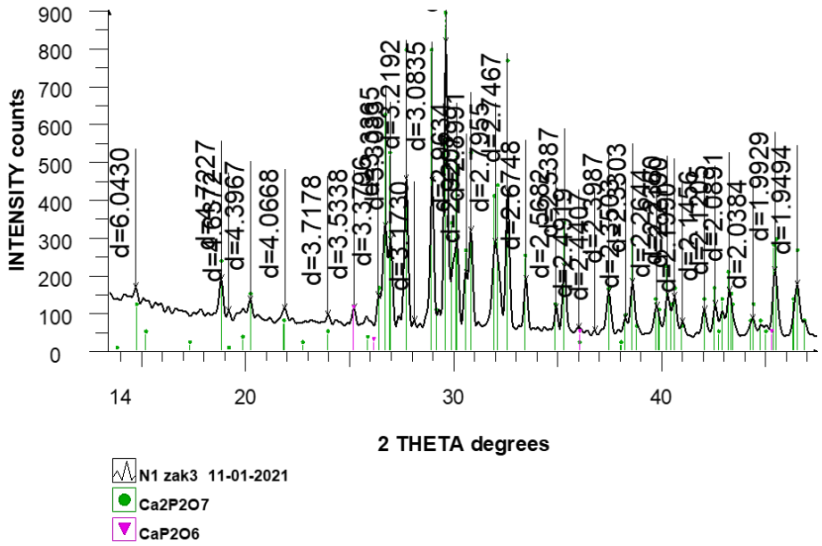

Figure 25 – XRD pattern of CPP powders.

XRD analysis on obtained powders shows that CPP purity is 94.8 %. The XRD pattern shows peaks of one undesired compound (Calcium metaphosphate). Based on Scherrer's equation (Equation 10) and the peak broadening of the XRD patterns, the powders' average crystallite size was 3.11 μm.

The possible formation reactions are as follows:

$$CaCO_3 + 2\ HNO_3 \rightarrow H_2O + CO_2 + Ca(NO_3)_2$$

$$Ca(NO_3)_2 + Na_2HPO_4 \rightarrow CaHPO_4 + 2NaNO_3$$

$$2CaHPO_4 \rightarrow Ca_2P_2O_7 + H_2O$$

Moreover, undesired Calcium metaphosphate can appear during transformation, which can be ignored due to its small amount. CaP_2O_6 is a biodegradable bioceramic and does not reduce the efficiency of the obtained powder and can be used as bone implant coatings [95] and can be ignored due to its small amount.

3.3 EDX analysis of HA powder

Element	W %
O	43.84
C	6.82
P	15.87
Ca	33.47

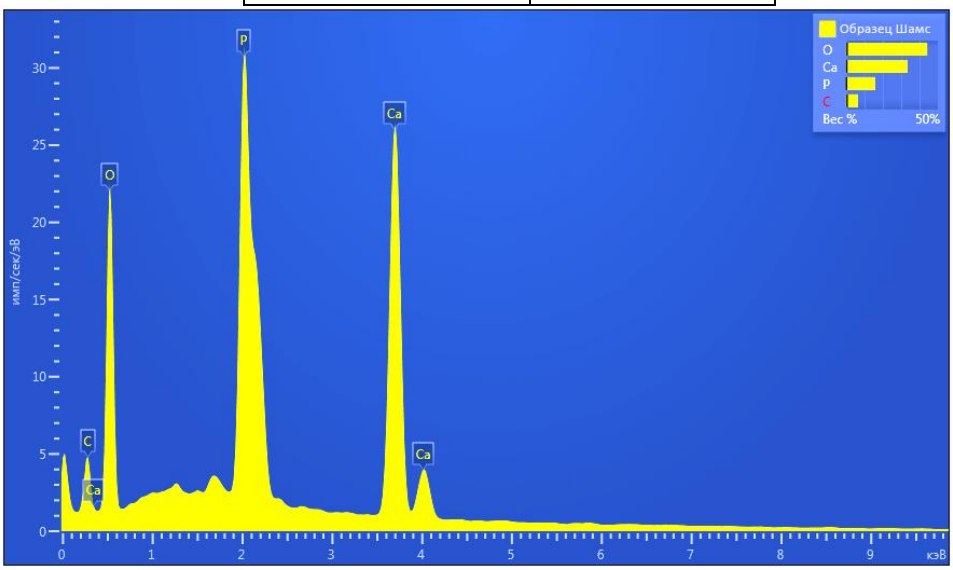

Figure 26 – EDX analysis of HA powders.

Calcium, Carbon, Oxygen, and phosphorus are all expected to be present in bone apatite, and EDX demonstrates the existence of these elements in the sample. According to EDX analysis, the Ca/P ratio is 1.5, which is suitable for medical uses. However, as noted in Chapter 1, an important parameter of synthetic HA is the

Ca/P ratio, Which strongly influences their performance under biological conditions, and chemically pure compounds should be from 0.5 to 2.0 [96].

3.4 FESEM images of HA and CPP powders

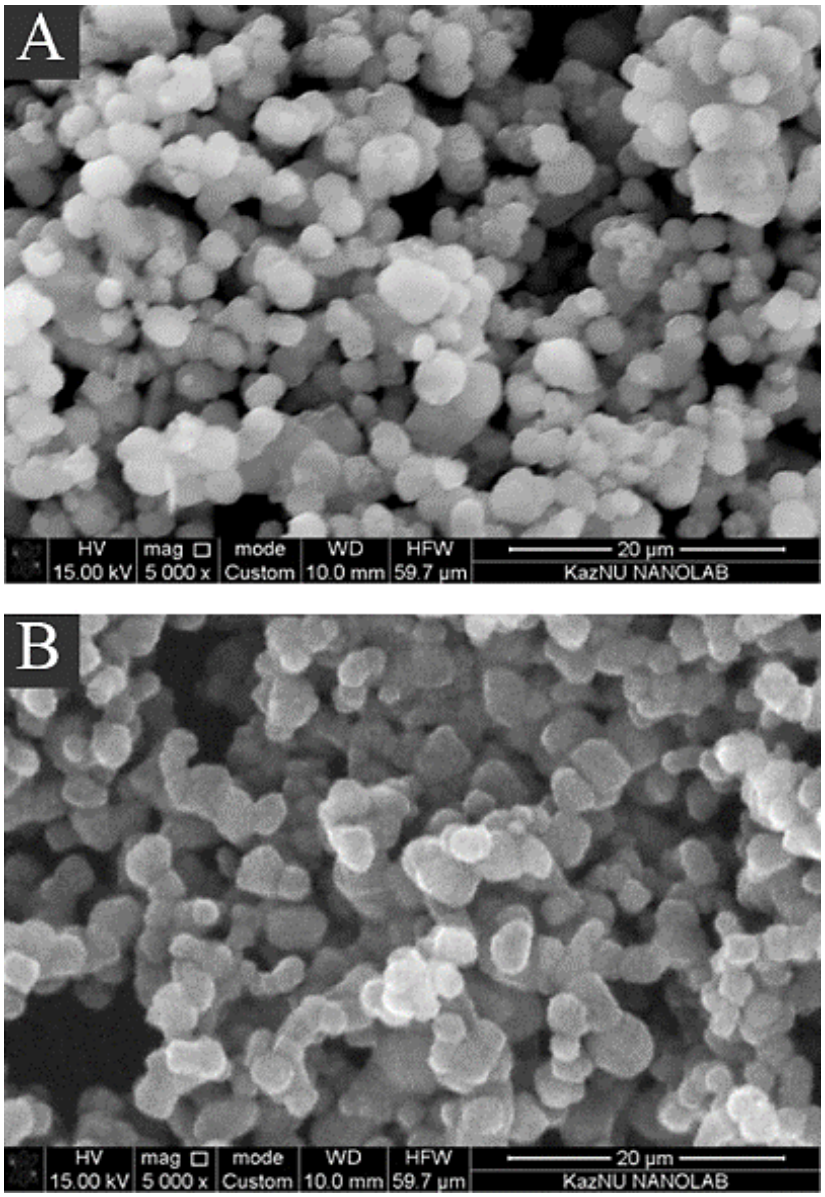

Figure 27 – FESEM images of A) HA and B) CPP powders obtained from the eggshell.

FESEM images of the obtained HA (Figure 27 A) demonstrate the presence of crystals with micron inclusions. The microstructure of samples is presented in the form of angular and bulk crystals, with an average size of 1-2 μm with a rough layered structure and a developed surface morphology. CPP particles (Figure 27 B) with minimum agglomeration, developed surface morphology, and an average size of 2 - 3 μm are suitable for medical applications.

3.5 Electrospinning of PCL/HA/AMX fibers

Figure 28 presents SEM images of the surface morphology of scaffolds based on PCL fibers with additions of HA and AMX and shows filamentous polymer fibers with agglomerates of HA particles with an average diameter of polymer fibers from 100 nm to 200 nm formed in the composite scaffold structure. Although the particles were obtained with an average size of 1–2 μm due to the synthesis of HA powder, the size of the added HA particles was much smaller after electrospinning.

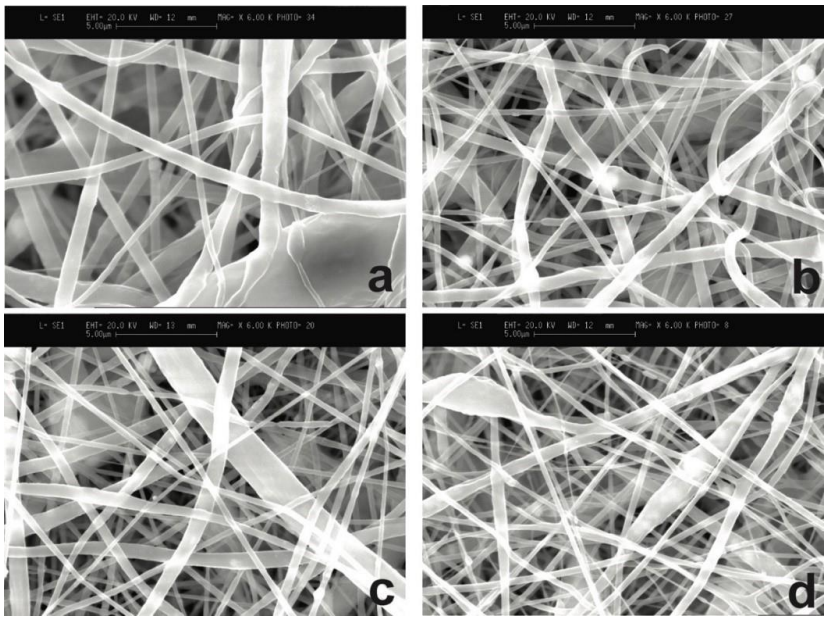

Figure 28 – SEM images of the obtained fibers a) PCL-based fibers, b) PCL-based fibers with the addition of HA, c) PCL-based fibers with the addition of HA and five wt% of AMX, d) PCL-based fibers with the addition of HA and seven wt% of AMX.

3.6 Evaluation of the microbiological effectiveness and drug release of scaffolds (Fibers)

A standard agar diffusion test result revealed significant inhibition of the studied bacterial strains growth around the synthesized bioscaffold (PCL + 7 wt% HA + 5 wt% AMX). In the plates with S. aureus bacterial culture, the growth inhibition zone after 24 h was 3.8 mm ± 0.07. After 72 h, it did not increase in diameter and still was 3.8 mm ± 0.14, with no signs of secondary contamination. The growth of the inhibition zone in the plates with the bacterial culture of *E. faecalis* was 4.5 mm ± 0.04 and 5.3 mm ± 0.14 after 24 and 72 h, respectively [82].

Over time, an increase in the inhibition zone growth indicated a prolonged antimicrobial effect of the synthesized bioscaffold on the specified types of pathogen. It was found that AMX incorporated into the structure of the bioscaffold affects gram-positive cocci *S. aureus* and *E. faecalis*. Moreover, as far as *E. faecalis* is concerned, a prolonged antimicrobial effect is noted. The electrospinning process during the synthesis of bioscaffolds and the presence of HA in its structure does not affect the antimicrobial properties of the obtained material.

As expected, the inhibition zone was not grown in control groups (pure PCL and PCL + 7 wt% HA) after the observation time regarding both studied pathogens. Thus, we show the growth inhibition at day 3 of *S. aur*eus and *E. faecalis*, the prominent representatives of root canals microflora, by antibiotic-containing electrospun scaffold (PCL + 7 wt% HA+ 5 wt% AMX). Two types of samples (PCL + 7 wt% HA) and pure PCL were used as negative control. Thereby significant differences between the indicators of the antimicrobial action of the specified samples were revealed (Figure 15).

The kinetics of AMX release from the scaffolds were observed during four weeks. The resulting drug release curves are shown in Figure 29. The antibiotic release from the scaffolds without adding HA (Figure 29 a) was 25 mg and increased to 42 mg at the end of the observation period. The cumulative percentage of AMX release amounted to about 94% of the total weight of the antibiotic. These observations show that in the case of scaffolds with a thickness of 0.15 mm, the antibiotic is mostly located on the surface of polymer fibers, ensuring its complete release. It was found that when increasing the fiber diameter from 100 nm to 300 nm, the total antibiotic release was 75%over a 4-week observation period. This is because a change in the diameter of the fibers allows the drug to penetrate deep into the scaffold.

The presence of HA in the scaffold structure has practically no effect on the release of the antibiotic. However, studies have shown that the kinetics of drug release depends on the diameter of polymer fibers, their surface morphology, and the drug distribution throughout the scaffold's structure.

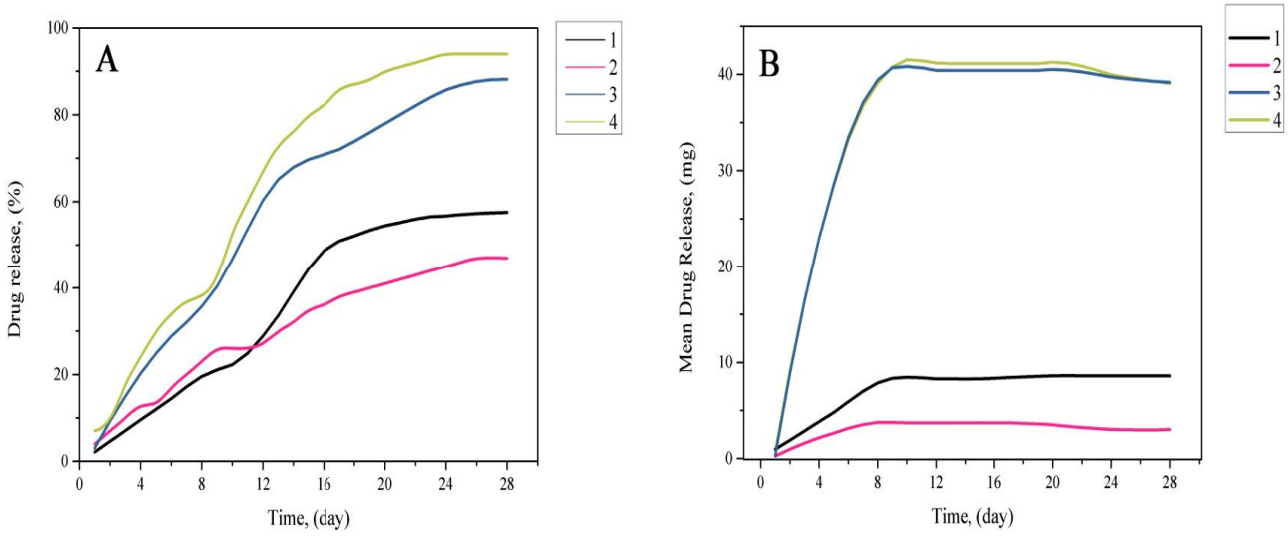

Figure 29 – Kinetics of AMX release in (A) percentage and (B) quantitative terms from the obtained PCL/HA/AMX based scaffolds: (1) PCL/AMX (diameter of fibers 300 nm); (2) PCL/HA/AMX (diameter of fibers 300 nm); (3) PCL/AMX (diameter of fibers 100 nm); (4) PCL/HA/AMX (diameter of fibers 100 nm).

Thus, the obtained results confirm the efficiency of electrospinning for obtaining biologically soluble scaffolds for endodontic therapy. Moreover, the change in HA concentrations and drugs in the resulting scaffolds makes them promising candidates

for biologically soluble scaffolds and other areas such as drug delivery and bone substitute implants.

3.7 Biodegradable resin properties

Viscosity is a crucial factor that affects the quality of printed objects, which can range from 0.25 to 1 Pa.s [97]. At room temperature, the viscosity of the liquid resin was 0.731 Pa.s, respectively, which is appropriate for stereolithography. Figure 30 compares the viscosity of synthesized resin with standard commercial one (Anycubic standard resin) at different temperatures. Viscosity is one of the most significant factors in determining the printing quality and ranges from 0.25 to 1 Pa.s [97]. According to Figure 30 B, with the increase in temperature, the viscosity of both resins decreases and equals ~0.6 and ~0.7 Pa.s at room temperature for standard and synthesized resins, respectively.

Table 11 – The resin formulation and different diluent comparisons.

Diluent formula	Diluent wt.%	Oligomer wt.%	Initiator wt.%	Viscosity	Strength	Toughness
$C_{18}H_{26}O_6$	37	62	1	hight	strong	brittle
$C_{16}H_{30}O_2$	37	62	1	low	medium	ductile
$C_{14}H_{22}O_6$	37	62	1	medium	strong	ductile
$C_{10}H_{14}O_4$	37	62	1	low	very strong	brittle
$C_5H_{10}O_2$	37	62	1	very low	medium	ductile

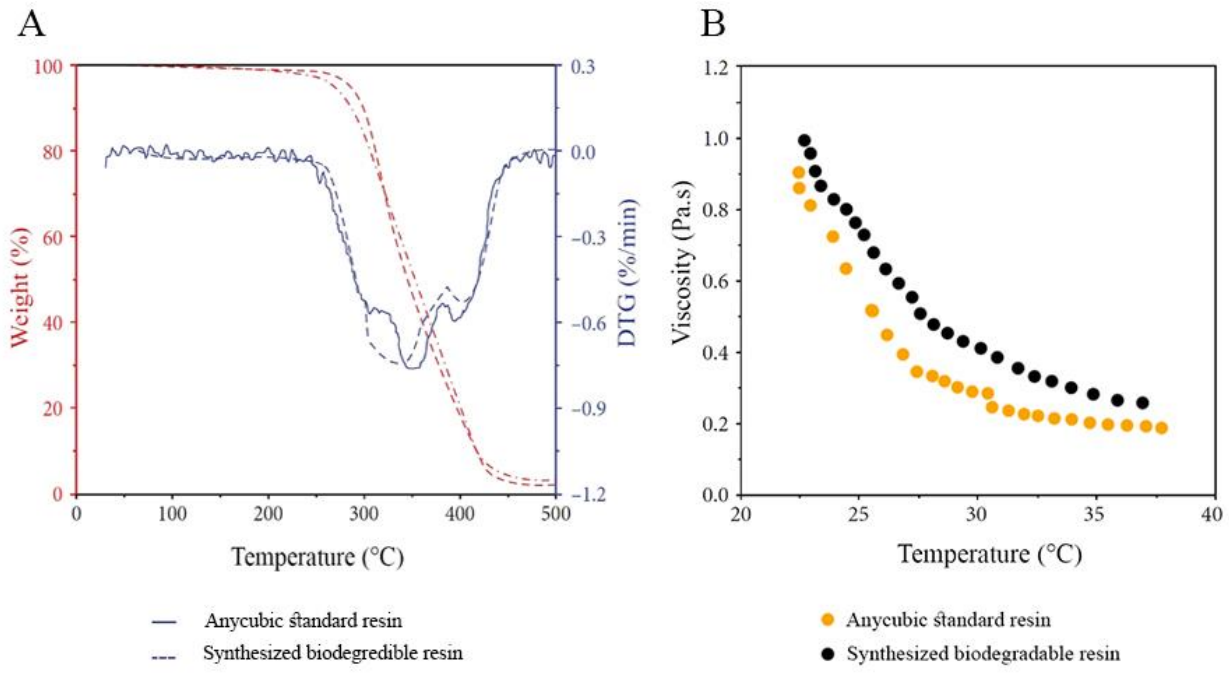

Figure 30 – A) TGA and DTG curves of standard resin compared to synthesized resin B) The viscosities of synthesized resin compared to the standard resin at various temperatures.

As shown in Figure 28, filamentous polymer fibers with agglomerates of HA particles with an average diameter of polymer fibers from 100 nm to 200 nm are formed in the composite scaffold structure. Although the average size of synthesized HA particles was 1-2 μm, the added HA particles' size was much smaller after electrospinning. This particle size decrease can result from the stretching of polymer fibers due to high voltage. It can be inferred that electrical exposure leads to the destruction of HA particles. The presumable reason for this destruction is the action of an electric field, which is concentrated inside a solid dielectric, leading to a decrease in the size of HA particles.

3.8 Mechanical properties of scaffolds that contain HA and CPP

3.8.1 Compression Test

The compression test was performed on both groups, and the results are presented in the table below [98]:

Table 12 – Compression test result for each structure - Structures that contain hydroxyapatite and calcium pyrophosphate are marked with (*).

Structure	**Initial Crack** (N)	**Full Destruction** (N)
Schwarz P	5.184-5.098*	58.184-57.211*
Schwarz D	4.751-4.437*	58.918-57.852*
Honeycomb	4.074-3.909*	58.312-57.714*
Gyroid	4.451-4.152*	57.544-56.709*
Kelvin Lattice	6.029-5.898*	58.240-57.606*
Lidinoid	4.933-4.533*	53.344-52.018*

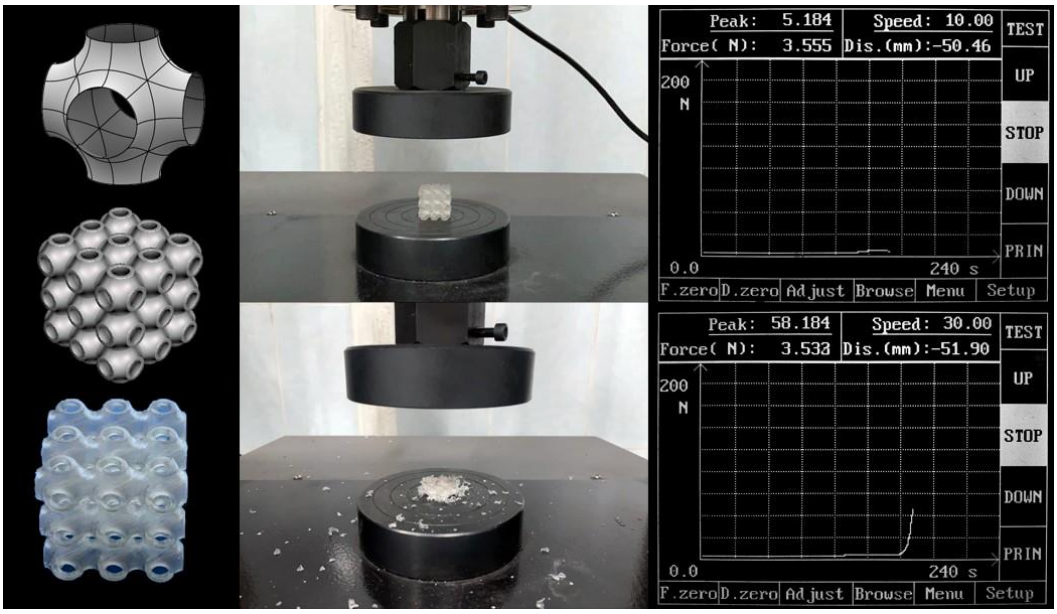

Figure 31 – Compression test on Schwarz P structure done by the universal testing system.

Results show the reduction in compression resistance by adding the resin precursor, and Kelvin lattice has been the most robust structure. Figure 31 shows the compression test steps on the Schwarz P structure as an example.

According to this study, the mechanical properties of 3D printed materials could be enhanced by varying the infill shapes and volume percentages.

3.8.2 Tensile strength

Table 13 presents the individual test results for each specimen.

Table 13 – Individual Tensile test results for each specimen. Specimens that contain hydroxyapatite and calcium pyrophosphate are marked with (*).

Specimen Structure	Precise Width (mm)	Precise Thickness (mm)	Ultimate Stress (MPa)	Elongation at Break (%)	Modulus of Elasticity (GPa)
Honeycomb	9.56- 9.54*	3.19- 3.20*	56.62- 55.94*	2.31%- 2.16%*	3.15- 3.09*
Schwarz D	9.54- 9.55*	3.20- 3.19*	59.68- 58.71*	2.19%- 2.09%*	3.11- 3.07*
Kelvin Lattice	9.58- 9.55*	3.20- 3.20*	59.12- 58.91*	1.66%- 1.57%*	3.13- 3.10*
Schwarz P	9.56- 9.54*	3.21- 3.19*	58.71- 58.01*	2.11%- 2.01%*	3.21- 3.16*
Gyroid	9.53- 9.54*	3.19- 3.21*	60.12- 59.57*	1.74%- 1.65%*	3.19- 3.13*
Lidinoid	9.54- 9.53*	3.21- 3.19*	60.06- 59.32*	2.01%- 1.89%*	3.17- 3.11*

The experimental results confirmed the decrease in specific ultimate tensile strength as the infill percentage decreases, and in particular, the Gyroid structure was more robust than others. Gyroid structures' high porosity and low weight make it an ideal candidate for orthopedic surgery. There is a direct relationship between porosity and tensile strength; with increasing porosity, tensile strength decreases slightly.

3.9 Resin reinforce precursors

The resulting precipitate was centrifuged at 3800 RPM for 6 min, then washed and dried at 80 °C for 24 hours, and finally calcinated in the furnace at 800 °C for 8 hours.

The equations below present metallic silicate nanoparticles' formation through a step-by-step reaction mechanism (M = Fe, Mn, Ca).

$$H_2O \rightarrow H^\circ + OH^\circ$$

$$H^\circ + H^\circ \rightarrow H_2$$

$$H^\circ + OH^\circ \rightarrow H_2O$$

$$OH^\circ + OH^\circ \rightarrow H_2O_2$$

$$H_2O_2 + Si(OEt)_4 \rightarrow Si(OH)_4 + 4C_2H_5OH$$

$$Si(OH)_4 + M(NO_3)_2 \cdot xH_2O + TETA \rightarrow M^{2+} + SiO_4^{4-} + HNO_3$$

$$M^{2+} + SiO_4^{4-} + TETA \rightarrow M_2SiO_4$$

3.9.1 Formation and sonication mechanism

Bubble formation, expansion, and collapse are all functions of ultrasonic that depend on acoustic cavitation [99, 101]. Unstable bubble pressure and temperature can create an ideal environment for nanoscale crystal growth. Consequently, nanoscale structures with favorable surface characteristics are produced by ultrasonic waves. The explosion of bubbles caused shaking waves that spread over the reaction surrounding. A bubble outburst can also rupture the bubble's spherical polarity by producing microjets that impress the surrounding environment. Particle suspension can accelerate within the vibration waves (Figure 32). Interparticle interactions arose the ability to carry out significant modifications in configuration, compound, and reactivity as a result [102].

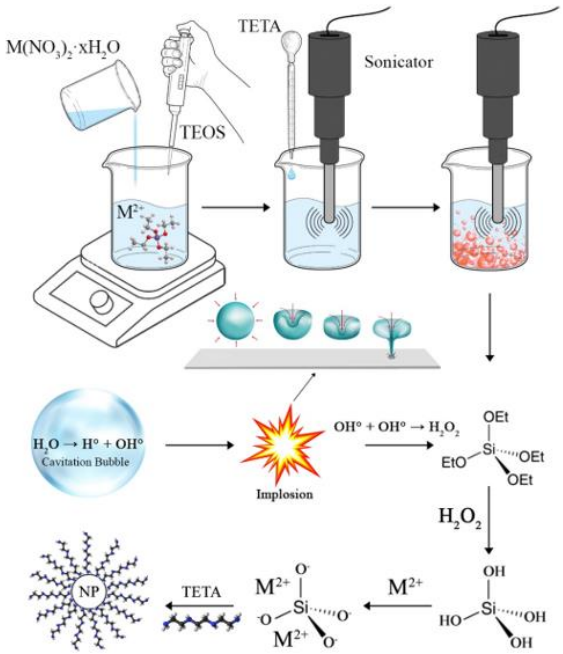

Figure 32 – Illustration mechanism for sonochemical synthesis of resin reinforces precursors nanoparticles M = Fe, Mn, Ca.

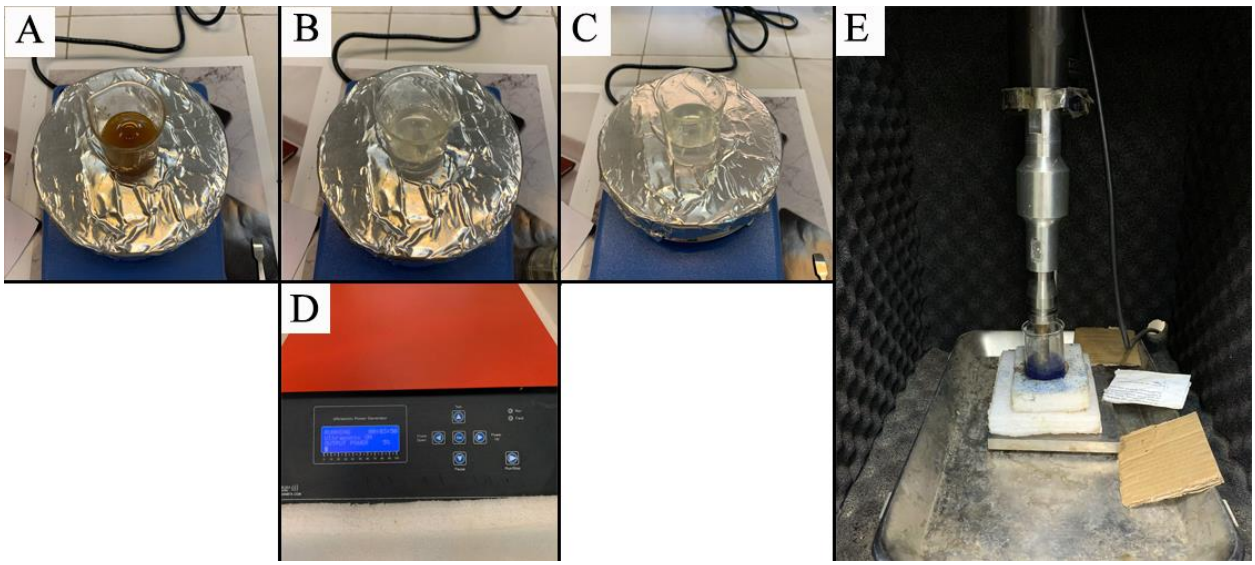

Figure 33 – Dissolved $M(NO_3)_2 \cdot xH_2O$ precursors A) Fe B) Mn C) Ca in distilled water and TEOS, D) sonocation power source and E) sonication step in the presence of TETA.

As shown in figure 34, filled scaffolds can serve as vehicles for delivering bioactive factors to manipulate cellular processes within the scaffold microenvironment.

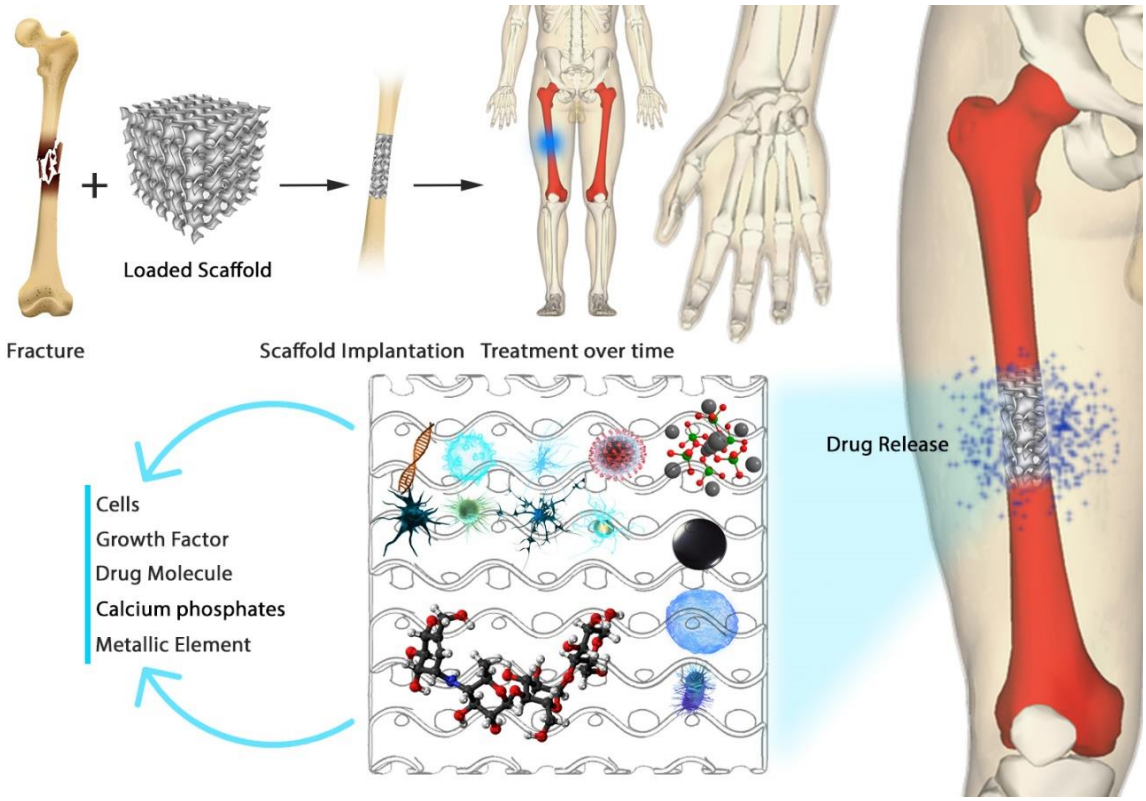

Figure 34 – Schematic presentation of drug release from loaded scaffolds for the targeted treatment of the bone fracture.

Furthermore, the action of TETA will create hydrogen bonds with OH groups on the surface of metallic silicates. TETA could readily adsorb to their crystal facets as a covering agent and independently prevent particle growth. The particle nucleus can grow in all directions. Utilizing a masking agent surrounded by the nucleus controls the particle size caused by growth. Additionally, TETA's long carbon chain prevents aggregation and keeps the particles separate.

3.9.3 Vibrating Sample Magnetometer (VSM) Analysis

There is growing interest in using magnetic materials to accelerate osteogenesis since magnetic fields significantly impact the regeneration process. Furthermore, magnetism results from moving electrons, but organs, cells and tissues have their magnetic fields, and different magnetic fields may interact. Therefore, several scientific studies have focused on magnetic materials' possible health effects [103]. Manganese and Iron orthosilicate are isomorphous with the mineral olivine and are antiferromagnetic at low temperatures [104]. In addition, the effects of magnetic fields and magnetic nanoparticles on osteogenic enhancements have recently been reviewed [105, 106].

VSM is a method to measure magnetic properties based on Faraday's Law of Induction. Magnetizing and demagnetizing soft magnets is simple, exhibiting high saturation magnetization values, low coercivity, and high permeability. Conversely, Hard magnetic materials exhibit high saturation magnetization as well, but they are characterized by high coercivity and are challenging to magnetize and demagnetize [107].

VSM analysis has been done on synthesized Fe_2SiO_4 and Mn_2SiO_4 powders as magnetic resin reinforce precursors. Based on the M-H loop of components (Magnetic hysteresis) illustrated in Figure 36, obtained Ms, Mr, and Hc quantities are presented in table 14.

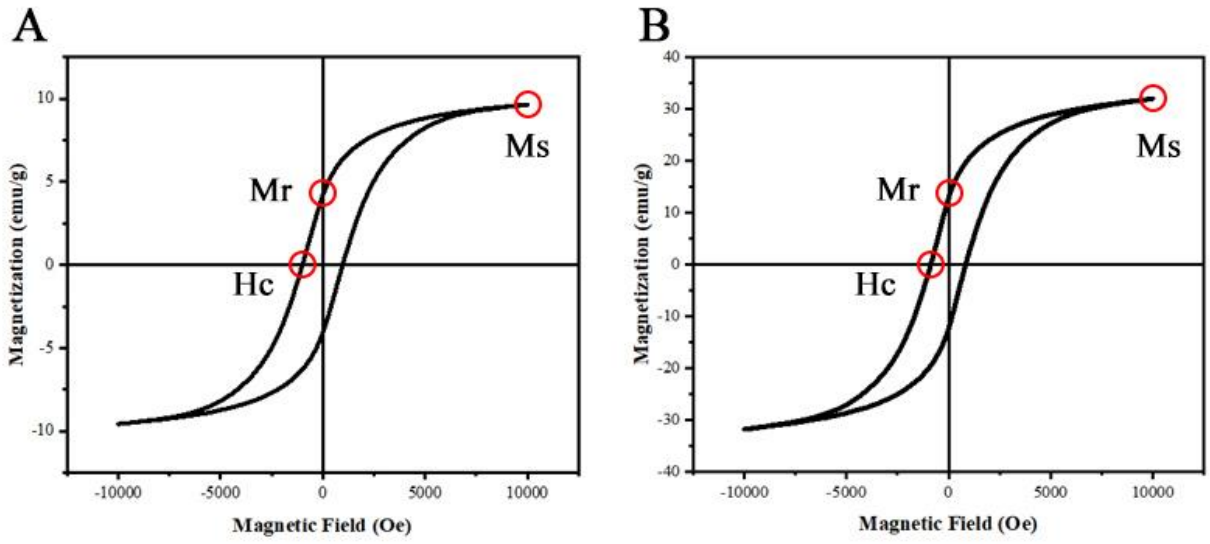

Figure 36 – Magnetic hysteresis loop of A) Fe_2SiO_4 and B) Mn_2SiO_4 powders.

Table 14 – Ms, Mr and Hc quantities of synthesized Fe_2SiO_4 and Mn_2SiO_4 powders.

Compound	Saturation Magnetization (Ms)	Remanence (Mr)	Correctivity (Hc)
Fe_2SiO_4	9.6 emu/g	4.18 emu/g	994.3 Oe
Mn_2SiO_4	32.1 emu/g	12.7 emu/g	862.6 Oe

According to the result, both samples are soft magnetic materials with high permeability and are easy to magnetize and demagnetize. Their primary function is to conduct magnetic and electromagnetic energy conversion and transmission. Previous research shows that nanomagnetic materials can be promising candidates for bone regeneration and enhancing osteogenesis [108, 110].

3.9.4 X-ray Powder Diffraction

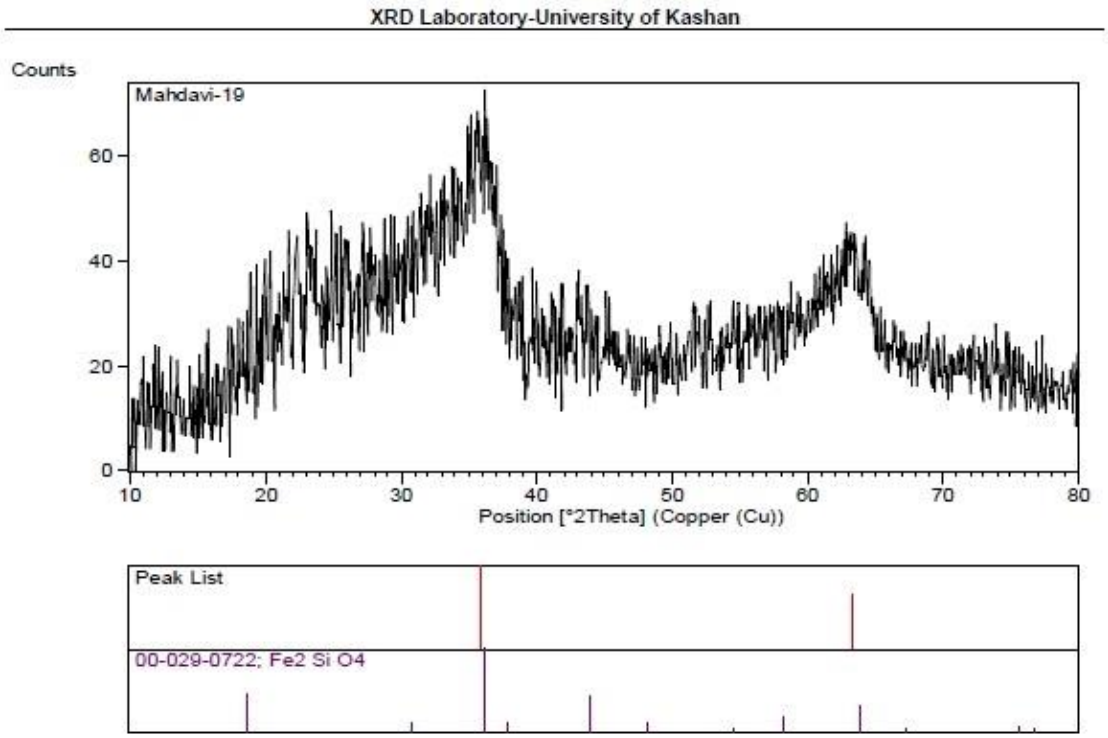

Figure 37 – XRD spectrum of Fe_2SiO_4.

XRD analysis on obtained powders shows that Fe_2SiO_4 purity is 96.6 %. Based on Scherrer's equation (Equation 10) and the peak broadening of the XRD patterns, the powders' average crystallite size was 52.2 nm.

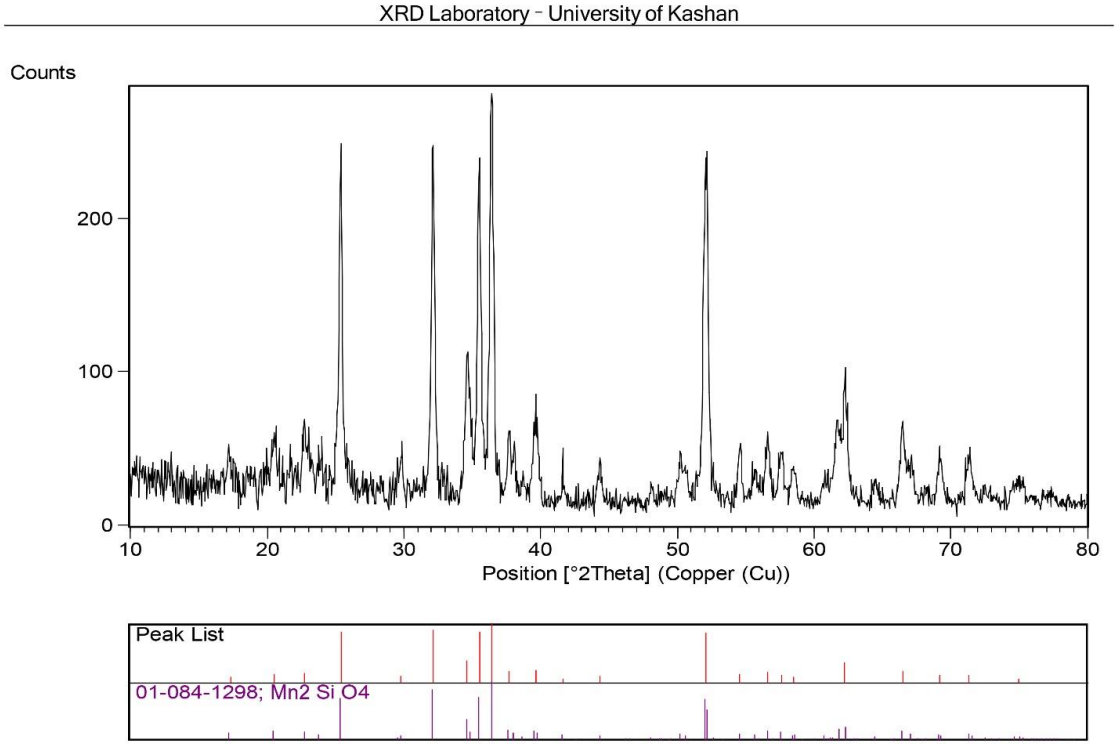

Figure 38 – XRD spectrum of Mn_2SiO_4.

XRD analysis on obtained powders shows that Mn_2SiO_4 purity is 96.8 %. Based on Scherrer's equation and the peak broadening of the XRD patterns, the average crystallite size of the powders was evaluated to be 59.8 nm.

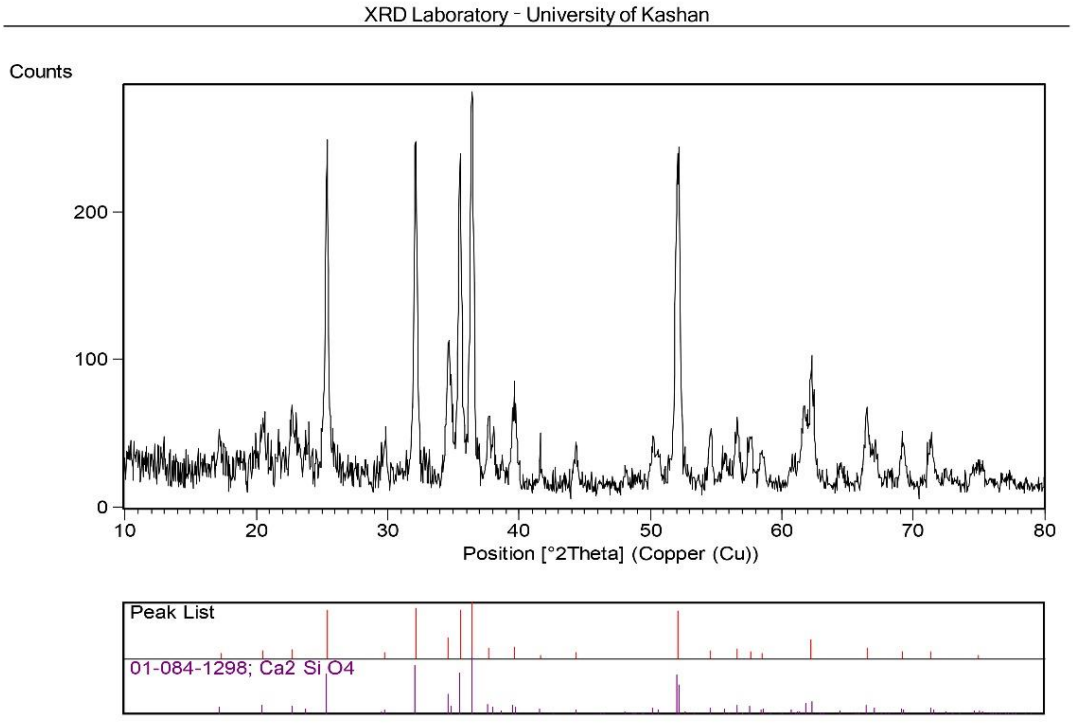

Figure 39 – XRD spectrum of Ca_2SiO_4.

XRD analysis on obtained powders shows that Ca_2SiO_4 purity is 94.4 %. Based on Scherrer's equation and the peak broadening of the XRD patterns, the average crystallite size of the powders was evaluated to be 89.8 nm.

3.9.5 Brunauer-Emmett-Teller (BET) Analysis

Accurate measurement of surface area and porosity is important in many nanostructure applications (such as nanoparticles, etc.). By knowing the average thickness of a molecule, it is possible to calculate the surface occupied by a molecule and measure the total surface area of the sample based on the amount of absorbed substance.

$$\frac{1}{X[\left(\frac{P_0}{P}\right)-1]} = \frac{1}{X_m C} + \frac{C-1}{X_m C}\left(\frac{P}{P_0}\right) \tag{11}$$

The BET Equation uses the information from the isotherm to determine the sample's surface area, where P and P0 are the equilibrium and the saturation pressure of adsorbates at the adsorption temperature, respectively; X is the adsorbed gas quantity while X_m is the monolayer adsorbed gas quantity. C is the BET constant.

$$C = \exp\left(\frac{E_1 - E_L}{RT}\right) \tag{12}$$

where E_1 is the heat of adsorption for the first layer, and E_L is that for the second and higher layers and is equal to the heat of liquefaction or heat of vaporization.

According to the division made by IUPAC, the structure of the porous medium, according to the average size of the holes, can contain holes smaller than 2 nm called Micro porosity, holes between 2 to 50 nm called Meso porosity, and holes larger than 50 nm called the name of the Macro porosity.

Figure 40 illustrates the Fe_2SiO_4, Mn_2SiO_4, and Ca_2SiO_4 nanostructures' correlation N_2 adsorption/desorption isotherms and pore-size distributions.

Figure 40 (A) shows the nitrogen adsorption/desorption isotherm of Ca_2SiO_4. This isotherm is designated as type III based on the IUPAC classification. H3-type hysteresis loop was observed, attributed to Ca_2SiO_4 being mesoporous or microporous. Figure 40 B. shows the size distribution plot of Ca_2SiO_4.

Figure 40 (C) depicts the N_2 adsorption/desorption isotherm of Fe_2SiO_4, which is designated type IV based on the IUPAC classification. H3-type hysteresis was observed, attributed to Fe_2SiO_4 being mesoporous (The pore diameters are between 2-50 nm). Figure 40 (D) shows the size distribution plot of Fe_2SiO_4.

Figure 40 (E) depicts the N_2 adsorption/desorption isotherm of Mn_2SiO_4, which is designated type III based on the IUPAC classification. H3-type hysteresis was observed, attributed to Mn_2SiO_4 being mesoporous or microporous. Figure 40 (F) shows the size distribution plot of Mn_2SiO_4.

Table 15 presents the samples' mean pore diameters, total pore volumes, and specific surface areas.

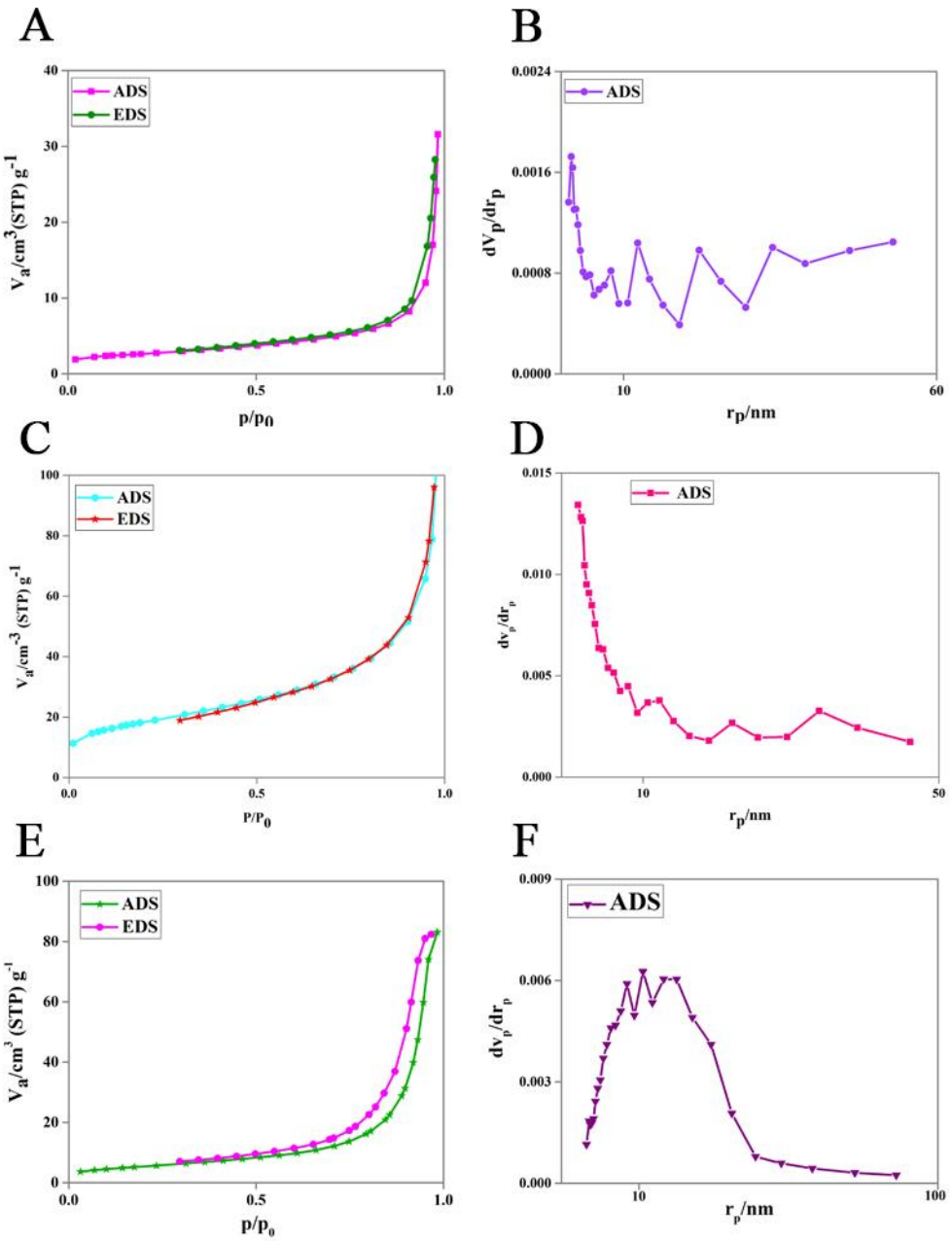

Figure 40 – The samples' pore size distributions and N_2 adsorption/desorption isotherms.

Table 15 – The surface characteristics related to the nano precursors.

Sample	BET surface area ($m^2\ g^{-1}$)	Pore volume ($cm^3\ g^{-1}$)	Mean pore diameter (nm)
Ca_2SiO_4	1.84	0.44	16.80
Fe_2SiO_4	1.66	0.41	34.22
Mn_2SiO_4	1.71	0.44	42.45

The estimated pore size and other BET data are in accordance with the FESEM results (Figure 41).

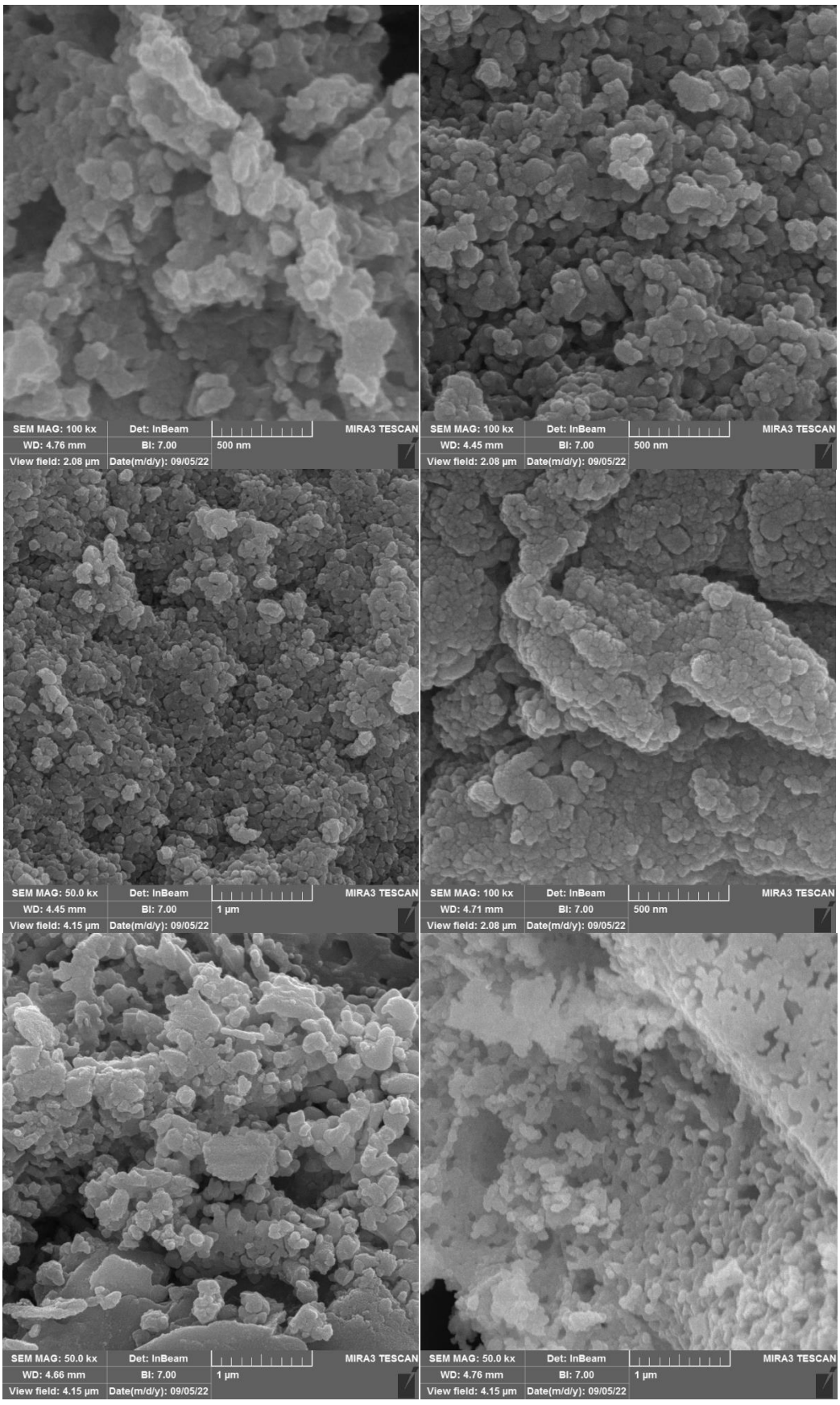

Figure 41 – FESEM images of A) Fe_2SiO_4 and B) Mn_2SiO_4 C) Ca_2SiO_4 powders.

FESEM images of the obtained Ca_2SiO_4, Fe_2SiO_4, and Mn_2SiO_4 (Figure 41) indicate the presence of crystals with nano inclusions. The samples' microstructure is presented as angular and bulk crystals, with an average size of 94 nm with developed surface morphology and minimum agglomeration.

3.10 Using SBF to predict in vivo bone bioactivity of scaffolds

A solution with an ion concentration similar to human blood plasma is known as simulated body fluid (SBF) [111, 112]. The ability of apatite to form on a material's surface in an SBF solution with ion concentrations almost equal to that of human blood plasma is frequently used to assess the bone-bonding ability of a material.

Tadashi Kokubo (Chubu University, Japan) in 1991 proposed that the essential requirement for an artificial material to bond to living bone when implanted in the living body is the formation of bonelike apatite on its surface, and this means that the apatite formation on a material surface in SBF can be used to predict the in vivo bone bioactivity of that.

The surface of implants has been treated using various techniques to improve cell adhesion. Specifically, it has been found that immersing TPMS scaffolds in SBF promotes the formation of osteogenic apatite, which improves bone cell attachment [113] and induces mineral nucleation resulting in apatite formation upon the materials' surface and enhanced cellular behavior [93].

Additionally, by increasing surface area, surface roughness, and focal adhesion points, forming an apatite layer on the surface modifies the bulk material's mechanical characteristics and promotes better cell attachment between the material and native bone cells [114].

Consequently, HA-coated TPMS scaffolds can be quickly used after SBF nucleation for bone tissue regeneration because they enhance proliferation and cell adhesion [81, 82]. In addition, because of their biodegradability, native cell populations can absorb and replace them [115].

One important factor is Calcium deposition to investigate the effect of the internal geometry of scaffolds prepared by 3D printing technology on enhancing Osteogenesis. Most previous studies have focused on 2D structures (films and coatings). Previous studies confirm the increase in Osteoblast adhesion and proliferation by soaking the scaffolds in SBF solution [94].

3.11 Calcium deposition

Figure 42 shows the total calcium deposition on different scaffolds during various nucleation times.

According to the results, in all samples, the amount of calcium deposition is directly related to the nucleation time in the SBF solution and increases with the immersion time.

Lidinoid had the highest total calcium content in long and short periods, and it seems that seven days of nucleation time can be suitable as needed.

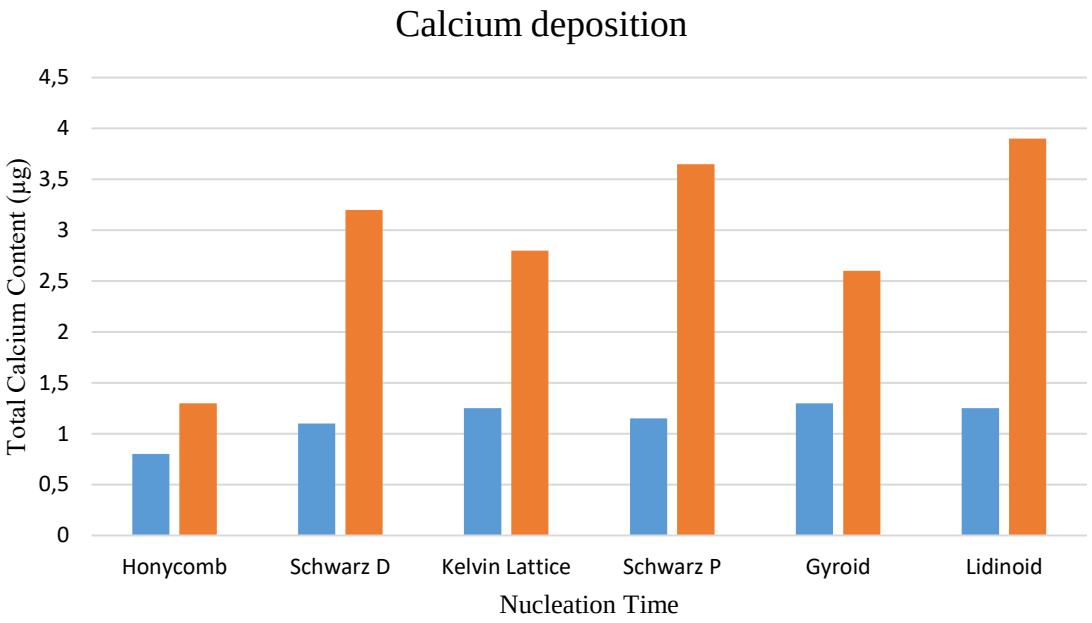

Figure 42 – Total calcium deposition on different scaffolds during various nucleation times.

CONCLUSION

1. It has been found that the crystalline HA and CPP powders obtained by chemical precipitation from an aqueous solution using a biological eggshell waste have a purity of~95%. In this research work, a distinctive feature of the method used for obtaining biological HA is post-thermal processing, which made it possible to obtain HA and CPP particles with an average size of 2-3 μm and improve their crystal structure, and according to EDX analysis, the Ca/P ratio of HA is 1.5, that is suitable for medical uses.

2. The experimental data confirm that obtained polymer-based fibers by electrospinning with the addition of HA particles are potential candidates to use as biological matrixes and drug delivery agents in TE and can reduce the convalescence period. According to the results, Although the particles were obtained with an average size of 1-2 μm due to the synthesis of HA powder, the size of the added HA particles was much smaller after electrospinning (less than 100 nm), which is associated with the behavior of HA particles in high voltage field. It was found that with an increase in the fiber diameter from 100 to 300 nm, the total release of the antibiotic decreased over a 4-week observation period. In contrast, it was shown that the presence of HA in the structure of the films did not affect the release of the antibiotic.

3. Various cell geometries were used to design the TPMS and FGLS structures inspired by natural/mathematical examples, and according to the results, the Gyroid structure is the best in Top-load/Crush test, and the Lidinoid structure is the best in Tensile tests. However, it was found that adding the resin reinforcement precursors to the matrix positively affects the mechanical properties, enhancing osteogenesis and reducing the convalescence period. In addition, a combination of obtained data from mechanical tests with the simulation data was used to develop the structures' parametric design algorithm, which makes the final results more reliable.

4. In order to address biological needs, achieving the required mechanical function and mass transport qualities, the developed parametric design algorithms can generate hierarchical porous structures and create these structures within arbitrary and complicated 3D anatomical geometries that result in porous scaffolds with a controllable shape, pore distribution, size, and interconnectivity. Due to the links that can be established between geometric features made possible by the developed algorithms, the model's shape changes whenever a dimension value changes.

5. Producing resin reinforce precursors by ultrasonic method led to the formation of nanomaterials with suitable size, morphology, and surface properties for medical applications. These nanomaterials are soft magnetic materials, and many investigations show magnetic fields and magnetic nanoparticles' positive effects on osteogenic enhancements. Mechanical properties and in-Vivo behavior of a reinforced scaffold with HA, CPP, and metallic nanoparticles have been evaluated for the first time.

6. In-Vivo results from implanting the scaffolds in dog femur bone and observing the treatment process showed that printed scaffolds coated with HA could decrease the period of convalescence compared to filing the fracture with HA powder. CT scans have confirmed the integration of bone scaffolds with bone tissue over time.

Assessment of the completeness of the solutions to the tasks. The tasks set in the work are completely solved. Scaffolds are printed and coated with SBF and HA and used as support in the dog femur bone. The results are reliable and reasonable since all measurements were carried out on calibrated instruments using standard methods.

Part of the study was performed in the Institute of Nano Science and Nano Technology at the University of Kashan (Kashan, Isfahan province, Iran) inside the group of professor Masoud Salavati Niasari, my foreign scientific supervisor: performing scanning electron microscopy (SEM), elemental analysis, synthesis of magnetic silicates, and analytical techniques such as BET, VSM, and XRD.

Assessment of technical and economic efficiency proposed in the dissertation. The results obtained in the framework of this dissertation can be proposed for producing 3D bone scaffolds based on HA. An advantage of the proposed method for designing and printing scaffolds is that there is no need to remove implanted material after the treatment period, and using the scaffolds as a platform, the cells can immigrate to the specified part of the body and create new tissue.

Assessment of the scientific level of the work performed in comparison with the best achievements in this field. Currently, most medical centers use commercial scaffolds for bone surgery, which are the most expensive items from a commercial point of view, and most of them need to be removed after the treatment period, which requires extra expenses. However, because using biodegradable materials, there is no need to remove 3D printed scaffolds after the treatment period, and they become part of the bone over time.

This work may open up prospects for producing affordable, cheap, and effective scaffolds for bone tissue engineering. The obtained results are of practical interest for obtaining nanomaterials to enhance bone osteogenesis. In addition, the scientific level of the presented dissertation complies with international standards for research conducted in the selected field. It is evidenced by a relatively good level of publications, presentations, and discussions of work results at international symposia and conferences.

REFERENCES

1. Wu A.-M., Bisignano C., James S.L., Abady G.G., Abedi A., Abu-Gharbieh E., Alhassan R.K., Alipour V., Arabloo J., Asaad M., Asmare W.N., Awedew A.F., Banach M., Banerjee S.K., Bijani A., Birhanu T.T.M., Bolla S.R., Cámera L.A., Chang J.-C., Cho D.Y., Chung M.T., Couto R.A.S., Dai X., Dandona L., Dandona R., Farzadfar F., Filip I., Fischer F., Fomenkov A.A., Gill T.K., Gupta B., Haagsma J.A., Haj-Mirzaian A., Hamidi S., Hay S.I., Ilic I.M., Ilic M.D., Ivers R.Q., Jürisson M., Kalhor R., Kanchan T., Kavetskyy T., Khalilov R., Khan E.A., Khan M., Kneib C.J., Krishnamoorthy V., Kumar G.A., Kumar N., Lalloo R., Lasrado S., Lim S.S., Liu Z., Manafi A., Manafi N., Menezes R.G., Meretoja T.J., Miazgowski B., Miller T.R., Mohammad Y., Mohammadian-Hafshejani A., Mokdad A.H., Murray C.J.L., Naderi M., Naimzada M.D., Nayak V.C., Nguyen C.T., Nikbakhsh R., Olagunju A.T., Otstavnov N., Otstavnov S.S., Padubidri J.R., Pereira J., Pham H.Q., Pinheiro M., Polinder S., Pourchamani H., Rabiee N., Radfar A., Rahman M.H.U., Rawaf D.L., Rawaf S., Saeb M.R., Samy A.M., Sanchez Riera L., Schwebel D.C., Shahabi S., Shaikh M.A., Soheili A., Tabarés-Seisdedos R., Tovani-Palone M.R., Tran B.X., Travillian R.S., Valdez P.R., Vasankari T.J., Velazquez D.Z., Venketasubramanian N., Vu G.T., Zhang Z.-J., Vos T. Global, regional, and national burden of bone fractures in 204 countries and territories, 1990–2019: a systematic analysis from the Global Burden of Disease Study 2019. № 9(2)2021.

2. Weiner S., Wagner H.D. The material bone: Structure-mechanical function relations // Annual Review of Materials Science. 1998. № 1(28). P. 271–298. DOI:10.1146/annurev.matsci.28.1.271.

3. Bandyopadhyay-Ghosh S. Bone as a Collagen-hydroxyapatite Composite and its Repair // Trends Biomater. Artif. Organs. 2008. (22). P. 116–124.

4. Knudson D. Fundamentals of Biomechanics. Second Edi Springer, Boston, MA, 2007. 354 P. ISBN:978-0-387-49311-4.

5. Brown J.L., Kumbar S.G., Laurencin C.T. Chapter II.6.7 - Bone Tissue EngineeringAcademic Press, 2013. P. 1194–1214.

6. Abreu E. Peter Ma X, Elisseeff Jennifer, (Editors): Scaffolding in Tissue Engineering // BioMedical Engineering OnLine. 2006. № 1(5). P. 52. DOI:10.1186/1475-925X-5-52.

7. Williams D.F. The Williams Dictionary of BiomaterialsLiverpool University Press, 1999. . ISBN:9780853237341.

8. Armentano I., Dottori M., Fortunati E., Mattioli S., Kenny J.M. Biodegradable polymer matrix nanocomposites for tissue engineering: A review // Polymer Degradation and Stability. 2010. № 11(95). P. 2126–2146. DOI:10.1016/j.polymdegradstab.2010.06.007.

9. Jeong J., Kim J.H., Shim J.H., Hwang N.S., Heo C.Y. Bioactive calcium phosphate materials and applications in bone regeneration // Biomaterials Research. 2019. № 1(23). P. 4. DOI:10.1186/s40824-018-0149-3.

10. Osborn J.F., Newesely H. The material science of calcium phosphate ceramics // Biomaterials. 1980. № 2(1). P. 108–111. DOI:10.1016/0142-

9612(80)90009-5.

11. Vasant S.R., Joshi M.J. A review on calcium pyrophosphate and other related phosphate nano bio-materials and their applications // Reviews on Advanced Materials Science. 2017. № 1(49). P. 44–57.

12. Dubok V.A. Bioceramics - Yesterday, today, tomorrow // Powder Metallurgy and Metal Ceramics. 2000. № 7–8(39). P. 381–394. DOI:10.1023/a:1026617607548.

13. Hench L.L., Thompson I. Twenty-first century challenges for biomaterials // Journal of the Royal Society Interface. 2010. № SUPPL. 4(7). P. S379-91. DOI:10.1098/rsif.2010.0151.focus.

14. Dorozhkin S. V. Calcium orthophosphates in nature, biology and medicine // Materials. 2009. № 2(2). P. 399–498. DOI:10.3390/ma2020399.

15. Byrappa K., Yoshimura M. Handbook of Hydrothermal Technology 2013. . ISBN:9780123750907.

16. Kim J.H., Kim S.H., Kim H.K., Akaike T., Kim S.C. Synthesis and characterization of hydroxyapatite crystals: A review study on the analytical methods // Journal of Biomedical Materials Research. 2002. № 4(62). P. 600–612. DOI:10.1002/jbm.10280.

17. Thanh Hoai T., Kim Nga N. Synthesis and Investigation into Apatite-forming Ability of Hydroxyapatite/Chitosan-based Scaffold // VNU Journal of Science: Natural Sciences and Technology. 2019. № 3(35). DOI:10.25073/2588-1140/vnunst.4896.

18. Mark Weller, Tina Overton, Jonathan Rourke F.A. Inorganic Chemistry. 7th editio Oxford University Press, 2018. . ISBN:978-0-19-252295-5.

19. Dorozhkin S. V. Calcium orthophosphates // Journal of Materials Science. 2007. № 4(42). P. 1061–1095. DOI:10.1007/s10853-006-1467-8.

20. Uskoković V., Desai T.A. In vitro analysis of nanoparticulate hydroxyapatite/chitosan composites as potential drug delivery platforms for the sustained release of antibiotics in the treatment of osteomyelitis // Journal of Pharmaceutical Sciences. 2014. № 2(103). P. 567–579. DOI:10.1002/jps.23824.

21. Yunoki S., Sugiura H., Ikoma T., Kondo E., Yasuda K., Tanaka J. Effects of increased collagen-matrix density on the mechanical properties and in vivo absorbability of hydroxyapatite-collagen composites as artificial bone materials // Biomedical Materials. 2011. № 1(6). P. 15012. DOI:10.1088/1748-6041/6/1/015012.

22. Kalita S.J., Bhardwaj A., Bhatt H.A. Nanocrystalline calcium phosphate ceramics in biomedical engineering // Materials Science and Engineering C. 2007. № 3(27). P. 441–449. DOI:10.1016/j.msec.2006.05.018.

23. Froimson M.I., Garino J., Machenaud A., Vidalain J.P. Minimum 10-year Results of a Tapered, Titanium, Hydroxyapatite-Coated Hip Stem. An Independent Review // Journal of Arthroplasty. 2007. № 1(22). P. 1–7. DOI:10.1016/j.arth.2006.03.003.

24. Tsui Y.C., Doyle C., Clyne T.W. Plasma sprayed hydroxyapatite coatings on titanium substrates. Part 1: Mechanical properties and residual stress levels // Biomaterials. 1998. № 22(19). P. 2015–2029. DOI:10.1016/S0142-9612(98)00103-3.

25. Furlong R.J., Osborn J.F. Fixation of hip prostheses by hydroxyapatite ceramic coatings // Journal of Bone and Joint Surgery - Series B. 1991. № 5(73). P. 741–745. DOI:10.1302/0301-620x.73b5.1654336.

26. Geesink R.G.T. Osteoconductive coatings for total joint arthroplasty // Clinical Orthopaedics and Related Research. 2002. (395). P. 53–65. DOI:10.1097/00003086-200202000-00007.

27. Kang X., Zhang W., Yang C. Mechanical properties study of micro- and nano-hydroxyapatite reinforced ultrahigh molecular weight polyethylene composites // Journal of Applied Polymer Science. 2016. № 3(133). P. n/a-n/a. DOI:10.1002/app.42869.

28. Zhou C., Deng C., Chen X., Zhao X., Chen Y., Fan Y., Zhang X. Mechanical and biological properties of the micro-/nano-grain functionally graded hydroxyapatite bioceramics for bone tissue engineering // Journal of the Mechanical Behavior of Biomedical Materials. 2015. (48). P. 1–11. DOI:10.1016/j.jmbbm.2015.04.002.

29. Sobczyk-Guzenda A., Boniecka P., Laska-Lesniewicz A., Makowka M., Szymanowski H. Micro- and nanoparticulate hydroxyapatite powders as fillers in polyacrylate bone cement-A comparative study // Materials. 2020. № 12(13). P. 1–18. DOI:10.3390/ma13122736.

30. Mohd Pu'ad N.A.S., Abdul Haq R.H., Mohd Noh H., Abdullah H.Z., Idris M.I., Lee T.C. Synthesis method of hydroxyapatite: A review // Materials Today: Proceedings. 2019. (29). P. 233–239. DOI:10.1016/j.matpr.2020.05.536.

31. Sasaki K., Osamu S., Takahashi N. Interface oral health science 2014: Innovative research on biosis-abiosis intelligent interface. 1st ed.Springer Tokyo, 2015. 1–351 P. ISBN:9784431551928.

32. Lu J., Yu H., Chen C. Biological properties of calcium phosphate biomaterials for bone repair: A review // RSC Advances. 2018. № 4(8). P. 2015–2033. DOI:10.1039/c7ra11278e.

33. Ben-Nissan B. Ed. Advances in Calcium Phosphate Biomaterials. 1st ed.Springer, Berlin, Heidelberg, 2014. 547 P. ISBN:978-3-642-53979-4.

34. Pignatello R. Ed. Advances in Biomaterials Science and Biomedical Applications. 1st ed.IntechOpen, 2013. 570 P. ISBN:978-953-51-1051-4.

35. Corrêa T.H.A., Holanda J.N.F. Calcium pyrophosphate powder derived from avian eggshell waste // Ceramica. 2016. № 363(62). P. 278–280. DOI:10.1590/0366-69132016623631986.

36. Bose S., Tarafder S. Calcium phosphate ceramic systems in growth factor and drug delivery for bone tissue engineering: A review // Acta Biomaterialia. 2012. № 4(8). P. 1401–1421. DOI:10.1016/j.actbio.2011.11.017.

37. Karageorgiou V., Kaplan D. Porosity of 3D biomaterial scaffolds and osteogenesis // Biomaterials. 2005. № 27(26). P. 5474–5491. DOI:10.1016/j.biomaterials.2005.02.002.

38. Boden S.D. The abcs of bmps // Orthopaedic Nursing. 2005. № 1(24). P. 49–52. DOI:10.1097/00006416-200501000-00014.

39. Urist M.R., Mikulski A., Lietze A. Solubilized and insolubilized bone

morphogenetic protein // Proceedings of the National Academy of Sciences of the United States of America. 1979. № 4(76). P. 1828–1832. DOI:10.1073/pnas.76.4.1828.

40. Jammalamadaka U., Tappa K. Recent advances in biomaterials for 3D printing and tissue engineering // Journal of Functional Biomaterials. 2018. № 1(9). P. 22. DOI:10.3390/jfb9010022.

41. Michel J.B., Kui Shen Y., Presser Aiden A., Veres A., Gray M.K., Pickett J.P., Hoiberg D., Clancy D., Norvig P., Orwant J., Pinker S., Nowak M.A., Aiden E.L. Quantitative analysis of culture using millions of digitized books // Science. 2011. № 6014(331). P. 176–182. DOI:10.1126/science.1199644.

42. Do A.V., Khorsand B., Geary S.M., Salem A.K. 3D Printing of Scaffolds for Tissue Regeneration Applications // Advanced Healthcare Materials. 2015. № 12(4). P. 1742–1762. DOI:10.1002/adhm.201500168.

43. Aljohani W., Ullah M.W., Zhang X., Yang G. Bioprinting and its applications in tissue engineering and regenerative medicine // International Journal of Biological Macromolecules. 2018. № PartA(107). P. 261–275. DOI:10.1016/j.ijbiomac.2017.08.171.

44. Derakhshanfar S., Mbeleck R., Xu K., Zhang X., Zhong W., Xing M. 3D bioprinting for biomedical devices and tissue engineering: A review of recent trends and advances // Bioactive Materials. 2018. № 2(3). P. 144–156. DOI:10.1016/j.bioactmat.2017.11.008.

45. Shimojo A.A.M., Rodrigues I.C.P., Perez A.G.M., Souto E.M.B., Gabriel L.P., Webster T. Scaffolds for tissue engineering: A state-of- the- art review concerning types, properties, materials, processing, and characterization // Racing for the Surface: Antimicrobial and Interface Tissue Engineering. Cham: Springer International Publishing, 2020. P. 647–676.

46. Chung J.J., Im H., Kim S.H., Park J.W., Jung Y. Toward Biomimetic Scaffolds for Tissue Engineering: 3D Printing Techniques in Regenerative Medicine // Frontiers in Bioengineering and Biotechnology. 2020. (8). P. 1251. DOI:10.3389/fbioe.2020.586406.

47. Bahraminasab M., Edwards K.L. Computational Tailoring of Orthopaedic Biomaterials: Design Principles and Aiding Tools. Singapore: Springer Singapore, 2019. P. 15–31.

48. Salmi M., Tuomi J., Paloheimo K.S., Björkstrand R., Paloheimo M., Salo J., Kontio R., Mesimäki K., Mäkitie A.A. Patient-specific reconstruction with 3D modeling and DMLS additive manufacturing // Rapid Prototyping Journal. 2012. № 3(18). P. 209–214. DOI:10.1108/13552541211218126.

49. Kalender W.A. Computed Tomography: Fundamentals, System Technology, Image Quality, Applications. 3rd ed.Publicis, 2011. 372 P. ISBN:978-3-895-78644-0.

50. Jerban S., Chang E.Y., Du J. Magnetic resonance imaging (MRI) studies of knee joint under mechanical loading: Review // Magnetic Resonance Imaging. 2020. (65). P. 27–36. DOI:10.1016/j.mri.2019.09.007.

51. van Eijnatten M., Koivisto J., Karhu K., Forouzanfar T., Wolff J. The impact of manual threshold selection in medical additive manufacturing // International

Journal of Computer Assisted Radiology and Surgery. 2017. № 4(12). P. 607–615. DOI:10.1007/s11548-016-1490-4.

52. Asghari F., Samiei M., Adibkia K., Akbarzadeh A., Davaran S. Biodegradable and biocompatible polymers for tissue engineering application: a review // Artificial Cells, Nanomedicine and Biotechnology. 2017. № 2(45). P. 185–192. DOI:10.3109/21691401.2016.1146731.

53. Albrektsson T., Johansson C. Osteoinduction, osteoconduction and osseointegration // European Spine Journal. 2001. № Suppl 2(10). P. S96–S101. DOI:10.1007/s005860100282.

54. Senatov F.S., Niaza K. V., Stepashkin A.A., Kaloshkin S.D. Low-cycle fatigue behavior of 3d-printed PLA-based porous scaffolds // Composites Part B: Engineering. 2016. (97). P. 193–200. DOI:10.1016/j.compositesb.2016.04.067.

55. Liu Y., Lim J., Teoh S.H. Review: Development of clinically relevant scaffolds for vascularised bone tissue engineering // Biotechnology Advances. 2013. № 5(31). P. 688–705. DOI:10.1016/j.biotechadv.2012.10.003.

56. Yoo D.J. Porous scaffold design using the distance field and triply periodic minimal surface models // Biomaterials. 2011. № 31(32). P. 7741–7754. DOI:10.1016/j.biomaterials.2011.07.019.

57. Wahid Z., Ariffin M.K.A.M., Baharudin B.T.H.T., Ismail M.I.S., Mustapha F. ABAQUS Simulation of Different Critical Porosities Cubical Scaffold Model // IOP Conference Series: Materials Science and Engineering. 2019. № 1(530). P. 12018. DOI:10.1088/1757-899X/530/1/012018.

58. Leong K.F., Chua C.K., Sudarmadji N., Yeong W.Y. Engineering functionally graded tissue engineering scaffolds. // Journal of the mechanical behavior of biomedical materials. 2008. № 2(1). P. 140–152. DOI:10.1016/j.jmbbm.2007.11.002.

59. Ali D., Sen S. Finite element analysis of mechanical behavior, permeability and fluid induced wall shear stress of high porosity scaffolds with gyroid and lattice-based architectures. // Journal of the mechanical behavior of biomedical materials. 2017. (75). P. 262–270. DOI:10.1016/j.jmbbm.2017.07.035.

60. Singh S., Shukla D.M., Srivastava R. Lattice Modeling and CFD Simulation for Prediction of Permeability in Porous Scaffolds // Materials today: proceedings. 2018. (Volume 5). P. 18879–18886. DOI:10.1016/j.matpr.2018.06.236.

61. Hauptmann N., Lian Q., Ludolph J., Rothe H., Hildebrand G., Liefeith K. Biomimetic Designer Scaffolds Made of D,L-Lactide-ε-Caprolactone Polymers by 2-Photon Polymerization // Tissue Engineering Part B: Reviews. 2019. № 3(25). P. 167–186. DOI:10.1089/ten.teb.2018.0284.

62. Yousefi A.-M., Liu J., Sheppard R., Koo S., Silverstein J., Zhang J., James P.F. I-Optimal Design of Hierarchical 3D Scaffolds Produced by Combining Additive Manufacturing and Thermally Induced Phase Separation // ACS applied bio materials. 2019. № 2(2). P. 685–696. DOI:10.1021/acsabm.8b00534.

63. Kim J.Y., Cho D.-W. The Optimization of Hybrid Scaffold Fabrication Process in Precision Deposition System Using Design of Experiments // Microsyst. Technol. 2009. № 6(15). P. 843–851.

64. Mechano-Biological Optimization of Scaffolds [Электронный ресурс]. URL: https://jwi.charite.de/en/research/research_biomechanics_and_biophysics_of_healing/computational_mechanobiology/mechano_biological_optimization_of_scaffolds/.

65. Petrulyte S., Petrulis D. 1 - Modern textiles and biomaterials for healthcare // Woodhead Publishing Series in TextilesWoodhead Publishing, 2011. P. 1–35.

66. Anil S., Chalisserry E.P., Nam S.Y., Venkatesan J. 24 - Biomaterials for craniofacial tissue engineering and regenerative dentistryWoodhead Publishing, 2019. P. 643–674.

67. Madeira S., Souza J.C.M., Fredel M.C., Henriques B., Silva F.S., Zhang Y. Chapter 9 - Functionally graded nanostructured biomaterials (FGNB) // Advanced NanomaterialsElsevier, 2018. P. 159–180.

68. Jha D.K., Kant T., Singh R.K. A critical review of recent research on functionally graded plates // Composite Structures. 2013. (96). P. 833–849. DOI:https://doi.org/10.1016/j.compstruct.2012.09.001.

69. Raghavendra G.M., Varaprasad K., Jayaramudu T. Chapter 2 - Biomaterials: Design, Development and Biomedical Applications. Oxford: William Andrew Publishing, 2015. P. 21–44.

70. Schwarz H.A. Gesammelte Mathematische Abhandlungen. 1st ed.Springer, Berlin, Heidelberg, 1890. 346 P. ISBN:978-3-642-50356-6.

71. Neovius E.R. Bestimmung zweier speciellen periodischen MinimalflächenHelsingfors : J.C. Frenckell & Sohn, 1883. 117 P.

72. Schoen A.H. Infinite periodic minimal surfaces without self-intersections. (5541)National Aeronautics and Space Administration, 1970. .

73. Alketan O., Abu Al-Rub R. Multifunctional mechanical-metamaterials based on triply periodic minimal surface lattices: A review // Advanced Engineering Materials. 2019. DOI:10.1002/adem.201900524.

74. Han S.C., Choi J.M., Liu G., Kang K. A Microscopic Shell Structure with Schwarz's D-Surface // Scientific Reports. 2017. № 1(7). P. 13405. DOI:10.1038/s41598-017-13618-3.

75. Chen H., Han Q., Wang C., Liu Y., Chen B., Wang J. Porous Scaffold Design for Additive Manufacturing in Orthopedics: A Review // Frontiers in Bioengineering and Biotechnology. 2020. (8). P. 609. DOI:10.3389/fbioe.2020.00609.

76. Fu F. Chapter Six - Design and Analysis of Complex StructuresButterworth-Heinemann, 2018. P. 177–211.

77. Al-Ketan O., Abu Al-Rub R.K. MSLattice: A free software for generating uniform and graded lattices based on triply periodic minimal surfaces // Material Design and Processing Communications. 2021. № 6(3). P. e205. DOI:10.1002/mdp2.205.

78. Kirillova A., Bushev S., Abubakirov A., Sukikh G. Bioethical and legal issues in 3D bioprinting // International Journal of Bioprinting. 2020. № 3(6). P. 1–10. DOI:10.18063/IJB.V6I3.272.

79. Ayusheeva I.Z. Problems of Legal Regulation of Contractual Relations in

the Process of Creating Bio-Print Human Organs // Lex Russica. 2019. (6). P. 92–99.

80. Shuaib M., Haleem A., Kumar S., Javaid M. Impact of 3D Printing on the environment: A literature-based study // Sustainable Operations and Computers. 2021. (2). P. 57–63. DOI:https://doi.org/10.1016/j.susoc.2021.04.001.

81. Daulbaev C.B., Dmitriev T.P., Sultanov F.R., Mansurov Z.A., Aliev E.T. Obtaining Three-Dimensional Nanosize Objects on a “3D Printer + Electrospinning” Machine // Journal of Engineering Physics and Thermophysics. 2017. № 5(90). P. 1115–1118. DOI:10.1007/s10891-017-1665-z.

82. Daulbayev C., Sultanov F., Aldasheva M., Abdybekova A., Bakbolat B., Shams M., Chekiyeva A., Mansurov Z. Nanofibrous biologically soluble scaffolds as an effective drug delivery system // Comptes Rendus Chimie. 2021. № 1(24). P. 1–9. DOI:10.5802/crchim.58.

83. Gomes L., Lello B., de Campos J., Sampaio M. Synthesis and characterization of calcium phosphates produced from chicken eggshell // Cerâmica. 2012. (58). P. 448–452. DOI:10.1590/S0366-69132012000400005.

84. Qi X., Ren Y., Wang X. New advances in the biodegradation of Poly(lactic) acid // International Biodeterioration and Biodegradation. 2017. (117). P. 215–223. DOI:10.1016/j.ibiod.2017.01.010.

85. Howard G.T. Biodegradation of polyurethane: A review // International Biodeterioration and Biodegradation. 2002. № 4(49). P. 245–252. DOI:10.1016/S0964-8305(02)00051-3.

86. Shi J., Zhu L., Li L., Li Z., Yang J., Wang X. A TPMS-based method for modeling porous scaffolds for bionic bone tissue engineering // Scientific reports. 2018. № 1(8). P. 7395. DOI:10.1038/s41598-018-25750-9.

87. Evans F.G., Lebow M. The strength of human compact bone as revealed by engineering technics // The American Journal of Surgery. 1952. № 3(83). P. 326–331. DOI:10.1016/0002-9610(52)90265-1.

88. EVANS F.G., LEBOW M. Regional differences in some of the physical properties of the human femur // Journal of applied physiology. 1951. № 9(3). P. 563–572. DOI:10.1152/jappl.1951.3.9.563.

89. EVANS F.G., PEDERSEN H.E., LISSNER H.R. The role of tensile stress in the mechanism of femoral fractures. // The Journal of bone and joint surgery. American volume. 1951. № 2(33 A). P. 485–501. DOI:10.2106/00004623-195133020-00025.

90. Evans F.G. Stress and Strain in Bones: Their Relation to Fractures and OsteogenesisCharles C. Thomas, 1957. 245 P.

91. Brooks D.B., Burstein A.H., Frankel V.H. The biomechanics of torsional fractures. The stress concentration effect of a drill hole. // The Journal of bone and joint surgery. American volume. 1970. № 3(52). P. 507–514. DOI:10.2106/00004623-197052030-00008.

92. Horst Czichos, Tetsuya Saito L.S. Ed. Springer Handbook of Materials Measurement Methods. 1st ed.Springer Berlin, Heidelberg, 2006. 1208 P.

93. Kokubo T., Takadama H. How useful is SBF in predicting in vivo bone bioactivity? // Biomaterials. 2006. № 15(27). P. 2907–2915.

DOI:10.1016/j.biomaterials.2006.01.017.

94. Castro N.J., Tan W.N., Shen C., Zhang L.G. Simulated Body Fluid Nucleation of Three-Dimensional Printed Elastomeric Scaffolds for Enhanced Osteogenesis // Tissue Engineering - Part A. 2016. № 13–14(22). P. 940–948. DOI:10.1089/ten.tea.2016.0161.

95. Oh D., Han M.-H., Im W.-B., Kim S., Kim K., You C., Ong J. Surface characterization and dissolution study of biodegradable calcium metaphosphate coated by sol–gel method // Journal of Sol-Gel Science and Technology. 2010. (53). P. 627–633. DOI:10.1007/s10971-009-2141-9.

96. Liu H., Yazici H., Ergun C., Webster T.J., Bermek H. An in vitro evaluation of the Ca/P ratio for the cytocompatibility of nano-to-micron particulate calcium phosphates for bone regeneration // Acta Biomaterialia. 2008. № 5(4). P. 1472–1479. DOI:10.1016/j.actbio.2008.02.025.

97. Huang B., Cheng G., Deng C., Zou H. Investigation on some properties of renshapeTM SL7545 type photosensitive resin and its application for stereolithography material // Applied Mechanics and Materials. 2013. (252). P. 220–223. DOI:10.4028/www.scientific.net/AMM.252.220.

98. Shams M., Mansurov Z., Daulbayev C., Bakbolat B. Effect of Lattice Structure and Composite Precursor on Mechanical Properties of 3D-Printed Bone Scaffolds // Eurasian Chemico-Technological Journal. 2021. № 4 SE-Articles(23). DOI:10.18321/ectj1129.

99. Alizadeh S., Fallah N., Nikazar M. An ultrasonic method for the synthesis, control and optimization of CdS/TiO 2 core-shell nanocomposites // RSC Advances. 2019. № 8(9). P. 4314–4324. DOI:10.1039/c8ra10155h.

100. Vaitsis C., Mechili M., Argirusis N., Kanellou E., Pandis P.K., Sourkouni G., Zorpas A., Argirusis C. Ultrasound-Assisted Preparation Methods of Nanoparticles for Energy-Related Applications // Nanotechnology and the Environment. Rijeka: IntechOpen, 2020. P. Ch. 5.

101. Dheyab M.A., Aziz A.A., Jameel M.S. Recent advances in inorganic nanomaterials synthesis using sonochemistry: A comprehensive review on iron oxide, gold and iron oxide coated gold nanoparticles // Molecules. 2021. № 9(26). DOI:10.3390/molecules26092453.

102. Mahdavi K., Salavati-Niasari M., Amiri O., Ghanbari M. Synthesis of La9.33Si6O26 nano-photocatalysts by ultrasonically accelerated method for comparing water treatment efficiency with changing conditions // Arabian Journal of Chemistry. 2022. № 1(15). P. 103481. DOI:https://doi.org/10.1016/j.arabjc.2021.103481.

103. Peng J., Zhao J., Long Y., Xie Y., Nie J., Chen L. Magnetic Materials in Promoting Bone Regeneration // Frontiers in Materials. 2019. (6). DOI:10.3389/fmats.2019.00268.

104. Santoro R.P., Newnham R.E., Nomura S. Magnetic properties of Mn_2SiO_4 and Fe_2SiO_4 // Journal of Physics and Chemistry of Solids. 1966. № 4(27). P. 655–666. DOI:10.1016/0022-3697(66)90216-2.

105. Xia Y., Sun J., Zhao L., Zhang F., Liang X.J., Guo Y., Weir M.D.,

Reynolds M.A., Gu N., Xu H.H.K. Magnetic field and nano-scaffolds with stem cells to enhance bone regeneration // Biomaterials. 2018. (183). P. 151–170. DOI:10.1016/j.biomaterials.2018.08.040.

106. Amiri M., Salavati-Niasari M., Akbari A. Magnetic nanocarriers: Evolution of spinel ferrites for medical applications // Advances in Colloid and Interface Science. 2019. (265). P. 29–44. DOI:10.1016/j.cis.2019.01.003.

107. Florio G. Structural Features of Magnetic Materials // Encyclopedia of Smart Materials. Oxford: Elsevier, 2021. С. 1–9.

108. Fan D., Wang Q., Zhu T., Wang H., Liu B., Wang Y., Liu Z., Liu X., Fan D., Wang X. Recent Advances of Magnetic Nanomaterials in Bone Tissue Repair // Frontiers in Chemistry. 2020. (8). P. 745. DOI:10.3389/fchem.2020.00745.

109. Dasari A., Xue J., Deb S. Magnetic Nanoparticles in Bone Tissue Engineering // Nanomaterials. 2022. № 5(12). P. 757. DOI:10.3390/nano12050757.

110. Li M., Liu J., Cui X., Sun G., Hu J., Xu S., Yang F., Zhang L., Wang X., Tang P. Osteogenesis effects of magnetic nanoparticles modified-porous scaffolds for the reconstruction of bone defect after bone tumor resection // Regenerative Biomaterials. 2019. № 6(6). P. 373–381. DOI:10.1093/rb/rbz019.

111. Kokubo T., Kushitani H., Sakka S., Kitsugi T., Yamamuro T. Solutions able to reproduce in vivo surface-structure changes in bioactive glass-ceramic A-W3 // Journal of Biomedical Materials Research. 1990. № 6(24). P. 721–734. DOI:10.1002/jbm.820240607.

112. Kokubo T. Bioactive glass ceramics: properties and applications // Biomaterials. 1991. № 2(12). P. 155–163. DOI:10.1016/0142-9612(91)90194-F.

113. Mi H.Y., Jing X., Salick M.R., Cordie T.M., Peng X.F., Turng L.S. Morphology, mechanical properties, and mineralization of rigid thermoplastic polyurethane/hydroxyapatite scaffolds for bone tissue applications: Effects of fabrication approaches and hydroxyapatite size // Journal of Materials Science. 2014. № 5(49). P. 2324–2337. DOI:10.1007/s10853-013-7931-3.

114. Boone P.S., Zimmerman M.C., Gutteling E., Lee C.K., Parsons J.R., Langrana N. Bone attachment to hydroxyapatite coated polymers // Journal of Biomedical Materials Research. 1989. № SUPPL. A2(23). P. 183–199.

115. Bergmeister H., Seyidova N., Schreiber C., Strobl M., Grasl C., Walter I., Messner B., Baudis S., Fröhlich S., Marchetti-Deschmann M., Griesser M., Di Franco M., Krssak M., Liska R., Schima H. Biodegradable, thermoplastic polyurethane grafts for small diameter vascular replacements // Acta Biomaterialia. 2015. № 1(11). P. 104–113. DOI:10.1016/j.actbio.2014.09.003.